Computational Studies on the Mechanism of Main-Group Catalysed Reduction Reaction

A Thesis

Submitted for the Degree of

Doctor of Philosophy

by

Pallavi Sarkar

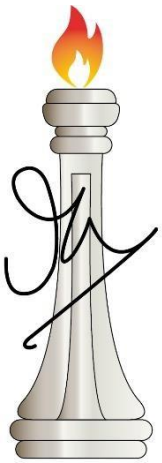

Theoretical Sciences Unit

Jawaharlal Nehru Centre for Advanced Scientific Research

(A Deemed University)

Bengaluru – 560064

July 2022

Dedicated to my Family...

DECLARATION

I hereby DECLARE that the matter embodied in this thesis entitled "**Computational Studies On the Mechanism of Main-Group Catalysed Reduction Reactions**" has been carried out by me at the Theoretical Sciences Unit, Jawaharlal Nehru Centre for Advanced Scientific Research, Bangalore, India under the supervision of Prof. Swapan K Pati and that it has not been submitted elsewhere for the award of any degree or diploma. In Keeping with the general practice in reporting scientific observations, due acknowledgement has been made whether the work described is based on the findings of other investigators. Any omission that might have occured by oversight or error of judegement is regretted.

Pallavi Sarkar

Pallavi Sarkar

CERTIFICATE

I hereby certify that the matter embodied in this thesis entitled "**Computational Studies On the Mechanism of Main-Group Catalysed Reduction Reactions**" has been carried out by Ms. Pallavi Sarkar at the Theoretical Sciences Unit, Jawaharlal Nehru Centre for Advanced Scientific Research, Bangalore, India under my supervision and that it has not been submitted elsewhere for the award of any degree or diploma.

Prof. Swapan K. Pati
(Research Supervisor)

Acknowledgements

First and foremost, I would take this opportunity to acknowledge my research supervisor Prof. Swapan K Pati for his guidance, support, and motivation throughout the journey of my Ph.D. career. I am grateful to him for giving me the opportunity to involve in various collaborative works and the freedom he has given me while working on the projects. Working with him has been a thoroughly enjoyable and learning experience, which has helped me to grow professionally as well as personally.

My heartfelt gratitude to Prof. C. N. R. Rao for his vision about JNC. His presence speeches are truly very inspiring.

I am thankful to all my course instructors in JNCASR, Prof. Waghmare, Prof. Narasimhan, Prof. Balasubramanian, and Prof. Meher K Prakash.

I am very grateful to my collaborators Subir, Arpan, Parul, Sabyasachi, Nilanjana, Prof. Tapas Kumar Maji, Prof. Swadhin Mandal, Prof. S. P. Rath, Dr. Anukul Jana, Prof. Shabana Khan, Prof. Manab Chakraborty for the interesting and fruitful scientific discussions. I would also like to thank all the faculty members of Theoretical Sciences Unit.

I am extremely grateful to my senior Dr. Shubhajit das for all the insightful

discussions which has helped me a lot. He was always a phone call away whenever the going gets tough.

I am thankful to Anusooya ma'am for her love, care and support from the very beginning of my stay in JNCASR. Thanks to Sohan for his warm hospitality during our visits to sir's house.

I would like to thank my seniors Pralokda, Bradraj bhaiya, Asvini and Arkamitadi for their love and support during my first year of Bangalore. My special thanks to my friend Saptarshi for having a listening ear, Himangshu for the fun chats. Thanks to Riaz for always having my back.

I am thankful to my present and past lab mates Swastika, Dibyajyoti, Sukanta, Navamani, Sandhya, Abhiroop, Neha, Madhulika, Supriti, Bidhan, Paramita, Anita, Sayan, Mayank, Sonu, Soumya, Pralhad, Utkarsh for their cooperation.

I thank CSIR for fellowship. Thanks to JNCASR for providing all the facilities, Complab, CCMS colleague Anoop and Suresh, admin, academic office and health centre staffs.

I am grateful to all my teachers from Santiniketan, specially Pranabda, Bidhanda and Shovanda for their mentorship.

Finally I thank my parents and my elder sister for their patience, support and sacrifices without which it would be impossible for me to reach here.

Abbreviations

TM	Transition metal
LA	Lewis acid
LB	Lewis base
THF	Tetreahydrofuran
HOMO	Highest occupied molecular orbital
LUMO	Lowest unoccupied molecular orbital
FMO	Frontier molecular orbital
FLP	Frustrated Lewis pair
EC	Encounter complex
DFT	Density functional theory
Me	Methyl
Et	Ethyl
*n*Pr	n-propyl
*i*Pr	isopropyl
*n*Bu	n-butyl
*t*Bu	tert-butyl
Ph	phenyl
Mes	mesityl
BCF	$B(C_6F_5)_3$
TS	Transition state
PES	Potential energy surface
IRC	Intrinsic reaction coordinate
NPA	Natural population analysis
NBO	Natural bonding analysis
EDA	Energy decomposition analysis
FA	Formic acid
DHR	Dihydrogen release

Synopsis

Reduction reactions constitute an important area in chemistry and among them particularly hydrogenation reactions hold a special interest as catalytic hydrogenation reaction is used for the global production of a myriad of chemical products. Since the initial findings, this area has been largely based on transitional metal mediated reactions. With time, the area of catalysis has also continued to evolve and in the last decade, considerable research effort has been devoted to main-group element chemistry to develop a greener catalytic protocol. Particularly, the emergence of so-called frustrated Lewis pairs (FLPs) draws significant attention. These are combinations of bulky Lewis acids and Lewis bases which are sterically precluded from the formation of a dative bond. The resulting unquenched reactivity of the two sites is utilised for the cooperative activation of a wide range of small molecules. Particularly interesting and relevant to the present thesis is the heterolytic activation of dihydrogen molecule (H_2) by FLP and the subsequent transfer of proton and hydride to an unsaturated substrate of interest. Thus, it develops a transition metal-free catalytic hydrogenation protocol for a wide range of polar and nonpolar organic substrates. While the cooperative interaction of FLPs arises from the acceptor orbital and the donor orbital residing

at two different centres, N-heterocyclic carbenes (NHCs), which is another area of interest of this thesis, are one such example where both the vacant orbital and filled orbital located on the same carbon atom and thus it can mimic the transition metal environment. Additionally, abnormal N-heterocyclic carbenes (aNHC) are also introduced, which can act as an efficient metal-free catalyst for a wide range of chemical transformations. Similar to any area of research, rational design of efficient main-group catalysed reaction protocol relies on the conceptual understanding of the underlying key reaction steps. With this aim in mind, we have been involved in computational studies of a few main-group catalysed reduction reactions. Based on quantum chemical calculations with the aid of density functional theory (DFT), we have been able to investigate the mechanistic cycle and the relevant potential energy surfaces of the intriguing reactions. The thesis is divided into following eight chapters.

Chapter 1 provides an introduction to the field of main-group catalysis with particular attention to FLPs and aNHCs which appear as promising candidates. A brief discussion on the applied computational methodology is also included in this chapter.

In Chapter 2, with the aid of DFT calculations, the mechanism of stepwise hydrogenation of an N-heterocycle quinoline by a benzimidazolylidene stabilised borenium ion has been elucidated. We found that the borenium cation performs the H_2 activation in an FLP like manner with the substrate quinoline acting as a Lewis base. In this context, the inefficiency of aNHC based borenium cations for dihydrogen cleavage and therefore hydrogenation reaction is also rationalized which arises due to the steric crowding around the active site of the catalyst. We have also examined the next hydrogenation steps which are required for the conversion of protonated quinoline to tetrahydro quinoline. Computational results indicate that for the second step of hydrogenation, the 1,4-addition reaction is kinetically favoured over the 1,2-addition pathway. Moreover, it is found that the

zwitterion, obtained from H_2 activation by benzimidazolylidene stabilised borenium ion and quinoline plays a crucial role in this catalytic cycle for the formation of tetrahydroquinoline.

In Chapter 3 we have explored the mechanism of H_2 activation by a recently reported family of geminal FLPs, namely, $(C_2F_5)_3E\text{-}CH_2\text{-}P(tBu)_2$ (E = Si, Ge, Sn), which incorporate a neutral sp^3 tetrel atom as Lewis acid centre. A comprehensive DFT study has been performed to understand how an electronically saturated Lewis acid, which lacks a formally vacant p orbital unlike its cationic congener tetrylium ions or widely used borane, can perform the splitting of the H-H bond. Computational results reveal that in absence of a formal acceptor orbital, the sp^3 Lewis acid centre borrows the required Lewis acidity utilizing the antibonding molecular orbitals of its adjacent groups and the individual contributions vary with the identity of the acceptor and the donor sites. The effect of different substituents, the Lewis acid centre and the Lewis base centre on the energetics of H_2 activation is studied in detail. Our results show the N-containing FLPs $(C_2F_5)_3E\text{-}CH_2\text{-}N(tBu)_2$ (E = Si, Ge, Sn) follow a synchronous mechanism along the reaction pathway, and as a result, have a more favourable H_2 activation profile than those with a phosphorous donor. The present results could provide detail understanding of a general mechanistic framework for dihydrogen cleavage by FLPs with electronically saturated Lewis acids.

In Chapter 4, after the mechanistic understanding obtained from the previous chapter, we explored the ability of these geminal FLPs to act as hydrogenation catalysts using CO_2, carbonyl and imine as substrates. Mechanistic analyses revealed that the transfer of activated hydrogen from FLP to unsaturated bond follows a concerted yet asynchronous pathway. The sequence of proton/hydride transfer is influenced by the donor/acceptor atom as well as the corresponding unsaturated functional group. In the case of the electrophilic substrate, like CO_2 and carbonyl, initially, a hydride transfer takes place followed by a subsequent

proton transfer. For imine hydrogenation, the sequence of this dihydrogen transfer process is controlled by the donor atom of the FLP. For N-containing FLPs, a simultaneous migration of proton and hydride is found, while for FLPs with P atom, the initial release of proton creates a polarization in the C=N bond and thereafter hydride transfer takes place. It is observed that the donor site largely controls the dihydrogen release barrier and in general nitrogen-bearing FLPs have a lower dihydrogen release barrier than those with phosphorus. Additionally, possible decomposition pathways, such as dimerization of the catalysts and reductive elimination reactions are also examined.

In Chapter 5, a comprehensive DFT study has been performed to unravel the mechanism of carbon dioxide hydrogenation reaction by a monomeric copper hydride catalyst working in tandem with a DBU/BCF Lewis pair in a catalytic cycle. Our mechanistic study unveils that the CO_2 activation by the copper-hydride catalyst is kinetically feasible. However, the H_2 activation reaction by the DBU-BCF Lewis pair has a high energetic span and therefore quite difficult to achieve and the results provide a solid support for the experimental observations. Thus, the possible reaction routes for dihydrogen splitting are investigated. The critical role of the solvent, tetrahydrofuran (THF) in this catalytic cycle is elucidated, which actively participates in the H_2 activation by forming a Lewis pair with BCF and acts as a proton shuttle and transfers the proton to the base, DBU. Additionally, the possibility of H_2 activation by an $LCu(DBU)^+$ (L=CAAC) complex is also studied. The resulting ion pair $[DBUH]^+[HBCF]^-$ replace the formate ion from LCuOCOH and forms the LCuHBCF complex. Computational results also show that for resuming the next catalytic cycle, the release of BCF is crucial. In this context, the comparative role of the bases, DBU and PMP are investigated and the inability of PMP/BCF FLP under experimental catalytic condition is rationalized. Insights obtained from this study are critical for the development of transition metal-FLP hybrid catalytic protocol.

Chapter 6 discusses the mechanism of the reductive functionalization reaction of carbon dioxide where the thermally stable and kinetically inert CO_2 molecule has been reduced to its unusual oxidation state C(0) and functionalized with amides by a mesoionic N-heterocyclic imine (mNHI). DFT calculations show that the superior nucleophilicity of this mNHI arises due to its polarized zwitterionic structure. This is further confirmed by comparing its computed proton affinity values with other very similar N-heterocyclic imine complexes. Mechanistic investigations show that due to high nucleophilicity, the catalyst can easily react with CO_2 as well as with $PhSiH_3$ and both the pathways generate silyl formate. It is also observed that the excellent donor ability of this catalyst leads to a significant reduction of the kinetic barrier for the hydride transfer reaction from $PhSiH_3$ to amide in different stages of the reaction.

In Chapter 7 two other classes of reduction reactions, such as hydroboration and cyanosilylation of carbonyl compounds by a new series of p-block Lewis acids, namely stibenium cations have been explored. DFT computation suggests weaker coordination of the counter anions with the cationic core of the catalysts. It also unveils that along with the steric environment at the active site, the coordination strengths of the anions largely influence the Lewis acidity of the active centres as well as the kinetics of the reactions. Additionally, two possible pathways for the hydroboration reaction are explored which confirms that this family of stibenium cations favours a single anchoring pathway over a double-anchoring route. Guided by the mechanistic understanding obtained from this result, these p-block catalysts are further examined for cyanosilylation of aromatic compounds.

Finally, Chapter 8 summarized the main findings emerging from our computational mechanistic models and it also provides future research directions regarding the possible development of the work described in the previous chapters.

List of publications

Publication related to thesis work

1. ”Mechanistic Insights into the Stepwise Hydrogenation of N-heterocycles Using NHC Stabilized Borenium ion ”, Subir Maji, **Pallavi Sarkar**, Arpan Das, Swapan K Pati and Swadhin K Mandal, Inorganic Chemistry (under revision).

2. ”Investigating Tetrel based Neutral Frustrated Lewis Pairs for Hydrogen Activation ”, **Pallavi Sarkar**, Shubhajit Das and Swapan K Pati, Inorganic Chemistry 60(20), 15180-15189 (2021).

3. ”Assessing Tetrel-based Neutral Frustrated Lewis Pairs for Catalytic Hydrogenation”, **Pallavi Sarkar**, Shubhajit Das and Swapan K Pati, J. Phys. Chem. C. 125(41), 22522-22530 (2021).

4. ”On the Mechanism of Copper Hydride-Lewis Pair Cooperative Catalysis for CO_2 Hydrogenation ”, **Pallavi Sarkar**, Shubhajit Das and Swapan K Pati, (manuscript under preparation).

5. ”Reductive Functionalization of CO_2 for Methylation of Amides” Arpan Das, **Pallavi Sarkar**, Subir Maji, Swapan K Pati, Swadhin K Mandal, (Submit-

ted).

6. ”Exploring Dicordinate Stibenium cations as hydroboration and cyanosilylation catalysts” Nilanjana Sen, Prachi Gothe, **Pallavi Sarkar**, Shubhajit Das, Swapan K Pati and Shabana Khan, Chem. Comm. (under revision).

Other publications by the author

7. ”Trisubstituted geminal diazaalkene derived transient 1, 2-carbodications” Debdeep Mandal, Felix Stein, Shubhadeep Chandra, Nicolás I Neuman, **Pallavi Sarkar**, Shubhajit Das, Abhinanda Kundu, Arighna Sarkar, Hemant Rawat, Swapan K Pati, Vadapalli Chandrasekhar, Biprajit Sarkar, Anukul Jana, Chem. Comm. 56,b59, 8233-8236. (2020).

8. ”Facile One-Pot Assembly of Push–Pull Imines by a Selective C–F Substitution Process in Aryl Fluorides” Srinivas Anga, Shubhadeep Chandra, **Pallavi Sarkar**, Shubhajit Das, Debdeep Mandal, Abhinanda Kundu, Hemant Rawat, Carola Schulzke, Biprajit Sarkar, Swapan K Pati, Vadapalli Chandrasekhar, Anukul Jana, Eur. J. Org. Chem. 7445. (2020).

9. ”Bicyclic (alkyl)(amino) carbene stabilized zinc (0) complex with singlet biradicaloid ground state,” NM Rajendran, Nimisha Gautam, **Pallavi Sarkar**, Jasimuddin Ahmed, Arpan Das, Shubhajit Das, Swapan K Pati and Swadhin K Mandal, Chem. Comm. 5(45), 57,43, 5282-5285 (2021).

10. ”Multistimuli and fingertip-triggered luminescence switching: a five-colored ink-free rewritable secured platform with strongest red emission,” Banchhanidhi Prusti, **Pallavi Sarkar**, Swapan K Pati and Manab Chakraborty, J. Mater. Chem. C. 9555, (2021).

11. ”Charge-transfer regulated visible light driven photocatalytic H_2 production and CO_2 reduction in tetrathiafulvalene based coordination polymer

gel," Parul Verma, Ashish Singh, Faruk Ahamed Rahimi, **Pallavi Sarkar**, Sukhendu Nath, Swapan K Pati and Tapas K. Maji, Nat Commun, 12, 7313, (2021).

12. "Activation of O_2 across a C(sp^3)–C(sp^3) bond," Rahul Kumar, Stefan Richter, Suvendu Maity, **Pallavi Sarkar**, Nicolas Chrysochos, Swapan K Pati, Prasanta Ghosh, Carola Schulzke and Anukul Jana, Chem. Comm., 58, 3122, (2021).

13. " Recent Advances in Group 14 and 15 Lewis Acids for Frustrated Lewis Pair Chemistry," Rahul Kumar, **Pallavi Sarkar**, Shubhajit Das and Swapan K Pati, Chemistry An Asian Journal, 12, 202200148, 1-12. (2022).

14. "Bis-N-Heterocyclic Olefin-Derived ,-Diimidazolium-p-quinodimethane: An Air and Moisture Stable Dicationic Thiele Hydrocarbon Analogue," Subhadip Jana, Benedict J. Elvers, **Pallavi Sarkar**, Ivo Krummenacher, Mithilesh Kumar Nayak, Avijit Maiti, Nicolas Chrysochos, Swapan K. Pati, Carola Schulzke, Holger Braunschweig, and Anukul Jana, (submitted).

15. " N,N'-ethylene/propylene/ trans-1,4- cyclohexylene (alkylene)-bridged bis-NHC-CAAC dimers: a new class of redox-active organic molecules," Mithilesh Kumar Nayak, **Pallavi Sarkar**, Benedict J. Elvers, Sakshi Mehta, Fangyuan Zhang, Ivo Krummenacher, Thangavel Vijayakanth, Ramakirushnan Suriya Narayanan, Ramapada Dolai, Biswarup Roy, Vishal Malik, Hemant Rawat, Abhishake Mondal, Prince Ravat, Ramamoorthy Boomishankar, Swapan K. Pati, Carola Schulzke, Holger Braunschweig and Anukul Jana, (submitted).

16. "Cooperativity in Dication Diradical Diiron(III)porphyrin Dimer Catalyzed oxa-Diels-Alder Reactions: Spectroscopic and Mechanistic Insights," Sabyasachi Sarkar, **Pallavi Sarkar**, D. Shamanta, Swapan K Pati, Acs Catalysis, 12, 95899601, (2022).

17. ” Regioselective ring-opening of epoxides towards Markovnikov alcohols: A metal-free catalytic approach using an abnormal N-heterocyclic carbene”, Sreejyothi P., **Pallavi Sarkar**, Supriti Dutta, Arpan Das, Swapan K Pati and Swadhin K Mandal, Chem. Comm. (just accepted).

Contents

Acknowledgements **5**

Synopsis **6**

List of publications **12**

List of Figures **23**

1 Introduction **1**

1.1 Reduction reaction 1

1.2 Introduction to FLP chemistry 5

1.2.1 Historic background 5

1.2.2 Recognising FLP reactivity: activation of H_2 and other small molecules. 6

1.2.3 Mechanism of H_2 cleavage 8

1.2.4 Catalytic hydrogenation 11

1.2.5 Mechanism of Catalytic hydrogenation 11

1.2.6 Factors controlling FLP hydrogenation 13

1.3 N-Heterocyclic Carbenes (NHC) 17

1.3.1 Activation of small molecules 18
1.3.2 Stabilization of reactive main group species 20
1.4 Computational methodology 21
1.4.1 General aspects 21
1.4.2 Electronic structure calculations 22
1.4.3 Born-Oppenheimer Approximation 23
1.4.4 Density Functional Theory 24
1.5 Softwares used: 28
1.6 Scope of the thesis 29
1.7 References 30

2 Mechanistic Insight into the Stepwise Hydrogenation of N-heterocycles Catalysed by NHC Stabilized Borenium ion 37
2.1 Introduction 38
2.2 Computational details 40
2.3 Results and discussions 41
2.3.1 Hydrogen activation by borenium ions 42
2.3.2 The second hydrogenation step: 1,4 addition 44
2.3.3 The third hydrogenation step: C2=C3 hydrogenation 45
2.4 Conclusion 49
2.5 References 49

3 Investigating Tetrel based Neutral Frustrated Lewis Pairs for Hydrogen Activation 53
3.1 Introduction 54
3.2 Computational details 55
3.2.1 Activation strain analysis 56
3.2.2 Energy decomposition analysis 56

3.3 Results and discussions 57
3.3.1 Structural features 58
3.3.2 H_2 activation 59
3.3.3 Mechanism of H_2 activation 60
3.3.4 Energetics of H_2 activation 65
3.4 Conclusion 75
3.5 References 76

4 Assessing Tetrel-based Neutral Frustrated Lewis Pairs for Catalytic Hydrogenation 81
4.1 Introduction 82
4.2 Computational details 83
4.2.1 Activation-strain analysis 84
4.3 Results and discussions 85
4.3.1 Catalytic hydrogenation of Carbon-dioxide 85
4.3.2 Catalytic hydrogenation of carbonyls and imines 92
4.3.3 Side reactions 100
4.3.4 Propensity of dimer formation 100
4.3.5 Reductive elimination decomposition pathway 101
4.4 Conclusions 104
4.5 References 105

5 On the Mechanism of Copper hydride-Lewis Pair Cooperative Catalysis for CO_2 Hydrogenation 107
5.1 Introduction 108
5.2 Computational details 111
5.3 Results and discussion 111
5.3.1 Activation of CO_2 by Copper hydride 112

5.3.2 Activation of H_2 by FLP 112
5.3.3 Regeneration of Cu-H using H-BCF 113
5.3.4 Activation of H_2 by DBU/BCF 113
5.3.5 Alternative Lewis pair in the system: H_2 activation by THF/BCF Lewis pair 115
5.3.6 Activation of H_2 by L-Cu-$(DBU)^+$ 116
5.3.7 Regeneration of Cooper hydride 117
5.3.8 Next catalytic cycle 119
5.4 Conclusions 123
5.5 References 123

6 Reductive Functionalization of CO_2 for Methylation of Amide 125
6.1 Introduction 126
6.2 Computational details 128
6.3 Results and Discussion 129
6.4 Conclusions 138
6.5 References 138

7 Exploring Dicordinate Stibenium Cations as Efficient Hydroboration and Cyanosilylation Catalysts 141
7.1 Introduction 142
7.2 Computational details 143
7.3 Results and Discussion 144
7.3.1 Structural features 144
7.3.2 Catalytic hydroboration reaction 146
7.3.3 Catalytic cyanosilylation reaction 151
7.4 Conclusions 154
7.5 References 155

8 Summary & Outlook **159**

List of Figures

1.1 Examples of some transition metal catalysed reduction reactions. . . 2

1.2 Frontier orbital model for different modes of H_2 activation by TMs (a) Homolytic H_2 activation (b) Heterolytic H_2 activation..... 3

1.3 Frontier orbital interaction of dihydrogen with (a) main group multiple bonds (b) singlet main group species eg. carbenes, tetrylenes..... 4

1.4 A few examples of non-classical behaviour by some sterically crowded Lewis acids and Lewis bases..... 5

1.5 The initial examples of H_2 activation by a few intramolecular and intermolecular FLPs..... 7

1.6 Some examples of Lewis acid (top) and Lewis bases (bottom) utilized in FLP chemistry 8

1.7 Selective examples of reaction of FLP with various small molecules. 9

1.8 Mechanism of H_2 activation by (a) intermolecular (b) intramolecular FLPs. (c) The proposed reactivity models for heterolytic splitting of H_2 10

1.9 A schematic representation of FLP catalysed hydrogenation cycle..... 11

1.10 Selective examples of FLP-catalysed hydrogenation reaction. 12

1.11 Different mechanistic pathways possible for FLP-mediated catalytic hydrogenation of an unsaturated substrate X=Y, where Y is basic site. 13

1.12 Influence of LA/LB strength on the thermodynamics of H_2 activation. 14

1.13 Effect of steric bulk on the LA/LB interaction. 15

1.14 Reactivity of two intramolecular phosphine/borane FLPs with slightly different linkers. 16

1.15 The electronic effects involved in NHC and CAAC....18

1.16 (a)Reaction of NHCs with various small molecules (b) NHC as Lewis base in FLP mediated H_2 activation. 19

2.1 Benzimidazolylidene stabilized borenium ion catalysed hydrogenation of N-heterocycles under ambient conditions. 39

2.2 Geometry optimized structures of Benzimidazolylidene stabilized borenium ion (**Catalysts A**) and aNHC stabilized borenium ion (**Catalyst B**) 41

2.3 The solvent corrected Gibbs free energy profile for the hydrogen activation by the FLP formed by **1** and **A**. All energies are reported in kcal/mol. All distances are shown in Å. 43

2.4 The solvent corrected Gibbs free energy profile for the hydrogen activation by the FLP formed by **1** and **B**. All energies are reported in kcal/mol. All distances are shown in Å. 44

2.5 Possible reaction routes for the second hydrogenation step of quinoline. 45

2.6 The solvent corrected Gibbs free energy profile for the second hydrogenation step of quinoline. 46

2.7 Geometry optimized structures of the intermediates/transition states involved in the second hydrogenation step (up, 1,4 addition) and (down 1,2 addition) of the catalytic cycle. 46

2.8 Possible reaction routes for the third hydrogenation step of quinoline. 47

2.9 The solvent corrected Gibbs free energy profile for the second hydrogenation step of quinoline. 48

2.10 Geometry optimized structures of the intermediates/transition states involved in the third hydrogenation step. 48

3.1 Group 13 and 14 LAs used in FLP chemistry (left), Intramolecular FLPs featuring neutral tetrel atom 55

3.2 General structural framework and the series of the geminal FLP systems considered in this study for H_2 activation. Here E=Tetrel atom and D=Donor atom. 58

3.3 Optimized geometries of (a) $(C_2F_5)_3Si\text{-}CH_2\text{-}P(tBu)_2$ (b) $(C_2F_5)_3Ge\text{-}CH_2\text{-}P(tBu)_2$ and (c) $(C_2F_5)_3Sn\text{-}CH_2\text{-}P(tBu)_2$. Colour code C (grey), H(white), P (yellow), F (light green), Si (magenta), Ge (pale blue), Sn (green). 59

3.4 Schematic representation of H_2 activation reaction by **1** 59

3.5 Geometry optimized structures of the intermediates/TSs involved in H_2 activation process by **1-Sn-N**. All distances are shown in Å. The hydrogen atoms are omitted for clarity 60

3.6 Frontier molecular orbitals of **1**s. 61

3.7 NBOs for **TS1** of **1-Sn-N** highlighting the major interactions 63

3.8 Schematic representation of the mechanism of H_2 activation by **1** 63

3.9 Donor-acceptor interaction energies estimated at the second-order perturbation theory level associated with interaction $\sigma H_2 \rightarrow \sigma^*(E\text{-}CH_2)/\sigma^*(E\text{-}R)$ along the minimum energy path for (a) **1-Si-P** (b) **1-Ge-P** and (c) **1-Sn-P**. The dotted lines denote the respective TSs. 64

3.10 Donor-acceptor interaction energies estimated at the second-order perturbation theory level associated with interaction $\sigma H_2 \rightarrow \sigma^*(E\text{-}CH_2)/\sigma^*(E\text{-}R)$ along the minimum energy path for (a) **1-Si-P** (b) **1-Si-N**, (c) **1-Ge-P** (d) **1-Ge-N** (e) **1-Sn-P** and (f) **1-Sn-N**. The dotted lines denote the respective TS. 65

3.11 Donor-acceptor interaction energies estimated at the second-order peturbation level associated with interaction $\sigma H_2 \rightarrow \sigma^*(E\text{-}CH_2)/\sigma^*(E\text{-}R)$ along the minimum energy path for (a) $\mathbf{(C_2F_5)_3SiCH_2P(tBu)_2}$ (b) $\mathbf{(C_2F_5)_3SiOP(tBu)_2}$.....66

3.12 The computed values of H_2 activation barrier (ΔG_a) and Gibbs free energy of H_2 activation (ΔG_r) for all FLPs. All energies are given in kcal/mol. 67

3.13 Activation-strain profiles for H_2 activation reaction by **1-Si-P** (green), **1-Ge-P** (red) and **1-Sn-P** (violet) along the reaction coordinate projected onto the H-H bond length. The black dots represent the respective TSs. 68

3.14 Evolution of the Wiberg bond index values for the H-H, E-H and D-H bonds for (a) **1-Sn-N** and (b) **1-Sn-P** along the pseudo-IRC path, depicted as a function of the H-H bond length. The dotted lines indicate the respective TSs.....70

3.15 Plot of the computed activation barriers (ΔG_a) vs the H..H distance in the corresponding transition states for (a) all FLP systems with Sn Lewis acid (b) all FLP systems with Si Lewis acid.....72

3.16 Activation-strain profiles for H_2 activation reaction by **1-Sn-P** (blue) and **1-Sn-N** (red) along the reaction coordinate depicted as a function of the H-H distance. The black dots represent the respective TSs. 73

3.17 Division of strain term ΔE_{strain} into $\Delta E_{strain}(1)$ and $\Delta E_{strain}(H_2)$. 73

3.18 Energy-decomposition analysis for the H_2 activation reaction by **1-Sn-P** (square) and **1-Sn-N** (triangle) along the reaction coordinate depicted as a function of the H-H distance. 74

4.1 The proposed scheme for catalytic hydrogenation of an unsaturated substrate X=Y. 83

4.2 Relative Gibbs free energy profiles for catalytic hydrogenation of CO_2 by **1-Si-N**. Solvent-corrected Gibbs free energy (kcal/mol) values are given in parenthesis. 85

4.3 Geometry optimized structures of the intermediate(s)/TS involved in the DHR of **2-Si-N** to CO_2. All distances are given in Å. 86

4.4 Natural Bond Orbitals (NBOs) for the reaction between **2-Si-N** and CO_2 highlighting the major interactions at three key points (reactant complex, midpoint amd TS) along the reaction coordinate. 87

4.5 Evolution of Wiberg bond index values for the Si-H, D-H, C-H and O-H bonds for (a) **1-Si-N** and (b) **1-Si-P** along the pseudo-IRC path depicted as a function of the SiH...C distance for CO_2 hydrogenation. 88

4.6 The computed values of CO_2 hydrogenation barrier, Free energies of CO_2 hydrogenation and the energy spans for all FLPs. All energies are given in kcal/mol. 89

4.7 Activation-strain profiles for CO_2 activation reaction by **3-Si-P** (blue) and **3-Si-N** (red) along the reaction coordinate depicted as a function of the SiH…C distance. 90

4.8 Division of strain term ΔE_{strain} into ΔE_{strain}(2-FLP) and $\Delta E_{strain}(CO_2)$. 91

4.9 Geometry optimized structures of the intermediate(s)/TS involved in the DHR of **2-Si-N** to Me_2CO. All distances are given in Å. The hydrogen atoms attached to the carbon atoms of FLP are omitted for clarity 93

4.10 Evolution of Wiberg bond index values for the Si-H, D-H, C-H and O-H bonds for (a) **1-Si-N** and (b) **1-Si-P** along the pseudo-IRC path depicted as a function of the SiH…C distance for Me_2CO hydrogenation. 94

4.11 Relative Gibbs free energy profiles for catalytic hydrogenation of Me_2CO (violet line) and H_2CNH (green line) by **1-Si-N**. Solvent-corrected Gibbs free energy (kcal/mol) values are given in parenthesis. 94

4.12 The computed values of Me_2CO hydrogenation barrier, Free energies of Me_2CO hydrogenation and the energy spans for all FLPs. All energies are given in kcal/mol. 95

4.13 Geometry optimized structures of (a) **4^{CO}-Sn-N** (b) **4^{CO}-Si-N** 96

4.14 Geometry optimized structures of the intermediate(s)/TS involved in the DHR of **2-Si-N** to H_2CNH. All distances are given in Å. The hydrogen atoms attached to the carbon atoms of FLP are omitted for clarity 97

4.15 The computed values of H_2CNH hydrogenation barrier, Free energies of H_2CNH hydrogenation and the energy spans for all FLPs. All energies are given in kcal/mol. 98

4.16 Activation-strain profiles for H_2CNH activation reaction by **3-Si-P** (blue) and **3-Si-N** (red) along the reaction coordinate depicted as a function of the DH...N distance 99

4.17 Schematic representation of dimer formation by **1**..... 100

4.18 Computed values of (ΔG_{dimer}) by **1** 101

4.19 Schematic representation of reductive elimination reaction by **2** (top). Geometry optimized structures of the stationary points involved in the reaction by **1-Sn-P** (bottom). All distances are given in Å. 102

4.20 A comparison of the TS1 and ($TS3^{XY}$) values with the activation barrier ($TS3^{elm}$) and reaction gibbs free energy of reductive elimination for all FLPs. All energies are given in kcal/mol. 103

5.1 Limitation of a typical FLP catalysed CO_2 hydrogenation and a Copper catalysed CO_2 hydrogenation catalytic cycle..... 108

5.2 Possible reaction route for the copper-hydride/Lewis pair catalysed hydrogenation ofcarbon dioxide. 109

5.3 CO_2 activation byCopper-hydride complex..... 112

5.4 H_2 activation by PMP/BCF FLP..... 112

5.5 Reaction of **1** with **B1** resulting in the formation of **C1**..... 113

5.6 The relative gibbs free energy profile for the H_2 activation by DBU/BCF pair.The upper panel shows the geometry optimized structures of the intermediate(s)/TS involved in this process. 114

5.7 The relative gibbs free energy profile for the H_2 activation by THF/BCF pair.The upper panel shows the geometry optimized structures of the intermediate(s)/TS involved in this process. 115

5.8 The relative gibbs free energy profile for the H_2 activation by **LCu(DBU)**$^+$ .The upper panel shows the geometry optimized structures of the intermediate(s)/TS involved in this process.....117

5.9 Proposed catalytic cycle for the regeneration of Copper-hydride.....118

5.10 The plausible reaction pathways for the conversion of **C1** to **B1** 120

5.11 The gibbs free energy profile for the conversion of **C1** to **B1** according to pathway-3. 121

5.12 The gibbs free energy profile for the conversion of **C1** to **B1** according to pathway-4. 122

6.1 Comparison among NHIs, MIIs, and mNHIs.....127

6.2 Reductive functionalization of amide in presence of CO_2 catalysed by mNHI. 128

6.3 Comparison of proton affinity values among various NHIs, MIIs, and mNHIs. All values are reported in kcal/mol. 129

6.4 Natural transition orbitals (NTOs) for the major absorptions of **2a**, **2b** and **2c** obtained from TDDFT calculations. 130

6.5 Proposed reaction mechanism for the reductive functionalization of CO_2 131

6.6 The solvent corrected Gibbs free energy profile for the conversion of CO_2 to silyl formate.....132

6.7 Geometry-optimized structures of the intermediate(s)/TS involved in the conversion of CO_2 to silylformate.....133

6.8 The solvent corrected Gibbs free energy profile for the conversion of amide to N-formyl amide. 134

6.9 Geometry-optimized structures of the intermediate(s)/TS involved in the conversion of amide to N-formyl amide. 135

6.10 The solvent corrected Gibbs free energy profile for the conversion of N-formyl amide to final product. 136

6.11 Geometry-optimized structures of the intermediate(s)/TS involved in the conversion of N-formyl amide to final product. 137

7.1 Different stibenium cations studied in this work. 143

7.2 Geometry optimized structures of Catalyst **A**, **B** and **C**. Atom colour code: C (grey), N (blue), O (oxygen), F (green), S (yellow), Sb (purple). Hydrogen atoms are omitted for clarity. 144

7.3 Computed free energies of anion dissociation values for Catalyst **A**, **B** and **C** 145

7.4 Presence of electron-donating interaction for Catalyst **B** and **C**. Atom colour code: C (grey), N (blue), O (oxygen), F (green), S (yellow), Sb (purple). 145

7.5 The model catalysts used for the initial investigation of reaction mechanism. 146

7.6 Catalytic cycle for hydroboration of benzaldehyde using the model catalyst **Y** (a) single-anchoring pathway (b) double-anchoring pathway 147

7.7 The solvent corrected Gibbs free energy profiles for the hydroboration of PhCHO catalysed by (a) **Y** and (b) **Z**. The green profile corresponds to the single-anchoring mechanism whereas the blue profile corresponds to the double-anchoring mechanism. 147

7.8 The solvent corrected Gibbs free energy profiles for the hydroboration of $PhCOCH_3$ catalysed by (a) **Y** and (b) **Z**. The green profile corresponds to the single-anchoring mechanism whereas the blue profile corresponds to the double-anchoring mechanism. 148

7.9 Proposed catalytic cycle for hydroboration of benzaldehyde using the catalysts **A**, **B** and **C** 149
7.10 The solvent corrected Gibbs free energy profiles for the hydroboration of PhCHO catalysed by **A**, **B** and **C** 150
7.11 The geometry optimized structures of the intermediates/TSs involved in the hydroboration of PhCHO. Atom colour code: C (grey), N (blue), O (oxygen), F (green), S (yellow), Sb (purple). 151
7.12 The solvent corrected Gibbs free energy profiles for the hydroboration of PhCOMe catalysed by **A**, **B** and **C** 152
7.13 The geometry optimized structures of the TSs involved in the hydroboration of PhCOMe by catalysts **A**, **B** and **C** respectively. Atom colour code: C (grey), N (blue), O (oxygen), F (green), S (yellow), Sb (purple), B (pink). 152
7.14 Proposed catalytic cycle for cyanosilylation of benzaldehyde using the catalysts **A** and **B** 153
7.15 The geometry optimized structures of the intermediates/TSs involved in the cyanosilylation of PhCHO, by catalyst **A** (up) and **B** (down).Atom colour code: C (grey), N (blue), O (oxygen), F (green), S (yellow), Sb (purple), Si (golden yellow). 154

1 Introduction

1.1 Reduction reaction

Reduction of organic substrates into value-added products is one of the most important reactions in chemistry. Among the wide range of reduction reactions, hydrogenation reaction, which is associated with the addition of hydrogen across the unsaturated chemical bond, in presence of a catalyst, has found extensive applications both in academia and in industrial sectors [1]. The genesis of hydrogenation reaction is almost a century old and dates back to the seminal work of Paul Sabatier, where this transformation was achieved using H_2 pressure over finely divided metals.[2] These catalysts are originally heterogeneous in nature. Later in 1960, homogeneous catalysts based on precious metals, Ir, Rh, and Ru are also developed enabling catalysis in solution. Both of these catalytic processes have certain advantages and drawbacks. However, homogeneous catalysis comes with some attractive opportunities (i) it has a well defined molecular complex as catalyst, which can be monitored easily in solution via suitable spectroscopic, microscopic and computational tools (ii) the active sites are quite precise and can readily be optimized to attain the required activity (iii) generally associated with high selectivity thus can afford excellent chemo, regio and stereoselectivity (iv)

the reaction conditions are often mild. Nonetheless, there is a con side also to this reaction, i.e., being in the same phase, it is quite difficult to extract out the products.

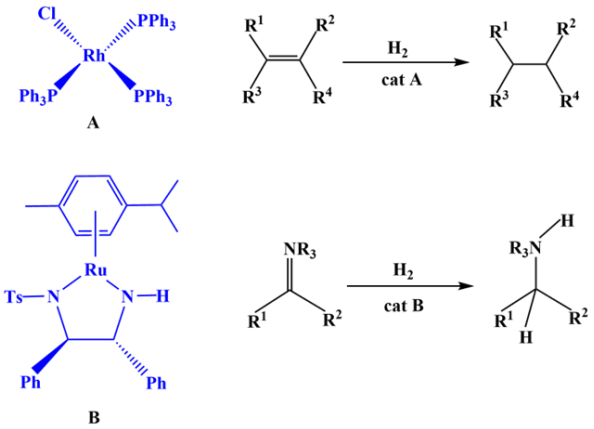

Figure 1.1: Examples of some transition metal catalysed reduction reactions.

Keeping all this in mind, a plethora of both homogeneous and heterogeneous hydrogenation catalysts have been developed across the last century. An important examples is the Wilkinson's catalyst, which plays a significant role in the progress of organometallic chemistry. Here a Rhodium catalyst is employed for olefin hydrogenation with molecular hydrogen [3]. Another example is Noyori's Ruthenium catalyst, which can perform stereo-selective reduction of unsaturated carbonyl and imine substrates [4]. In majority of the cases, the hydrogenation catalysts, irrespective of their nature, are based on d-block transition metals (TMs). This ubiquity of TMs can be attributed to the presence of both occupied and empty d-shell orbitals at the same site, which generally lies in close energy window. By virtue of these partially filled frontier orbitals, the TMs can successfully activate dihydrogen molecule (H_2). Needless to say that the activation of inert H_2 molecule is the critical step of any hydrogenation reaction. In this regard, depending on the metal-ligand framework, various modes of H_2 activation by TMs are reported in the literature which are shown in Figure 1.2. Generally, homolytic

H_2 activation involves two cooperative electron transfer (ET) processes, such as electron donation from σ bonding molecular orbital of H_2 into an vacant d-orbital of TM and a back donation from a d-orbital to empty σ^* antibonding molecular orbital of H_2. Heterolytic cleavage of the H-H bond is also possible if instead of a backdonation from the metal centre, σ^* of H_2 accepts electrons density from a filled ligand orbital.

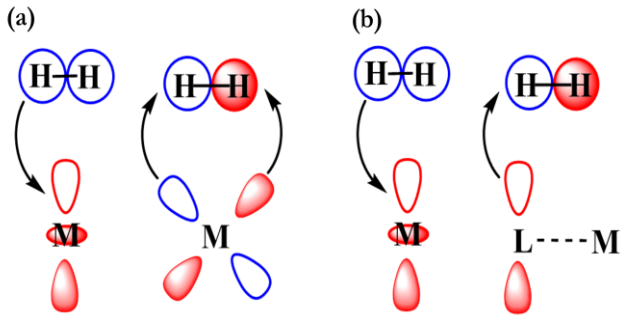

Figure 1.2: Frontier orbital model for different modes of H_2 activation by TMs (a) Homolytic H_2 activation (b) Heterolytic H_2 activation

The field of catalysis has continued to evolve over the years and has broadened to large extent. On one side when the application of TMs is prevailing in synthetic organic chemistry laboratories, on the other side chemists continue to replace the use of toxic precious metals in many important catalytic transformations with environmentally benign and cheap main group elements. Such ideas offered an approach to "greener catalysts", via conceptually distinct protocols. Although the prospect of metal-free catalysis is already generated quite a long ago, it is initially thought that heavier main group elements show more resemblance with TMs, compared to their lighter congeners [5]. However, some interesting developments in the latter quarter of the 20th century, like the synthesis of stannylene [6], disilene [7] and isolation of P=P [8] and Si=C [9] containing compounds have changed the concept drastically. The notion of main group chemistry drew more attention when main group elements are found to react with small molecules and perform cleavage of strong σ bonds under ambient conditions [10,11] The first such examples are

ArGeGeAr′ [12] and ArSnSnAr′ [13] which are found to engage in dihydrogen activation. Such reactivity can be explained by the cooperative interactions among the donor-acceptor orbitals of main group species with the molecular orbitals of H_2. Figure 1.3 depicts the mode of H_2 activation by these lighter main group elements, which possess a different set of frontier orbitals like a lone pair of electrons and a vacant p orbital, in comparison to the TMs.

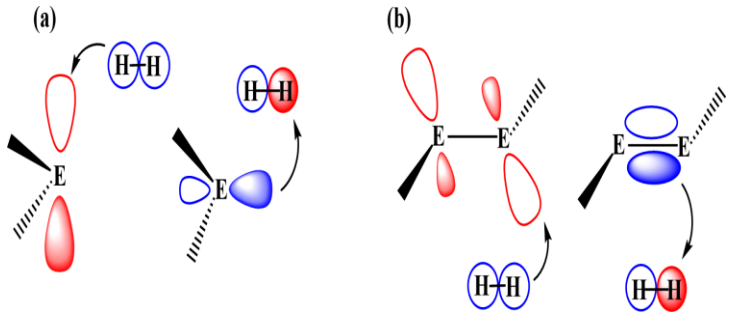

Figure 1.3: Frontier orbital interaction of dihydrogen with (a) main group multiple bonds (b) singlet main group species eg. carbenes, tetrylenes.

This area of main group catalysis experienced a paradigm shift with the advent of so-called frustrated Lewis pairs (FLPs). Seminal works by Stephan *rt al.* in 2007 showed that the synergistic action between sterically precluded Lewis acid-base pairs leads to the heterolytic splitting of H_2 molecule. This remarkable chemistry has played a pivotal role in the advancement of metal-free routes to catalytic hydrogenations which was mostly considered as purview of transition metals. Along with hydrogenation, the reactivity of FLP with H_2 gained popularity in inorganic and materials chemistry. This rapid developments and applications of the simple concept of FLP has even made transition metal chemists take note of it. Since a significant portion of this thesis are associated with chemistry exhibited by FLPs, in the next section a discussion on the background on the key concepts of FLP chemistry is presented. It is important to clarify that the another aspect of reduction reaction is the addition of electrons. However, in this thesis reduction reactions generally means addition of hydrogen across an unsaturated chemical bond.

1.2 Introduction to FLP chemistry

1.2.1 Historic background

It is the pioneering and seminal work of Gilbert Lewis in 1920 that drew the analogy of the chemistry of main group elements to that of Bronsted acids and bases, referring electron acceptors as Lewis acids (LAs) and electron donors as Lewis bases (LBs) [14]. A combination of LA and LB usually neutralizes each other by forming a classical Lewis acid-base adduct. This reactivity arises due to the interaction of the low-lying lowest molecular orbital (LUMO) of LA with the lone pair of electrons residing in the high-lying highest occupied molecular orbital (HOMO) of LB. In fact, most of the reactivity of the main group/TM-chemistry can be described by this in terms of LA/LB interactions.

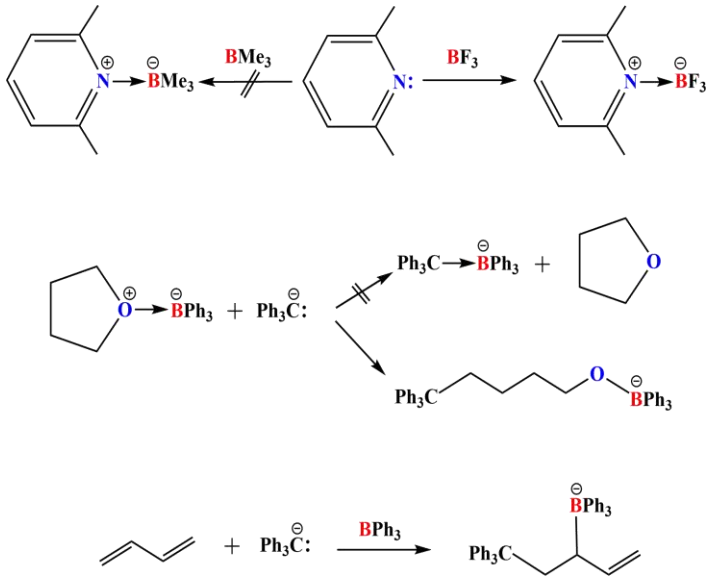

Figure 1.4: A few examples of non-classical behaviour by some sterically crowded Lewis acids and Lewis bases.

Along with that, there are also reports in the literature that contravene Lewis' rules. For example in 1942 Brown and coworkers found that while the combination of lutidine and BF_3 form a dative adduct, the combination of lutidine and BMe_3

did not react (Figure 1.4) [15, 16]. Another example was reported by Wittig and coworkers in 1950, where they found that the reaction between $Na[CPh_3]$ and $(THF)BPh_3$ does not lead to the displacement of weaker base, THF. Rather a ring opening reaction takes place at a sterically more available carbon instead of the Lewis acidic boron centre [17]. Another example is reported by Wittig and Tochtermann, where the polymerisation reaction of butadiene in the presence of $Na[CPh_3]$ and BPh_3 give rise to a trapping product via the 1,2-addition to butadiene [18]. However, no Lewis acid-base adduct between BPh_3 and Ph_3C was observed (Figure 1.4). The above examples illustrate that reactions involving sterically demanding Lewis acid and bases are of special nature and often find alternative routes than the traditional classical adduct formation.

1.2.2 Recognising FLP reactivity: activation of H_2 and other small molecules.

In 2006, Douglas W. Stephan and coworkers isolated a rare zwitterionic phosphonium hydridoborate, $[Mes_2PHC_6F_4BH(C_6F_5)_2]$ that contains both protic and hydridic fragments in the same molecule [19]. When heated to 150^0C, it was found to liberate H_2 affording $[Mes_2PC_6F_4B(C_6F_5)_2]$. Most surprisingly, the resulting phosphinoborane rapidly regenerates the original phosphonium hydridoborate when reacts with 1 atm H_2 at 25^0C (Figure 1.5). This serves as the first known metal-free system that reversibly uptakes and releases dihydrogen molecule.

Eventually, this chemistry was extended to simpler Lewis acids and bases when in 2007 Stephan and Welch reported heterolytic activation of H_2 by a combination of tBu_3P and $B(C_6F_5)_3$. This intermolecular Lewis pair shows no spectroscopic evidence of dative adduct and can perform H_2 activation [20]. This finding demonstrates that the presence of both the active LA and LB sites in the same molecule is not a prerequisite. At the same time, the Erker group provided another exam-

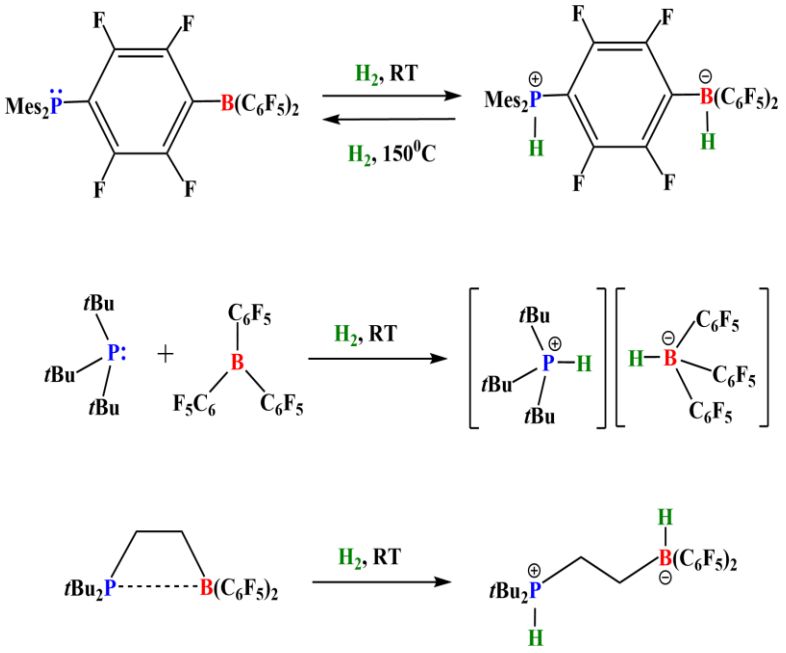

Figure 1.5: The initial examples of H_2 activation by a few intramolecular and intermolecular FLPs.

ple of facile H_2 activation by an ethylene-bridged phosphine borane intramolecular Lewis pair [21] (Figure 1.5). The unique reactivity was attributed to the inability of this main group Lewis pairs to neutralize each other as a result of the steric bulk associated with them. Hence the unquenched reactivity of these active centres can be exploited for the TM-like activation of the relatively inert, apolar H—H bond. Stephan *et al.* coined the term "Frustrated Lewis Pairs" to classify such combinations of bulky LAs and bulky LBs [22].

With the gradual development in this field, FLP chemistry witnessed a broad range of new LAs and LBs across the periodic table [23]. Moving from the ubiquity of borane, the list of LAs has been extented to cationic borenium, silylium, carbocations, stannylium, phosphoniums, nitrenium, zirconocenes *etc* [24,25]. Similarly family of LBs included amines, ethers, thioethers, carbenes, carbodiphosphorans to phosphazenes *etc* [26-31]. These new Lewis components hold great importance to achieve essential criteria, such as functional group tolerance, 'open-bench' sta-

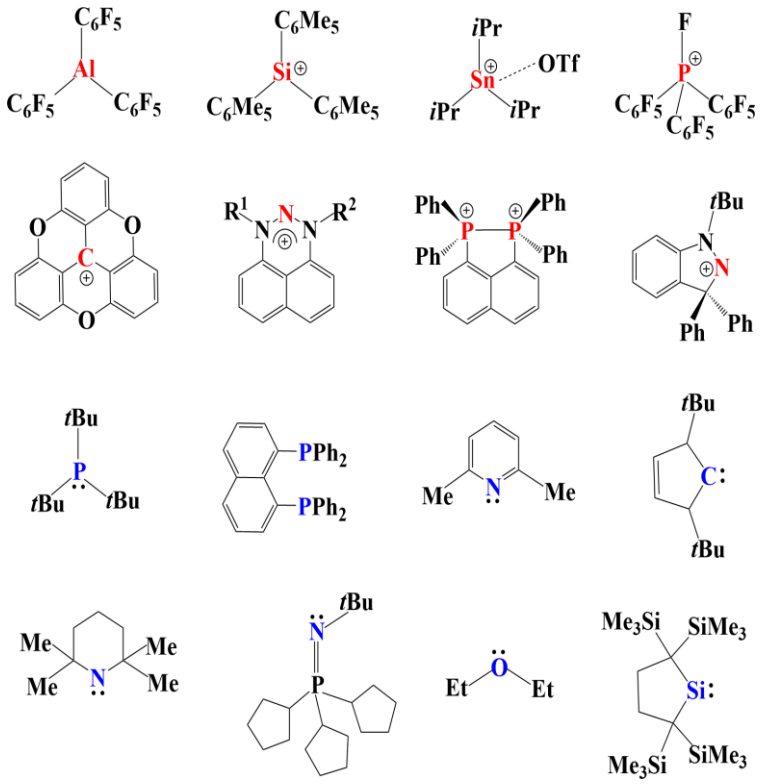

Figure 1.6: Some examples of Lewis acid (top) and Lewis bases (bottom) utilized in FLP chemistry.

bility, and distinct selectivity of FLP catalysts [32].

Along with dihydrogen activation, which becomes the hallmark of FLP chemistry, FLPs have been found to react with a plethora of small molecules like, CO_2, SO_2, N_2O, CO, NO *etc* [33-35]. Note that, many of these molecules are kinetically inert and found unreactive towards either Lewis acids or Lewis bases separately (Figure 1.7).

1.2.3 Mechanism of H_2 cleavage

The early mechanistic rationales proposed by Stephan *et al.* suggest initial coordination of H_2 with FLP either via an end-on or side-on mode, followed by a sequential action of Lewis components [20]. However, no experimental confirmation

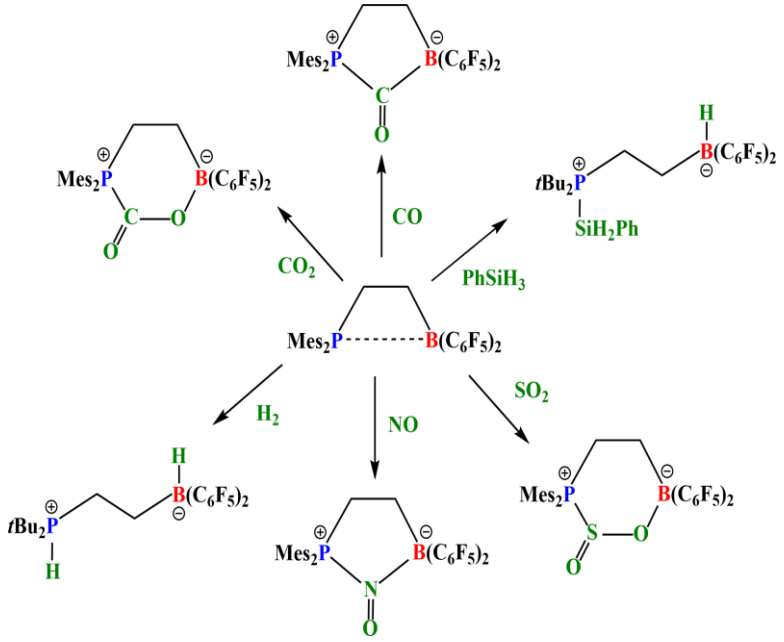

Figure 1.7: Selective examples of reaction of FLP with various small molecules.

was obtained to support such interactions, even at low temperature. Subsequently, computational studies have been performed to understand this perplexing situation of FLP-mediated H_2 activation. Contrary to the initial assumption of a van der Waals complex of dihydrogen with the LA centre, Papai and coworkers proposed the formation of a so-called encounter complex (EC), in which both the LA and LB centres are involved and held together by weak noncovalent interactions [36]. Such EC offers preorganised reaction centres for optimal interaction with dihydrogen. Molecular dynamics studies suggested that the relative concentration of the EC is extremely low under the reaction condition. For instance, at ambient temperature, the EC was predicted to be only for $tBu_3P/B(C_6F_5)_3$ in toluene solution [37]. Within this cavity, H_2 activation occurs through a concerted TS in which two cooperative electron transfer events, such as donation of electrons from the filled orbital of the LB to the σ^* antibonding molecular orbital of H_2 and from the σ molecular bonding orbital of H_2 to the empty orbital on the acceptor centre, are recognized. The cooperative action of the Lewis pairs gradually weakens the

H-H bond and subsequently, LA-H and LB-H bond formation takes place [20,38].

An alternate mechanistic model has been proposed by Grimme *et al.* where it was suggested that the H_2 molecule is polarised by the electric field generated in between the LA and LB centre [39]. This eventually breaks the H-H bond. According to this model, the entrance of the H_2 molecule inside the EC is the only energy demanding step whereas the reaction, the splitting of H_2 is said to be barrier less. Nonetheless, the reactivity of most of these FLPs reported in the literature can be explained by the former mechanistic model involving concerted electron transfer between FLP and the H_2.

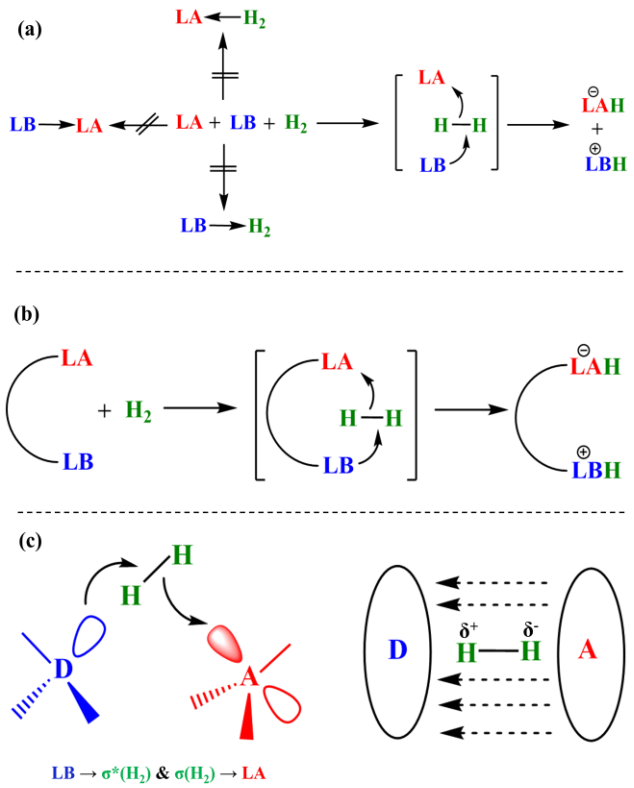

Figure 1.8: Mechanism of H_2 activation by (a) intermolecular (b) intramolecular FLPs. (c) The proposed reactivity models for heterolytic splitting of H_2.

1.2.4 Catalytic hydrogenation

Soon after the discoveries, the FLPs are used as a metal-free catalytic hydrogenation catalysts by sequential or concerted transfer of proton and hydride to an unsaturated organic substrate. In the beginning, hydrogenation of imines, aziridines and nitrile has been reported by Stephan *et al.* [40]. This has prompted numerous studies focused on hydrogenation of a wide range of organic substrates. Along with the reduction of prevailing functional groups, like alkene, alkyne, enamines, enones, silyl, enol, ethers, oxime, aziridines, nitrogen-based heterocycles, FLP hydrogenation has broadened its reach to challenging areas, such as dione Hydrogenations, amide Hydrogenations, transfer Hydrogenations, asymmetric reductions, CO_2 hydrogenation, CO hydrogenation and even N_2 reduction [41]. Recently, FLP reactivity has been used in heterogeneous catalysis also which can provide facile product separation and recyclablity of catalysts. Following the axiom of FLP chemistry, the LA/LB sites has been anchored into a porous material, such as a Zeolite or metal organic framework or they are linked with a surface [42-53]. Thus it can be said that with its roots in main group hydrogenation catalysts chemistry, the concept of FLPs is being applied across various facets in the discipline.

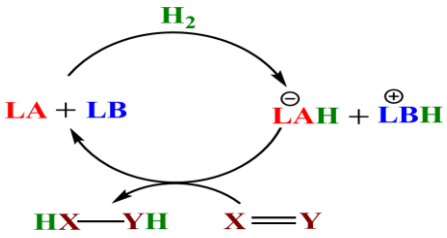

Figure 1.9: A schematic representation of FLP catalysed hydrogenation cycle.

1.2.5 Mechanism of Catalytic hydrogenation

Generally, an FLP catalysed hydrogenation cycle constitutes two key steps, first is the activation of H_2 and second is the release of active hydrogens by a sequential

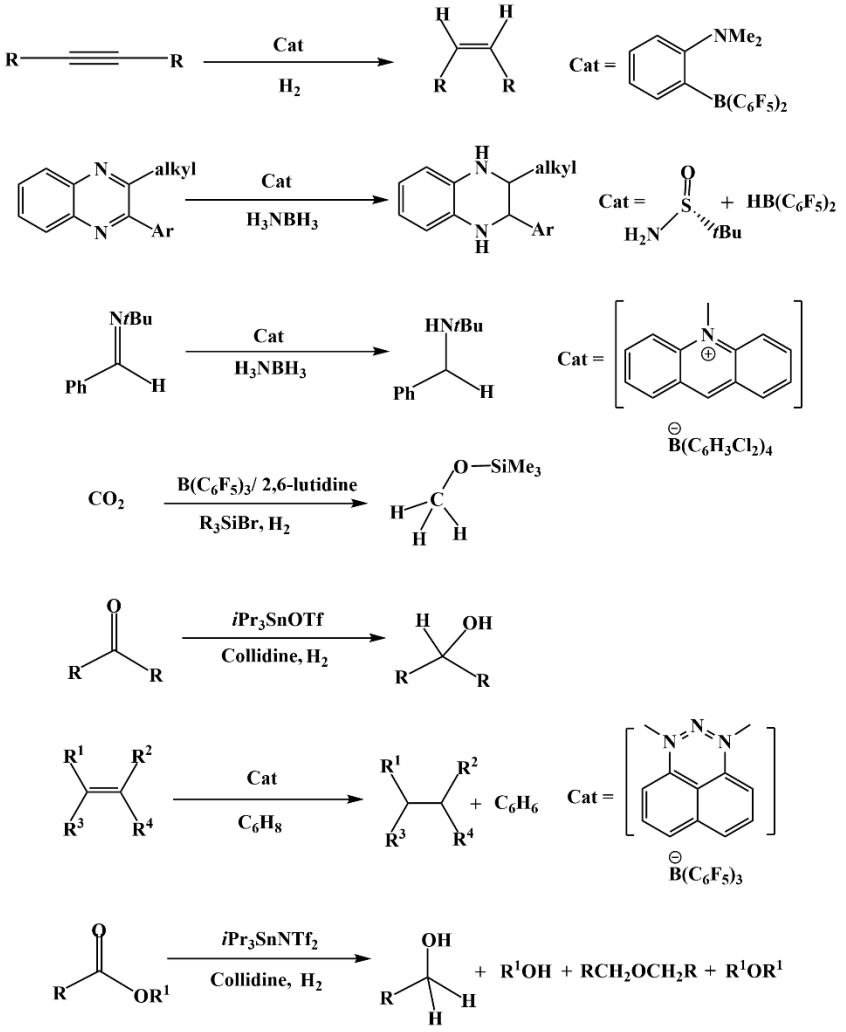

Figure 1.10: Selective examples of FLP-catalysed hydrogenation reaction.

or concerted delivery of proton and hydride to an unsaturated substrate with the regeneration of the FLP catalyst (Figure 1.9). The sequence of proton and hydride transfer depends on the FLP components. A considerable portion of FLP hydrogenation reported in literature features proton transfer prior to hydride transfer. This can be correlated with the strong electrophilic nature of boranes, which are quite omnipresent in FLP chemistry, resulting in borohydrides that are not powerful enough to transfer the hydride to the substrate [54-57]. Hence substrate activation can be achieved via full protonation or via forming hydrogen bonding

interaction with the proton, which can make it sufficiently hydridophilic. Some reports are also there where initially the substrate coordinates with another LA molecule and as a result, a hydride migration prior to proton transfer is observed [58]. At the same time, another possibility of concerted migration of proton and hydride to the substrate is also present in the FLP chemistry.

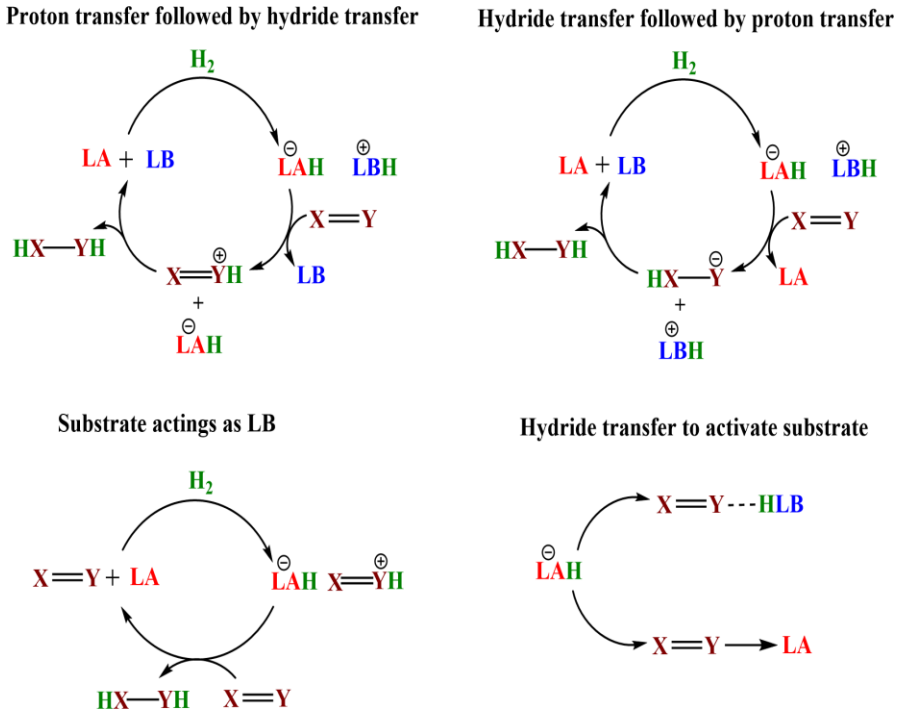

Figure 1.11: Different mechanistic pathways possible for FLP-mediated catalytic hydrogenation of an unsaturated substrate X=Y, where Y is basic site.

1.2.6 Factors controlling FLP hydrogenation

Strength of LA and LB

From the mechanistic understanding, it can easily be envisaged that the strength of Lewis components governs the feasibility of the reaction. While a strong LA and LB combination can easily split the H-H bond, it often leads to a very stable H_2 activation product, which may not be suitable for next proton/hydride delivery

hindering the hydrogenation process. On the other hand, a weak LA-LB pair is incapable of H_2 activation. Thus for effective performance, a reversible or close to reversible H_2 activation is desired. In their work on alkene hydrogenation, Stephan and Paradise used an innovative idea of using a weak fluorine-substituted phosphine base instead of a regular phosphine. This resulted in a strong Bronsted acid upon H_2 activation, which offers a facile hydrogen transfer [59]. A similar approach is observed in case of carbonyl hydrogenation where a weak LB ether is used [60]. These results highlight that for a reaction proceeding via the substrate

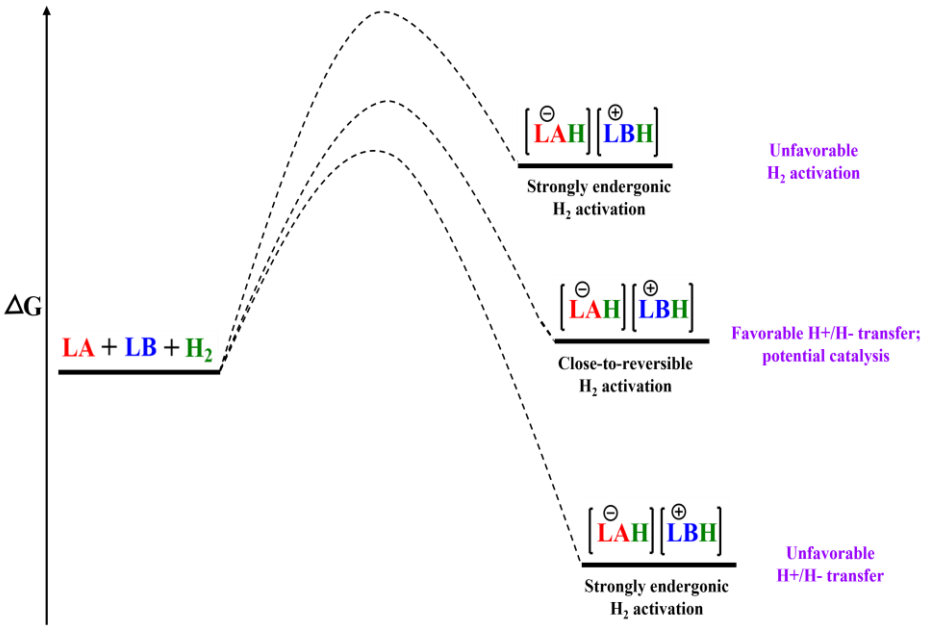

Figure 1.12: Influence of LA/LB strength on the thermodynamics of H_2 activation.

activation through protonation, which is often the case, it is crucial to balance the relative basicities of the LB and the substrate so that the protonation becomes feasible.

Steric bulk around the LA/LB centres

The basis of FLP chemistry lies in the utilization of the steric bulk to isolate the reaction centres so that they could not form an unreactive Lewis acid-base pair. However, by now it is well accepted that it is not an essential criterion to access FLP reactivity. It is observed that less bulky LAs and LBs might form a classical adduct at room temperature but at a higher temperature, it may get dissociated and give rise to the active FLP *in situ*. This behaviour is named as "thermally-induced frustration" in FLP chemistry [61]. This opens up new possibilities to access a large span of possible LA/LB combinations with different steric profiles.

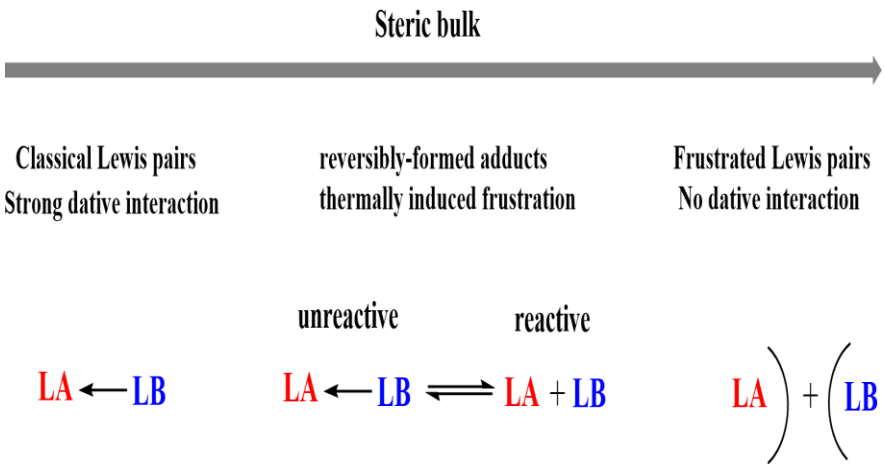

Figure 1.13: Effect of steric bulk on the LA/LB interaction.

In fact, steric bulk around the LA centre plays a crucial role in determining the functional group tolerance and substrate scope. Vanka *et al.* demonstrated that less bulky FLP combinations are better hydrogenation catalysts [62]. Thus it can be said that a less bulky LA forms a more reactive $[LA\text{-}H]^-$ facilitating the hydride transfer step while excessively bulky $[LA\text{-}H]^-$ might make this step kinetically inaccessible.

Intermolecular or Intramolecular FLP

As discussed from the beginning of this field, both intermolecular and intramolecular molecules have been expoited. It can be expected that due to the reduced entropic barrier of the bimolecular reaction with H_2 compared to the intermolecular step, the intramolecular FLPs can show superior catalytic performance. Erker *et al.* reported similar result, where the activity of an ethylene-linked intramolecular P/B FLP surpass the previous intermolecular P/B FLPs [63]. However it is soon realized that the activity of such systems is dependent on the nature of the linker used to tether the LA and LB centres. For example, the intramolecular FLP $Mes_2P(CH_2)_nB(C_6F_5)_2$ shows catalytic activity when n=2,3 but n=3 linker turned out to be inactive in this regard [64].

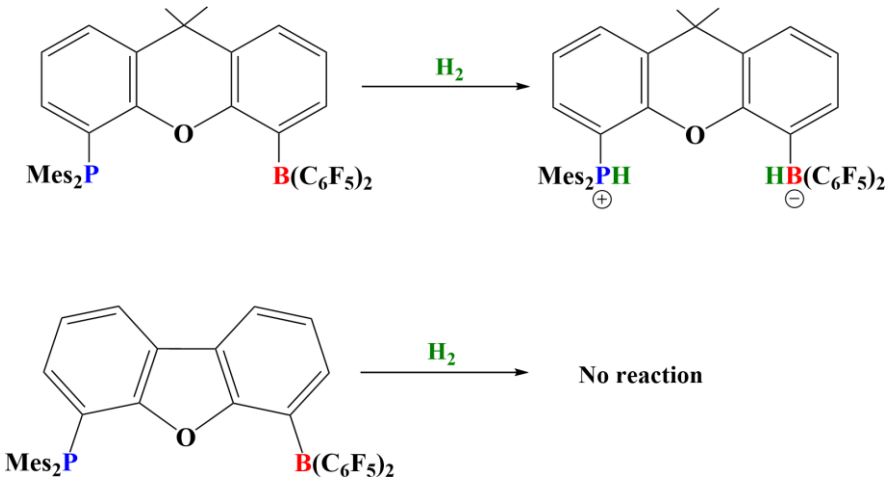

Figure 1.14: Reactivity of two intramolecular phosphine/borane FLPs with slightly different linkers.

Aldridge *et al.* reported similar observation that while a dimethylxanthene-linked P/B FLP is a successful candidate for H_2 activation, identical dibenzofuranlinked system renders the reaction (Figure 1.14) [65]. Note that, the very first FLP, $Mes_2PC_6F_4B(C_6F_5)_2$ reacts with H_2 in an intermolecular manner due to the rigid tetrafluorophenylene linker which does not allow the active centres to come

to close proximity [19,66]. Thus the choice of the linker is a crucial point in designing effective intramolecular FLP hydrogenation catalyst. On the other side, the LAs and LBs components of intermolecular FLPs can easily be tuned. In fact mechanistic investigation are often easier with intermolecular FLPs and therefore screening of a large number of combinations is possible in this class of FLPs.

1.3 N-Heterocyclic Carbenes (NHC)

Another class of compounds that has drawn significant attention of main-group chemists is the N-Heterocyclic Carbenes (NHC). NHCs are a class of carbenes compound which has a neutral divalent carbon atom directly attached to at least one nitrogen within a heterocyclic framework [67]. In 1988, Bertrand and coworkers synthesized the first stable acyclic (phosphino)(silyl)carbene [68]. However, in 1991 the first "bottle-able" imidazolin-2-ylidene was introduced by Arduengo *et al.* [69]. After this outstanding discoveries, numerous carbene compounds have been reported in literature. Among them, NHC is the most extensively studied as ligands in transition metal chemistry and catalysis [70], in f-block element chemistry [71] as well as in organocatalysts [72]. However, the unstable NHCs frequently undergo dimerisation, resulting in the formation of a double bond between the C1 positions. Later Goddard *et al.* and Thielet al. have shown the energetic gap between the singlet and triplet states of a carbene largely controls the propensity of the carbene dimerization [73,74]. The singlet state of NHC, which is practically used in organocatalysis and organometallic chemistry, is stabilised by electron donation from the adjacent nitrogen atom to the vacant 2p orbital of the C1 carbon. Specifically, the σ electron withdrawing and π electron donating effects of nitrogen atom(s) of the NHC scaffold decreases the energy of the HOMO which is the lone pair containing sp^2 orbital and increase the energy of LUMO which is the p_π orbital. As a result, the energy gap between these orbitals and therefore the

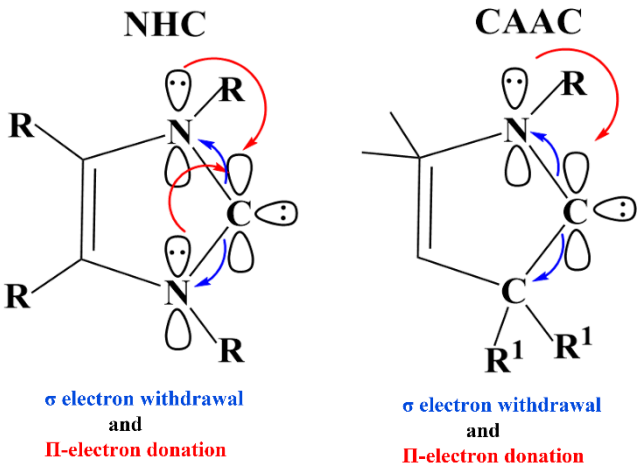

Figure 1.15: The electronic effects involved in NHC and CAAC.

singlet-triplet gap increases. This leads to a better stability and high nucleophilicity for the NHC ligand. In this regard, the cyclic (alkyl)(amino)carbenes, (CAACs) has been introduced where in place of an adjacent nitrogen, a σ-donating quaternary carbons is present. CAAC has slighly higher energy HOMO compared to classical NHC and therefore a lower HOMO-LUMO gap and thus lower singlet-triplet energy gap (Figure 1.13). As a result, CAACs exhibit stronger σ-donating and enhanced π-accepting properties (a better nucleophile and electrophile). This directly reflects in their unique chemical reactivity discussed as follows.

1.3.1 Activation of small molecules

It is observed that while acyclic and cyclic bis(amino)carbenes, are inert towards small molecules [76], the (alkyl)(amino)carbenes, cAAC1 and aAAC1 can act as single-site molecules for capturing small molecules like CO, NH_3 and can split H-H bond under mild condition (Figure 1.14). This behaviour can be attributed by the smaller singlet triplet energy gap and higher energy HOMO of CAAC which makes them stronger nucleophile as well as better electrophile, thus better suited for TM-like behavior [75]. However, the frontier orbital picture of H_2 activation

by TMs and mono-(amino)carbenes are quite different. As previously discussed in case of TMs, the H_2 splitting is initiated by the interaction of a empty d orbital of TM with σ orbital of H_2. Whereas in case of carbenes, the splitting of H-H bond primarily begins by the nucleophilic interaction of carbene's lone pair with the σ orbital of H_2 followed by a hydride transfer.

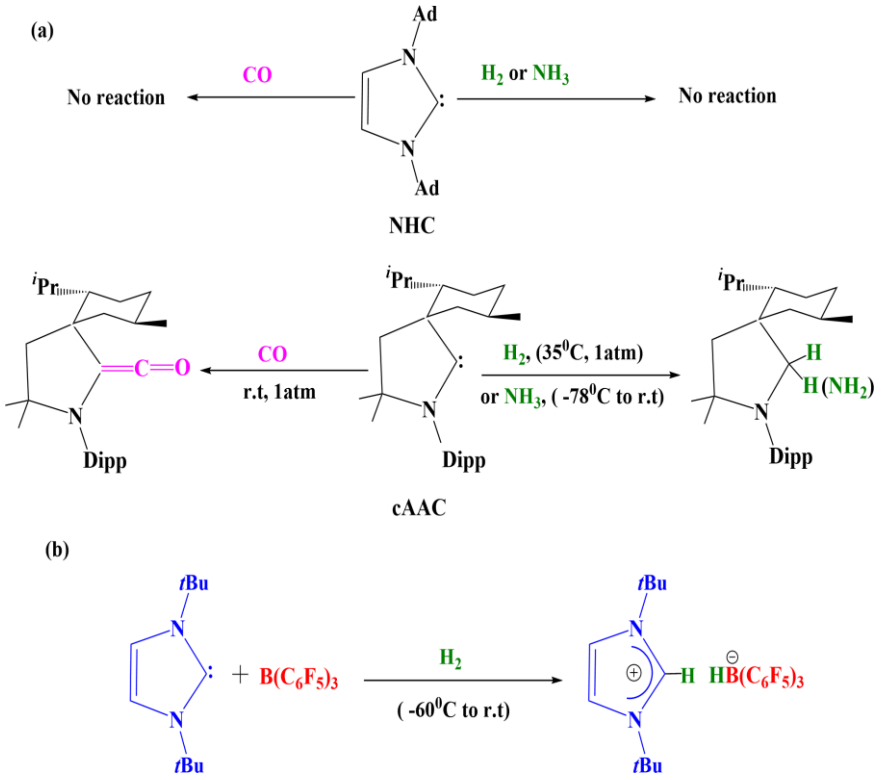

Figure 1.16: (a)Reaction of NHCs with various small molecules (b) NHC as Lewis base in FLP mediated H_2 activation.

Inspired by this strong nucleophilic character of NHC, it has been utilized as a Lewis base in FLP chemistry and has been combined with various barane Lewis acid. Interesting examples are combination of $B(C_6F_5)_3$ and 1,3-di-tert-butyl-1,3-imidazol-2-ylidene (I*t*Bu), which can perform H_2 activation[77,78], ring opening of THF [78], activation of NH_3, amine and aniline *etc* [77].

1.3.2 Stabilization of reactive main group species

By virtue of the strong σ-donating ability, NHC ligands provide excellent stabilization to the electron-deficient main group elements. This opens up a wide opportunity to access the low-coordinate elements with different oxidation states. Therefore, opportunity also is opened up for exploration of their reactivity and potential in synthesis and catalysis.

1.4 Computational methodology

1.4.1 General aspects

It is needless to say the current state of the art computational methodology and computer technologies is quite fascinating. However modelling a chemical reaction in solution phase is still a challenging task. Thus investigation of any reaction mechanism of a catalytic cycle is quite tricky. Along with the inherent factors like charge, oxidation state, coordination as well as the spin states of the reaction intermediates, other external parameters like solvent, additives impose additional complicacy in the study. Particularly solvent may have a significant influence on the reaction mechanism. It can simply perturb the potential energy profile as well can actively involve in the reaction steps. For example, a polar solvent or a protic solvent can stabelise the reaction intermediates through hydrogen bonding interaction. Another important parameter is the steric and electronic environment of the catalyst active site which generally play a crucial role in determining the reactivity and selectivity of the reaction.

In this thesis, based on the nature of the reaction studied and considering the available computational resources, a static approach is taken to investigate the potential energy surface (PES) of the reaction. Quantum chemical calculations at the framework of density functional theory have been used to locate the stationary points like reactants, products, intermediates and transition states on the PES. Next the nature of these stationary points are characterized by a harmonic vibrational frequency analysis. The respective Transition states (TSs) are further verefied by performing intrinsic reaction coordinate (IRC) calculations which connect the TS to the desired minima on either side of the saddle point. Most of the TS search calculations are performed by relaxed scan calculations where all degrees of freedom are fully relaxed except a single geometric variable (reaction

coordinate) which is scanned in a stepwise manner.

The solvent effects are taken into account by considering a dielectric continum model for solvation. Generally, the solvents used in the reactions are aprotic in nature, any active participation of the solvent molecule in the reaction mechanism can be ruled out. Only in chapter 5 we have studied the explicit role of the solvent molecule in the reaction mechanism. Note that, the present computational approach is not expected to result a very accurate value of Gibbs free energies. The uncertainties in calculating the free energy values lies in the two main sources (1) the ideal gas-rigid rotor-harmonic oscillator model used to estimate the gas phase entropic contributions and (2) the empirical ingredients of the SMD solvation model used for the solvent corrections. However, in this thesis, we kept all these factors in account and we aim to identify the key mechanistic features, understand the underlying principles as well as rationalize experimental observations that may provide useful insight for the future direction. For this purpose, we think that the present computational framework is reasonble.

1.4.2 Electronic structure calculations

The basis of any electronic structure calculation is the Schrödinger equation. The non-relativistic time-independent Schrödinger equation (SE) is

$$\hat{H}\Psi(R,r) = E\Psi(R,r) \tag{1.1}$$

where ($\hat{H}$) is the Hamiltonian operator, Ψ(R,r) is the many body wavefunction which store all kind of characteristics of the system and E is the total energy. The complete Hamiltonian for an interacting system read as,

$$\hat{H} = -\frac{1}{2}\sum_{i=1}^{N}\nabla_i^2 - \sum_{k=1}^{K}\frac{1}{2M_k}\nabla_k^2 - \sum_{i=1}^{N}\sum_{k=1}^{K}\frac{Z_k}{|r_i - R_k|} + \frac{1}{2}\sum_{i\neq j}^{N}\frac{1}{|r_i - r_j|} + \frac{1}{2}\sum_{k\neq I}^{K}\frac{Z_k Z_I}{|R_k - R_I|} \tag{1.2}$$

This can be represented in a much simpler way which is

$$\hat{H} = \hat{T}_e + \hat{T}_n + \hat{V_{en}} + \hat{V_{ee}} + \hat{V_{nn}} \tag{1.3}$$

In the above equation, the first term is the kinetic energy of N number of electrons, second term is kinetic energy of L number of nuclei, third, fourth and fifth terms are the potential energies corresponding to nuclei-electron, electron-electron, nuclei-nuclei interactions respectively.

1.4.3 Born-Oppenheimer Approximation

Unfortunately, it is impossible to obtain an exact solution to Schrödinger equation and thus many approximations are applied to simplify the many-body Hamiltonian. The first such approximation is Born-Oppenheimer approximation, also familiar as adiabatic approximation, allows to decouple the dynamics of nuclei and electrons because the nuclei are about thousand times heavier than electrons. Hence it can be assumed that nuclei remain static with respect to electron time scale. Hence time-independent Schrödinger equation (SE) can be written for electronic degrees of freedom in the presence of stationary nuclear part. The modified electronic Hamiltonian is,

$$\hat{H_e} = \hat{T}_e + \hat{V_{en}} + \hat{V_{ee}} \tag{1.4}$$

Thus Born-Oppenheimer approximation reduces the complexity of the many-body Hamiltonian to some extent by separating the nuclear and electronic degrees

of freedom.

1.4.4 Density Functional Theory

Even after application of Born-Oppenheimer Approximation, solution of the many-body SE equation is far from trivial. Nonetheless, density functional theory (DFT) introduced a different approach by replacing wave function with the electron density of the system to obtain the ground state electronic properties. This method was first proposed in 1960s in two seminar papers by Hohenberg-Kohn. This *ab initio* (first principles) based method has gradually drawn attention as it is capable of mapping a complicated interacting problem to an easier non-interacting problem with replacement of the number of degrees of freedom, 3N (N is number of quantum particles) to only 3 spatial coordinates.

Hohenberg-Kohn Theory

At the heart of DFT, there lies two ingeniously simple theorems put forward by Hohenberg and Kohn introduced in 1964 [79,81].

Theorem-I [Uniqueness] "For any system of interacting particles in the presence of an external potential $V_{ext}(r)$, the potential $V_{ext}(r)$ can be uniquely determined, upto an additive constant, by the ground state density $n_0(r)$." In other words, the total ground state energy of a system is a unique functional of its density, E[n(r)], hence we can write:

$$E[n(r)] = \langle \Psi[n(r)] | H | \Psi[n(r)] \rangle \tag{1.5}$$

Theorem-II [Variational Theory] "A functional which is universal for he energy E[n] in terms of density n(r) can be defined, valid for any external potential $V_{ext}(r)$. For any particular $V_{ext}(r)$, the exact ground state energy of the system

defines the global minimum value for this functional, and the density which minimizes the functional is the exact ground state density $n_0(r)$". The energy can be expressed as a sum of kinetic energy part (T[$n(r)$]), electrostatic energy part (U[$n(r)$]) and energy due to non-interacting electrons moving under external potential:

$$E[n(r)] = T[n(r)] + U[n(r)] + \int [V(r)n(r)d^3r] \tag{1.6}$$

Here the first two terms are independent of external potential and can be written in the form of universal functional of the electron density:

$$T = \frac{3}{10}\int [3\pi^2 n(r)]^{\frac{2}{3}} n(r)dr \tag{1.7}$$

$$U = \frac{1}{2}\int \frac{n(r)}{|r - r'|} dr'dr \tag{1.8}$$

The expression of kinetic energy is however inaccurate and moreover, the deduction of the functional of the interacting systems is not very clear. However, this is solved by Kohn and Sham in 1965 by providing a an indirect approximate approach to calculate energy functional E[n(r)]. In fact, it is the Kohn-sham formalism that puts DFT to practical use.

Kohn-Sham approach

Kohn and Sham considered a uniform electron density from 3d non-interacting electron gas and iteratively solved the Kohn-Sham equation. They considered, as a first approximation, a fictitious system of non-interacting electrons instead of a real system of interacting electrons having the same electron density [80]. This theorem is enabled to calculate energy and other electronic properties of only the ground state. Having the same electron density leads to same ground state energies and other electronic properties. Since electrons are not interacting with each other, Kohn-Sham equation can be considered as a set of single particle

equations, which are simpler to handle than coupled Schrödinger equation, which becomes extremely difficult to solve for a large system size with huge number of electrons. The interacting part of the energies has been taken care of in terms of exchange-correlation and energy is written in terms of density:

$$E_{[n(r)]} = T_{[n(r)]} + E_{ext[n(r)]} + \frac{1}{2}\int \frac{n(r)}{|r - r'|} + V_{xc[n(r)]} \tag{1.9}$$

In the above equation, the first term is kinetic energy of only non-interacting electrons, second term is classical Coulomb interaction between nuclei and electron, third term is classical electron-electron interactions also known as Hartree interaction, the final term is exchange-correlation including the non-classical electrostatic interaction energy between electrons and the difference of energy between non-interacting and interacting kinetic energy of electron. The main idea behind this approach is that the first three terms can be dealt with simply and last term can be modified with better approximations.

Exchange-Correlation Functionals

The kohn-Sham formalism simplifies the fully-interacting many-body problem into a set of independent particle SEs. However, it is only possible if the exact form of exchange-correlation functional, $v_{xc[n(r)]}$ is known. The exchange-correlation functionals include two different kinds of electronic interactions; the exchange part comes because of fermionic nature of the electrons. The antisymmetrically paired electrons exchange with each other following Pauli exclusion principle. The other term i.e. correlation term arises from the effect of other electrons on kinetic and potential energy. The exact form of each interactions is still unknown. Nevertheless, even with gross approximations of the $v_{xc[n(r)]}$, it is possible to predict various properties of systems to a fair degree of accuracy. Since the accuracy of calculation depends on the exchange-correlation functionals, various modifications have been

done over the time and here we will discuss a few which has been extensively used in the literature.

Local density approximation (LDA)

LDA is the simplest approximation in DFT. In LDA the XC energy per electron is approximated to be same as the XC energy of a homogeneous electron gas of exactly same density [82]. Thus it can be expressed as,

$$E_{ex(n)}^{LDA} = \int e_{xc}(n(r)n(r)dr \tag{1.10}$$

Inspite of being an extensive crude approximation, it works reasonably well for solid systems. However, when the density varies rapidly, for inhomogeneous systems LDA performs poorly. For example, in the case of defects in the solid LDA makes inaccurate predictions. Similarly it often overestimates the binding energy and underestimates the ground state energies, ionization energies and band gaps of semiconductor.

Generalized gradient approximation

To account for inhomogeneity of the system, several modifications have been made beyond LDA. The apparent improvement to LDA is to consider density as well as gradient of density at a given point, which leads to the GGA exchange-correlation functional.

$$E_{ex(n)} = \int e_{xc}(n(r), |\partial n(r)|)n(r)dr \tag{1.11}$$

There are several approaches which can be included within GGA calculations. Three commonly used forms are proposed by Becke [83], Perdew *et al.* and Perdew, Burke and Enzerhof [83] (PBE). GGA shows significant improvement over LDA results in predicting structural parameters, binding energies. However, sometimes it tends to overcorrect LDA results as in ionic cryctals in which the later is found to give better results compared to GGA. Several better modifications have been

introduced to GGA resulting in meta-GGA, hybrid functionals. This functionals have been modified by considering both the electronic density and individual electronic wavefunctions to compute the energy and other properties.

Meta-GGA functionals

The next level of improvement on GGA can be obtained using the Laplacian of density along with the density gradient and density itself. These are called meta-GGA functionals, which often works well over GGA in many areas [84,85].

Hybrid functionals

In this line the hybrid functionals are also introduced which attempts to correct the self-interaction error in LDA/GGA by including a certain portion of exact non-local Hartree-Fock exchange along with XC description from other sources like LDA or GGA. The extensively used functional B3LYP [86] is an example of hybrid functional.

Long-range corrected functionals

The LDA and GGA functionals neglect the long-range electron-electron exchange interaction, which can not possibly be represented by a functional of one-electron quantity. Thus, these functionals are not suitable for modelling processes such as van der Waals interactions or non-covalent interactions. Various long-range exchange correction methods have been proposed to account these issues. Few examples of long-range corrected functionals are ωb97xd [87] and CAM-B3LYP [88].

1.5 Softwares used:

several software packages have been used to obtain the reported results in this thesis. All electronic structure calculations performed under the framework of DFT, geometry optimization, vibrational analysis, thermochemical data and solvent corrections are carried out using the Gaussian package (G16 A.03). NBO 3.1 package is used for bonding analysis. The energy decomposition analysis is per-

formed using ADF2017.01. For visualization and graphical analyses, we have used Gaussview, Chemcraft, Xmgrace. Whenever necessary, home-developed codes are used to analyse the computed values from these softwares.

1.6 Scope of the thesis

In this thesis, we primarily dealt with reduction reactions which are catalysed by various main-group element species. We aimed to get a molecular level understanding of how this main-group catalysts work. By using quantum chemical calculations at various levels of density functional theory, we have explored the relevant potential energy surface and identify the key intermediates of the corresponding reaction. The thesis commences with the study of the hydrogenation of a N-heterocycle quinoline by a NHC stabilised borenium cation. In the subsequent next two chapters we discussed the hydrogen activation and hydrogenation reaction by a series of tetrel based neutral geminal FLPs. Chapter 3 answer the mechanism of H_2 activation by these intramolecular FLPs. In chapter 4 we have explored these geminal FLPs as possible hydrogenation catalysts. Chapter 5 deals with a comprehensive mechanistic understanding on the reduction of CO_2 by a Lewis pair working in tandem with a copper catalyst. In chapter 6 we have explored the detailed mechanism of reductive functionalization of CO_2 with amide. Finally chapter 7 deals with a series of stibenium cations as a hydroboration and cyanosilylation catalysts for carbonyl compounds. The thesis ends with a brief summary of the results and an outlook towards the possible future research and development.

1.7 References

[1] Doman, L.E.; Arora, V.; Singer, L.E.; Zaretskaya, V.; Jones, A.; Huetteman, T.; Bowman, M.; Slater-Thompson, N.; Hojjati, B.; Peterson, D.; Gross, P. International energy outlook. US Energy Information, Administration 2016

[2] Sabatier, P. Industrial Engineering Chemistry 1926, 18,1005-1008.

[3] Osborn, J. A.; Jardine, F.;Young, J. F.; Wilkinson, G. Journal of [4] Kim, H.S.; Liu, W.; Ren, Z. The bridge between the materials and devices of thermoelectric power generators. Energy Environmental Science 2017, 10(1), 69-85.

[5] Power P. P. Nature 2010, 463,171.

[6] Davidson, P. J.; Lappert M. F. J. Chem. Soc. Chem. Commun. 1973, 317.

[7] West, R.; Fink, M. J.; Michl, J. Science 1981, 214,1343.

[8] Yoshifuji, M.; Shima, I.; Inamoto, N.; Hirotsu, K.; Higuchi, T.; J. Am. Chem. Soc. 1981, 103, 4587-4589.

[9] Brook, A. G.; Abdesaken, F.; Gutekunst, G.; Kallury, R. K.; J. Chem. Soc. Chem. Commun. 1981, 191-192.

[10] Chu, T.; Nikonov, G. I.; Chem. Rev. 2018, 118, 3608-3680.

[11] Yadav, S.; Saha, S.; Sakya, S. S. ChemCatChem 2015, 8, 486-501.

[12] Spikes, G. H.; Fettinger, J. C.; Power, P. P. Journal of the American Chemical Society 2005, 127, 12232-12233.

[13] Peng, Y.; Brynda, M.; Ellis, B. D.; Fettinger, J. C.; Rivard, E.; Power, P. P. Chemical Communications 2008, 6042-6044.

[14] Lewis, G. N. Valence and the Structurs of Atoms and Molecules; Chemical Catalog Com.; New York, 1923.

[15] Brown, H. C.; Schlesinger, H.; Cardon, S. Z. Journal of the Americal Chemical Society 1942, 64, 325-329.

[16] Brown, H. C.; Kanner, B.; Journal of the Americal Chemical Society 1966,88, 986-992.

[17] Wittig, G.; Ruckert, A. Justus Liebigs Annalen der Chemie 1950, 566, 101-113.

[18] Tochtermann, W. Angewandate Chemie International Edition in English 1966, 5, 351-371.

[19] Welch, G. C.; San Juan. R. R.; Masuda, J. D.; Stephan, D. W. Science 2006, 314, 1124-1126.

[20] Welch, G. C.; Stephan, D. W. Journal of American Chemical Society 2007, 129, 1880-1881.

[21] Spies, P.; Erker, G.; Kehr, G.; Bergander, K.; Frohlich, R.; Grimme, S.; Stephan, D. W. Chemical Communications 2007,5072-5074.

[22] Welch, G, C.; Cabrera, L.; Chase, P. A.; Hollink, E.; Masuda, J. D.; Wei, P.; Stephan, D. W. Dalton Transactions 2007,3407-3414.

[23] Stephan, D. W. A primer in Frustrated Lewis Pair Hydrogenation.

[24] Weicker, S. A.; Stephan, D. W. Bulletin of Chemical Society Japan 2015, 88, 8,1003-1016.

[25] Sarkar, P.; Das, S,; Pati, S. K. Chemistry An Asian Journal 2022, 12, 202200148,1-12.

[26] Farrell, J. M.; Hatnean, J. A.; Stepahn, D. W. Journal of the Americal Chemical Society 2012, 134,15728-15731.

[27] Schafer, A.; Reibmann, M.; Schafer, A.; Schmidtmann, M.; Muller, T. Chemistry An Europian Journal 2014, 20, 9381-9386.

[28] Menard, G.; Stephan, D. W.; Angewandate Chemie International Edition 2012, 51, 8272-8275.

[29] Stein, T.; Perez, M.; Dobrovetsky, R.; Winkelhaus, D.; Caputo, C. B.; Stephan, D. W. Angewandate Chemie International Edition 2015, 54.10178-10182.

[30] Clark, E. R.; Ingleson, M. J. Angewandate Chemie International Edition 2014, 126,11488-11491.

[31] Metters, O. J.; Forrest, S. J.; Sparkes, H. A.; Manners, I.; Wass, D. F. Journal

of the Americal Chemical Society 2016, 138, 1994-2003.
[32] Stephan, D. W. Journal of the Americal Chemical Society 2021, 143, 20002-20014.
[33] Stephan, D. W.; Erker, G. Chemical Science 2014, 5, 2625-2641.
[34]Stephan, D. W.; Erker, G. Angewandate Chemie International Edition 2010,49, 46-76.
[35] Stephan, D. W.; Erker, G. Angewandate Chemie International Edition 2014, 48, 306-316.
[36] Rokob, T. A.; Hamza, A.; Stirling, A.; SooS, T.; Papai, I. Angewante Chemie International Edition 2008,47, 2435-2438.
[37] Bako, I.; Stirling, A.; Balint, S.; Papai, I. Dalton Transactions 2012,41,9023-9025.
[38] Hamza, A.; Stirling, A.;Andras Rokob, T.; Papai, I. International Journal of Quantum Chemistry 2009,109,2416-2425.
39 Grimme, S.; Kruse, H.; Goerigk, L.; Erker, G. Angewante Chemie International Edition 2010, 49, 1402-1405.
[40] Chase, P.A.; Welch, G.C.; Jurca, T.; Stephan, D. W. Angewante Chemie International Edition 2007, 46, 8050-8-53.
[41] Stephan, D. W. Journal of American Chemical Society 2021, 143, 20002-20014.
[42] Lee, H.; Choi, Y. N.; Lim, D. W.; Rahman, M. M.; Kim, Y. I.; Cho,I. H.; Kang, H. W.; Seo, J. H.; Jeon, C.; Yoon, K. B.Angewante Chemie International Edition 2015,54 (44), 1308013084.
[43] Ye, J. Y.; Johnson, J. K. Catalysis Science Technology 2016, 6, 83928405.
[44] Heshmat, M. Journal of Physical Chemistry C 2020, 124, 1095110960.
[45] Yang, K.; Jiang, J.Journal of Material Chemistry A 2020, 8, 2280222815.
[46] Niu, Z.; Bhagya-Gunatilleke, W. D. C.; Sun, Q.; Lan, P. C.; Perman, J.; Ma, J.-G.; Cheng, Y.; Aguila, B.; Ma, S. Chem. 2018, 4, 25872599.
[47] Bromberg, L.; Diao, Y.; Wu, H.; Speakman, S. A.; Hatton, T. A. Chemistry

of Materials 2012, 24, 16641675.

[48] Niu, Z.; Zhang, W.; Lan, P. C.; Aguila, B.; Ma, S. Angewante Chemie International Edition 2019, 58, 74207424.

[49] Li, X.; Deng, Q.; Yu, L.; Gao, R.; Tong, Z.; Lu, C.; Wang, J.; Zeng, Z.; Zou, J.-J.; Deng, S. Green Chem. 2020, 22 (8), 25492557.

[50] Lu, G.; Zhang, P.; Sun, D.; Wang, L.; Zhou, K.; Wang, Z.-X.; Guo, G.-C. Chemical Science 2014, 5, 1082.

[51] Almora-Barrios, N.; Cano, I.; van Leeuwen, P. W. N. M.; Lopez, N. ACS Catalysis 2017, 7, 39493954.

[52] Fiorio, J. L.; Lopez, N.; Rossi, L. M. ACS Catalysis 2017, 7, 29732980.

[53] Wang, L.; Yan, T.; Song, R.; Sun, W.; Dong, Y.; Guo, J.; Zhang,Z.; Wang, X.; Ozin, G. A. Angewante Chemie International Edition 2019, 58,95019505.

[54] Tussing, S.; Greb, L.; Tamke, S.; Schirmer, B.; Muhle-Goll, C.; Luy,B.; Paradise, J. Chemistry-A European Journal 2015,21,8056-8059. .

[55] Tussing, S.; Kaupmees, K.; Paradise, J.; Chemistry-A European Journal 2016,22,7422-7426.

[56] Greb, L.;Tussing, S.; Schirmer, B.; Ona-Burgos, P.; Kaupmees, K.; Lokov,M.; Leito, I.; Grimme, S.; Paradise, J. Chemical Science 2013, 4, 2788-2796.

[57] Whittemore, S. M.; Aytrey, T. Israel Journal of Chemistry 2015, 55, 196-201.

[58] Scott, D. J.; Phillips, N. A. Sapsford, J. S.; Deacy, A. C.; Fuchter, M. J.; Ashley, A. E. Angewante Chemie 2016, 128,14958-149624.

[59] Greb, L.; Ona-Burgos, P.; Schirmer, B.; Grimme, S.; Stephan, D. W.; Paradise, J. Angewante Chemie 2012, 124, 10311-10315.

[60] Scott, D. J.; Fuchter, M. J.; Ashley, A. E. Journal of the American Chemical Society 2014, 136, 15813-15816.

[61] Rokob, T. A.; Hamza, A.; Stirling, A.; Papai, I.; Journal of the American Chemical Society 2009, 131, 2029-2036.

[62] Mane, M. V.; Vanka, K. ChemCatChem 2017, 9, 3013-3022.

[63] Spies,P.; Schwendemann, S.; Lange, S.; Kehr, G.; Frohlich, R.; Erker, G.; Angewante Chemie International Edition, 2008, 47, 7543.

[64] Ozgun, T.; Ye, K.-Y.; Daniliuc, C. G.; Wibbeling, B.; Liu, L.; Grimme, S.; Kehr, G.; Erker, G. Chemistry an Europian Journal, 2016, 22, 5988.

[65] Mo, Z. ; Kolychev, E. L.; Rit, A.; Campos, J.; Niu, H.; Aldridge, S. Journal of the American Chemical Society 2015, 137, 12227 .

[67] Hopkinson, M. N.; Richter, C.; Schedler, M.; Glorius, F. Nature 2014 , 510 , 485 496.

[68] Igau, A.; Grutzmacher, H.; Baceiredo, A.; Bertrand, G. Journal of American Chemical Society 1988 , 110 , 6463 6466.

[69] Arduengo, A. J.; Harlow, R. L.; Kline, M. Journal of American Chemcal Society 1991 , 113 , 361 363.

[70] D´ıezGonzalez, S. N-Heterocyclic Carbenes: From Laboratory Curiosities to Efficient Synthetic Tools (2) ; Royal Society of Chemistry: UK, 2017.

[71] Arnold, P. L.; Casely, I. J. Chem. Rev. 2009 , 109 , 3599 3611.

[72] Flanigan, D. M.; Romanov-Michailidis, F.; White, N. A.; Rovis, T. Chem. Rev. 2015 , 115 , 9307 9387.

[73] Carter, E. A.; Goddard, W. A. Journal of Physical Chemistry 1986,90,998-1001.

[74] Heinemann, C.; Thiel, W. Chemical Physics Letters 1994, 217, 11-16.

[75] Frey, G. D.; Lavallo, V.; Donnadieu, B.; Schoeller, W. W., Bertrand, G. Science, 2007, 316, 439–441.

[76] Denk, M. K.; Rodezno, J. M.; Gupta, S.; Lough, A. J. Journal of Organometalic Chemistry, 2001, 617, 242–253.

[77] Chase, P. A.; Stephan, D. W. Angewante Chemie International Edition 2008, 47, 74337437.

[78] Holschumacher, D.; Bannenberg, T.; Hrib, C. G.; Jones, P. G.; Tamm, M. Angewante Chemie International Edition 2008, 47, 74287432.

[79] Hohenberg, P.; Kohn, W. Phys. Rev. 1964, 136, B864-B871.

[80] Kohn, W.; Sham, L. J. Phys. Rev. 1965, 140, A1133-A1138.

[81] Kohn, W. Rev. Mod. Phys. 1999, 71, 1253-1266.

[82] Perdew, J. P.; Burke, K.; Ernzerhof, M. Physical review letters 1996, 77, 3865.

[83] Perdew, J. P.; Chevary, J. A.; Vosko, S. H.; Jackson, K. A.; Pederson, M. R.; Singh, D. J.; Fiolhais, C. Physical Review B 1992, 46, 6671.

[84] Zhao, Y.; Truhlar, D. G.; Theor. Chem. Acc. 2008, 120, 215-241.

[85] Zhao, Y.; Truhlar, D. G.; J. Phys. Chem. A 2006, 110, 13126-13130.

[86] Becke, A. D. J. Chem. Phys. 1993, 98,5648-5652.

[87] Chai, J.-D.; Head-Gordon, M. Phys. Chem. Chem. Phys 2008, 10, 6615-6620.

[88] Yanai, T.; Tew, D. P.; Handy, N. C. Chem. Phys. Lett. 2004, 393, 51-57.

2

Mechanistic Insight into the Stepwise Hydrogenation of N-heterocycles Catalysed by NHC Stabilized Borenium ion

Work reported in this chpater is based on: Subir Maji, Pallavi Sarkar, Arpan Das, Swapan K Pati, Swadhin K Mondal, Inorganic Chemistry (under revision).

2.1 Introduction

Catalytic hydrogenation is one of the most fundamental transformations in chemistry that has wide applications in the chemical industry to laboratory scale organic synthesis [1,3]. For this transformation, molecular hydrogen is considered as an ideal, atom economic and green reducing agent [4-10]. Over the last decade use of Frustrated Lewis pairs (FLPs) as hydrogenation catalysts provide a significant advancement in the area of transition metal-free hydrogenation [11-17]. Among the several forms of FLP catalysts, the hydrogenation using a boron-based Lewis acid (LA) particularly $B(C_6F_5)_3$ is very attractive [18]. Previous reports show that $B(C_6F_5)_3$ can perform hydrogenation reaction even without the use of an auxillary ligand and the substrate can act as Lewis base (LB) for this reaction [19]. However,the presence of such electron-withdrawing substituents hinders hydride delivery and thus slows the catalysis [20]. Moreover, preparing derivatives of such species presents significant synthetic challenges and limits the range of potential catalysts that are readily accessible for a systematic evaluation of structure–activity relationships [21-24]. This provides impetus for the investigation into alternative catalysts.

An exciting class of boron-based Lewis acids are the borenium ions [25-26]. Borenium ions are three-coordinate boron cations with two sigma-bound substituents and one dative interaction with a ligand in the third coordination site [27-28]. These relatively underexplored Lewis acids have attracted attention for use in metal-free catalysis. Several groups have recently shown that borenium ions possess novel properties as reagents in direct electrophilic aromatic borylations, carboration and haloboration of alkynes, the enantioselective reduction of ketones, and even in catalytic reduction reaction [29-34]. Imidazole based N-heterocyclic carbene (NHC) borane adducts provide a particularly interesting platform for the generation of borenium ions by hydride abstraction [35]. In 2012, an N-heterocyclic

carbene derived borenium ion was reported by Stephan *et al.* which split the H-H bond in the presence of imines at a very high pressure of H_2 [36]. After that another few groups reported the catalytic hydrogenation of imines and N-heterocycles by NHC based borenium ions [37-42]. Recently Mondal and coworkers synthesized abnormal N-heterocyclic carbene (aNHC) [43-45] and benzimidazolylidene [46-48] stabilized borenium ions and explored their catalytic reactivity towards selective hydrogenation of N-heterocyles (quinolines) to 1,2,3,4-tetrahydroquinoline under ambient conditions (Figure 2.1).

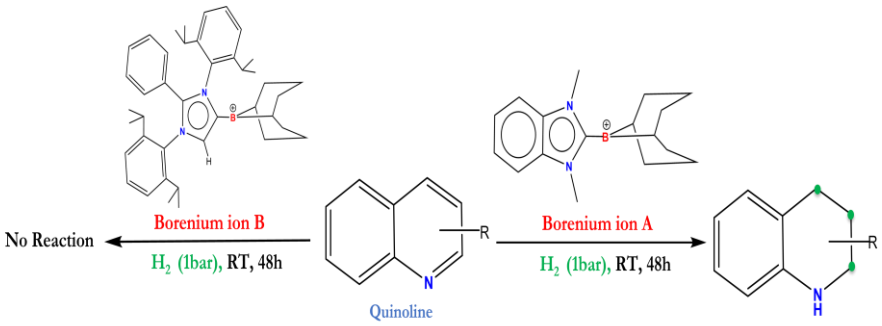

Figure 2.1: Benzimidazolylidene stabilized borenium ion catalysed hydrogenation of N-heterocycles under ambient conditions.

Among natural and synthetic bioactive molecules, 1,2,3,4-tetrahydroquinoline is the most valuable with numerous applications in drugs and agrochemicals [49-50]. Recently, such molecules have also been envisioned as hydrogen reservoirs [51-52]. The catalytic hydrogenation of quinoline derivatives to 1,2,3,4-tetrahydroquinoline is a challenging reaction because of potential catalyst deactivation due to the co-ordination of quinoline reactants and tetrahydroquinoline compounds. In their work Mondal and coworkers observed while the aNHC stabilized borenium ion **B** fails to perform the hydrogenation reaction, the benzimidazolylidene stabilized borenium ion **A** can selectively convert quinolines to 1,2,3,4-tetrahydroquinolines in the presence of molecular hydrogen at room temperature with excellent yields. Furthermore, it can successfully hydrogenate a wide range of substituted quinolines under ambient conditions.

These observations encourage us to understand the behaviour of these newly synthesized borenium ions (**A** and **B**) in detail. However, the previous literature lacks a deep mechanistic understanding of the reactivity of the borenium ions. Therefore, in this chapter, through density functional theory (DFT) computations, a detailed mechanistic investigation is performed which helps to understand the hydrogenation pathway by borenium ions as well as to rationalize the selective behaviour of **A** towards quinoline hydrogenation.

2.2 Computational details

All electronic structure calculations were performed using within density functional theory (DFT) framework. M062X exchange correlation functional along with 6-311g(d,p) basis set have been used for geometry optimization [49,50]. Harmonic vibrational frequency analysis is performed to characterize the optimized structures to be minima (zero imaginary frequency) or transition states (one imaginary frequency). Transition states (TSs) are further verified by intrinsic reaction coordinate (IRC) calculations to confirm their connection to two respective minimum structures. The optimized geometries are further refined with single-point energy calculations at the M062X/6-311++g(d,p) level of theory. All thermochemical data are obtained with the ideal gas-rigid rotor-simple harmonic oscillator approximations at 298.15 K and 1 atm. Zero point-energy corrections are included in the Gibbs free energy values along with a concentration correction for c = 1 mol/ dm^3 condition in the solvent. We have used DCM as a solvent to estimate the relative stabilities of the reaction intermediates/TS involved in the reaction. The SMD solvation model is used to account for the solvent effects [51]. All natural bond orbital (NBO) analyses were performed using the NBO 3.1 package [52]. All calculations were performed using the Gaussian 16 suite of programs [53].

2.3 Results and discussions

Experimentally, the hydrogenation reaction of 2-phenyl quinoline (**1**) was carried out using aNHC based borenium ions **B** in CH_2Cl_2 under 1 atmospheric molecular hydrogen. However, no hydrogenated product was observed. Nevertheless, the hydrogenated product, 2-phenyl-1,2,3,4-tetrahydroquinoline (**16**) was obtained in 63% isolated yield when borenium ion **A** was reacted with substrate under 1 atmospheric H_2 pressure within 24 hours at room temperature in CH_2Cl_2. This sharp contrast in reactivity of **A** with **B** towards hydrogenation reaction prompted us to explore the underlying reason(s). For this, we have considered catalyst **A** with **B** for further computational studies.

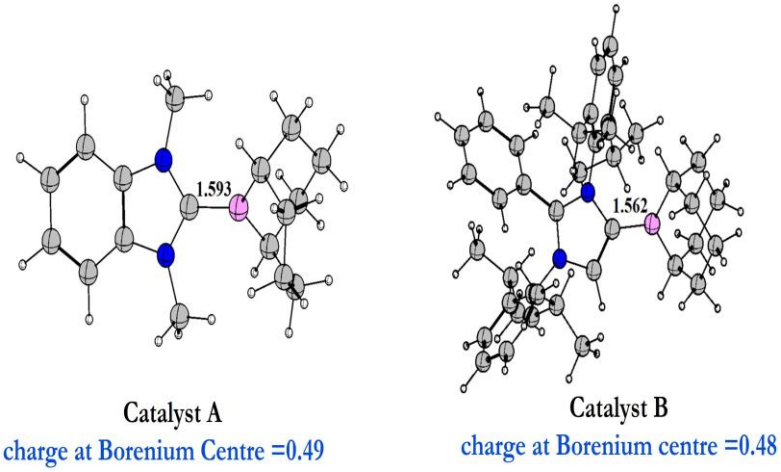

Figure 2.2: Geometry optimized structures of Benzimidazolylidene stabilized borenium ion (**Catalysts A**) and aNHC stabilized borenium ion (**Catalyst B**)

The optimized geometries of **A** and **B** as shown in Figure 2.2, depicts that catalyst **A** has a longer C_{NHC}-B bond length of 1.593 Å compared to **B**, where the C_{NHC}-B distance is 1.562 Å. Natural bonding analysis (NBO) performed on the optimized geometries reveals higher positive charges on the boron centre for **A** (Mulliken charge 0.49) compared to **B** (Mulliken charge 0.48). This behaviour can be rationalized by the higher nucleophilicity of aNHC which quenches the Lewis

acidic character of the boron centre in **B**. On the other hand, the borenium ion **A** exhibits higher Lewis acidity due to the weaker donor property of benzimidazolylidene carbene. This observation is further supported by the significant downfield shift in the experimentally obtained 11B NMR of **A** compared to **B**.

Therefore from these initial observations, we thought that the hydrogenation reaction might be susceptible to the electronic (Lewis acidity) factor of the borenium centres. However, apart from the enhanced Lewis acidity anticipated for **A**, it is important to note the steric protection of the acidic centre in these catalyst systems. It can be assumed that the bulkier catalysts might impede either H_2 activation or hydride delivery in the catalytic cycle. Therefore to gain a detailed insight into the source of catalytic activity differences between **A** and **B**, a mechanistic investigation of the full catalytic cycle is carried out. In this direction, we have studied the hydrogen splitting reaction which is the first step of the catalytic hydrogenation cycle.

2.3.1 Hydrogen activation by borenium ions

The Gibbs free energy profile and the optimized geometries of the intermediates involved in the hydrogen activation step by **A** are depicted in Figure 2.3. Our computed results show that the borenium ion **A** at first interacts with the substrate quinoline (**1**) and forms an FLP type complex **2A** where the B-N distance is 3.704 Å. Note that Gibbs free energy change associated with the formation of compound **2A** is only 2.7 kcal/mol (Figure 2.3). Interestingly, this FLP type complex **2A** is also observed experimentally upon stoichiometric mixing (1:2) of the borenium ion **A** and **1**, as confirmed by 11B NMR spectroscopy. Next, **2A** interacts with H_2 in a side-on manner and forms a reactant complex **3A**. **3A** eventually passes through a concerted transition state (TS) $\mathbf{TS_{3A/4A}}$ and forms an intermediate **4A**. This step has an activation barrier of 20.0 kcal/mol. At $\mathbf{TS_{3A/4A}}$ the H-H

bond length elongates to 0.847 Å. The B-H and N-H distances are 1.396 Å and 1.578 Å, respectively. NBO analysis of the H_2 activation TSs reveal a cooperative interaction between the donor and acceptor centers.

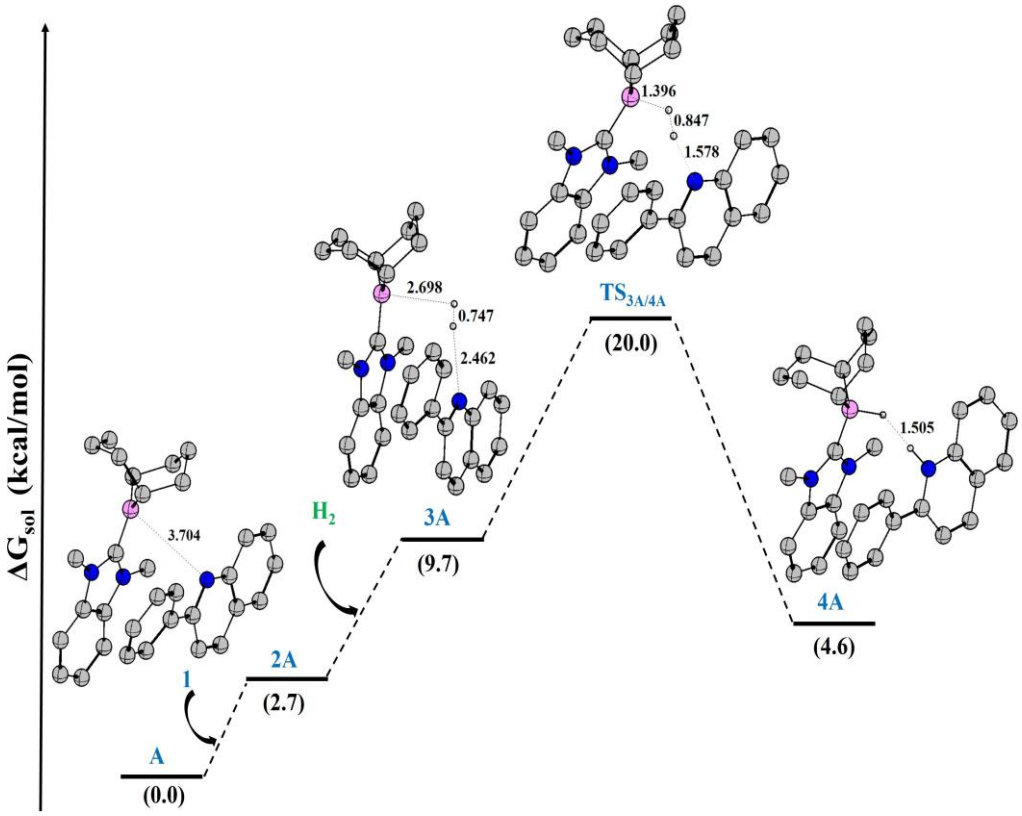

Figure 2.3: The solvent corrected Gibbs free energy profile for the hydrogen activation by the FLP formed by **1** and **A**. All energies are reported in kcal/mol. All distances are shown in Å.

Note that, due to the highly steric crowding, it is difficult for **B** to form such a complex with **1**. This is reflected by the longer B-N distance (3.776 Å) in complex **2B** and a high positive free energy change (6.8 kcal/mol, Figure 2.4) associated with this process. Note that The 11B NMR spectrum of the reaction mixture of the borenium ion **B** and **1** showed a broad resonance at 58.5 ppm which is the characteristic peak of borenium ion **B**. This further validates our computed result that the formation of complex **2B** does not take place in the reaction mixture. Moreover, for **B**, this transition state for H_2 activation lies quite high in the free

energy profile (34.7 kcal/mol). Hence we can conclude that apart from the strong electron-donating ability of aNHC ligand which reduces the Lewis acidity of the borenium ion, the steric crowding around the active centre results in the inactivity of **B** towards hydrogenation reaction.

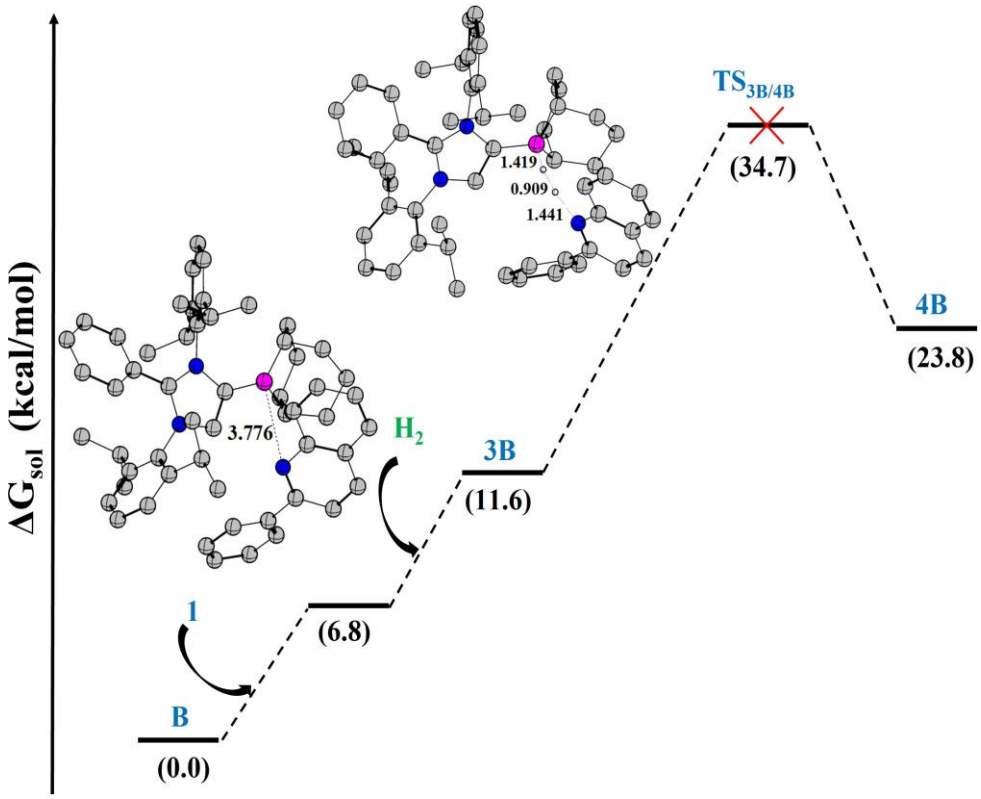

Figure 2.4: The solvent corrected Gibbs free energy profile for the hydrogen activation by the FLP formed by **1** and **B**. All energies are reported in kcal/mol. All distances are shown in Å.

2.3.2 The second hydrogenation step: 1,4 addition

On the splitting of the H-H bond, next the intermediate **4A** undergoes an intermolecular rearrangement to form another isomer **5A** where the B-H bond is oriented towards the C4 atom of **1** (Figure 2.5). In the next step, the hydride ion migrates from the boron centre to the C4 centre of **1** via the transition state $\mathbf{TS_{5A/6A}}$. The optimized geometries of the intermediates involved in the first hy-

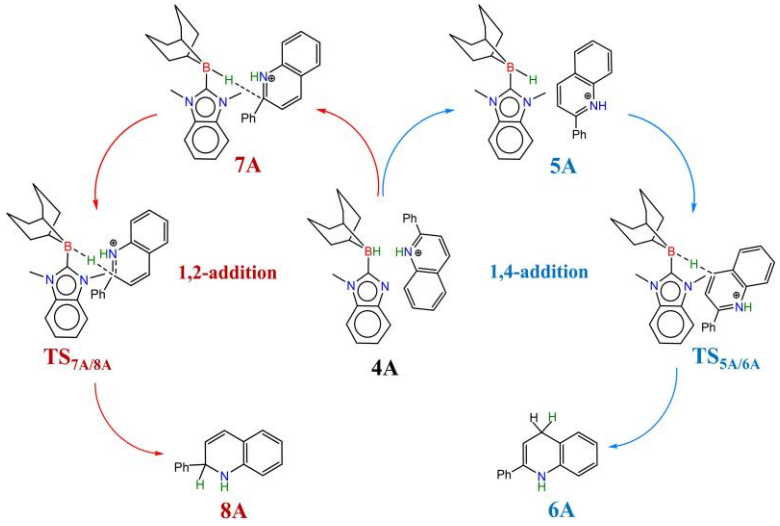

Figure 2.5: Possible reaction routes for the second hydrogenation step of quinoline.

drogenation cycle are depicted in Figure 2.7. In addition to that, we are able to locate another possible isomer of **4A** where the B-H bond is positioned towards C2 atom of **1**. This isomer numbered as **7A** can also transfer the hydride atom to **1** resulting in **8A** through the transition state $\mathbf{TS_{7A/8A}}$ (Figure 2.5). However, as shown in Figure 2.6, $\mathbf{TS_{5A/6A}}$ has a lower activation energy barrier (19.0 kcal/mol) compared to $\mathbf{TS_{7A/8A}}$ (23.2 kcal/mol). As a result, the formation of 2-phenyl-1,4-dihydro-quinoline **9A** is favoured.

2.3.3 The third hydrogenation step: C2=C3 hydrogenation

The next step is to hydrogenate the C2=C3 double bond of **9A** which further requires a proton and hydride migration. At first, the proton affinity of **9A** is calculated (272.6 kcal/mol) which is slightly higher than that of **1** (270.0 kcal/mol). This leads us to explore the possibility of hydrogen activation by **9A** and **A**. However, calculated results show that the barrier of H_2 activation $\mathbf{TS_{10A/11A}}$

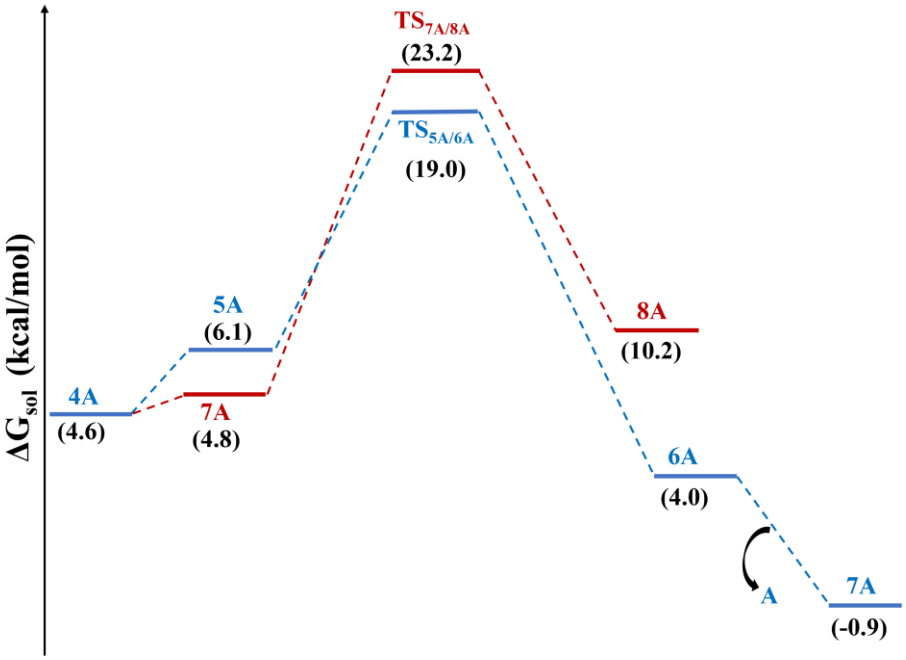

Figure 2.6: The solvent corrected Gibbs free energy profile for the second hydrogenation step of quinoline.

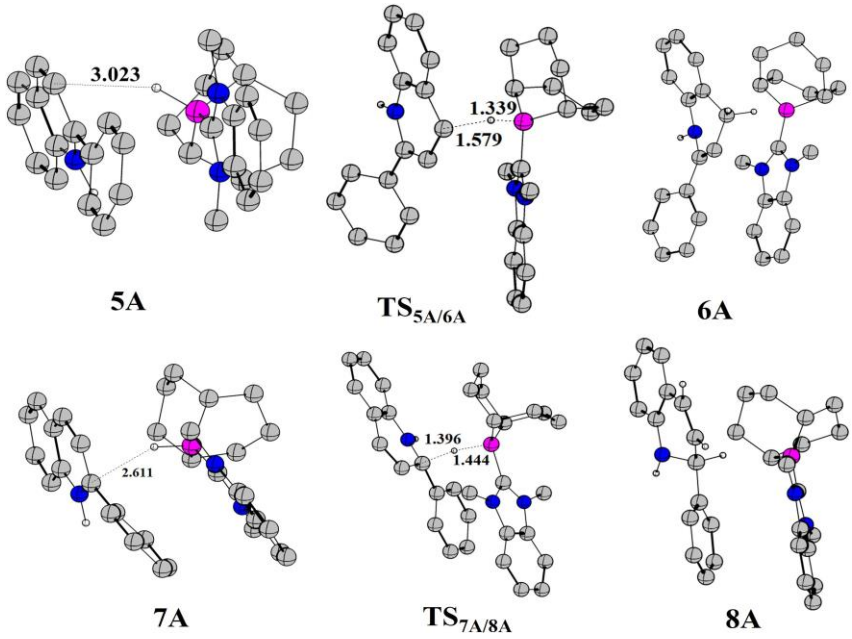

Figure 2.7: Geometry optimized structures of the intermediates/transition states involved in the second hydrogenation step (up, 1,4 addition) and (down 1,2 addition) of the catalytic cycle.

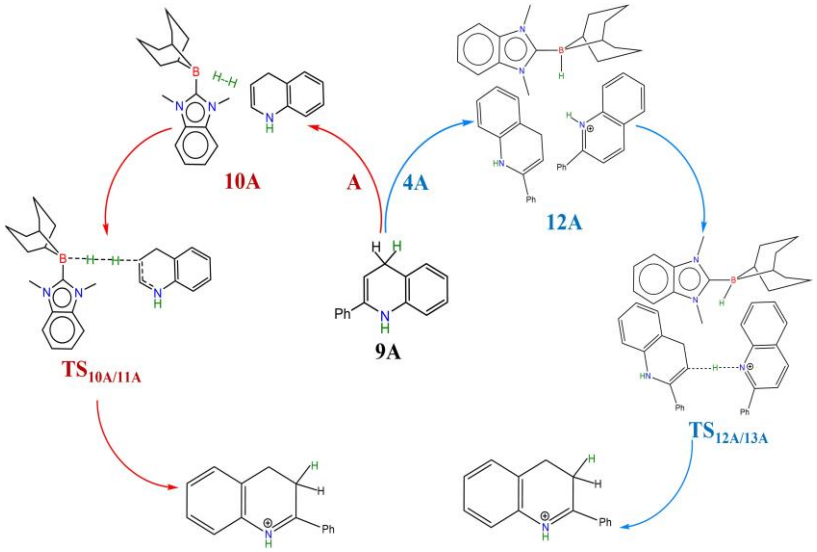

Figure 2.8: Possible reaction routes for the third hydrogenation step of quinoline.

by the FLP formed by **9A** and **A** is quite high (49.8 kcal/mol) which ruled out this pathway (Figure 2.9). Rather we find that the intermediate **9A** approaches the hydrogen split intermediate **4A** and forms a complex **12A** which is stabilized by the N-H···C hydrogen bonding interaction between **9A** and quinoline ion (Figure 2.8). In the subsequent step, this hydrogen-bonded proton is transferred to the C3 centre of **9A** via the transition state $\mathbf{TS_{12A/13A}}$ with an activation barrier of 18.2 kcal/mol. After that, once the loosely bound quinoline **1** is released, a complex **14A** is formed. This leads to the transfer of hydride from boron to the C2 centre of quinoline moiety. This process is associated with a free energy barrier ($\mathbf{TS_{14A/15A}}$) of only 10.2 kcal/mol (see Figure 2.9). It is interesting to mention that for this hydride transfer process, we have studied the possibility of competing behaviour of **A**. But the computed hydride affinity of **A** (44.7 kcal/mol) is lower than $\mathbf{9AH^+}$ (60.8 kcal/mol). Therefore it can be said that the weak acidity of catalyst **A** plays an important role in driving the catalytic hydrogenation cycle. Finally, the intermediate **15A** dissociates to deliver 2-phenyl-1,4,5,6-tetrahydroquinoline **16** as the final product.

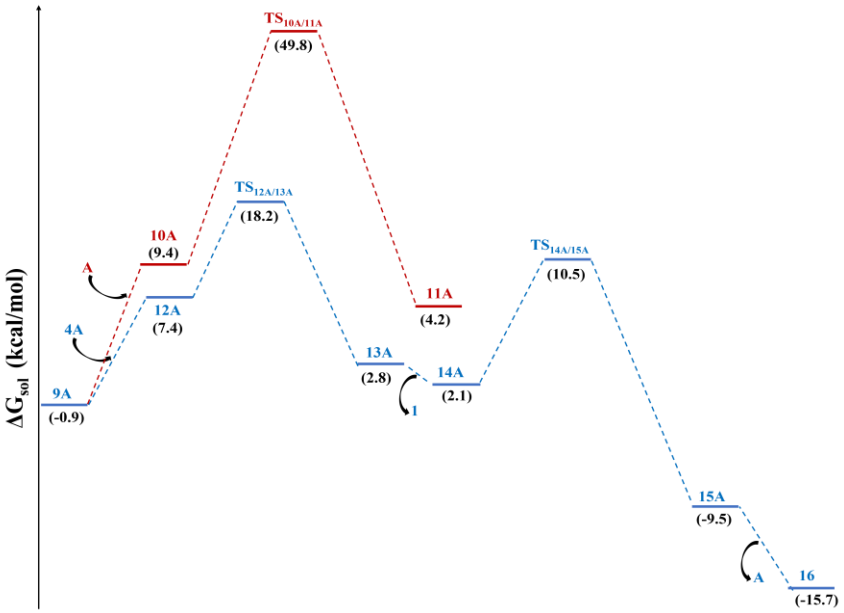

Figure 2.9: The solvent corrected Gibbs free energy profile for the second hydrogenation step of quinoline.

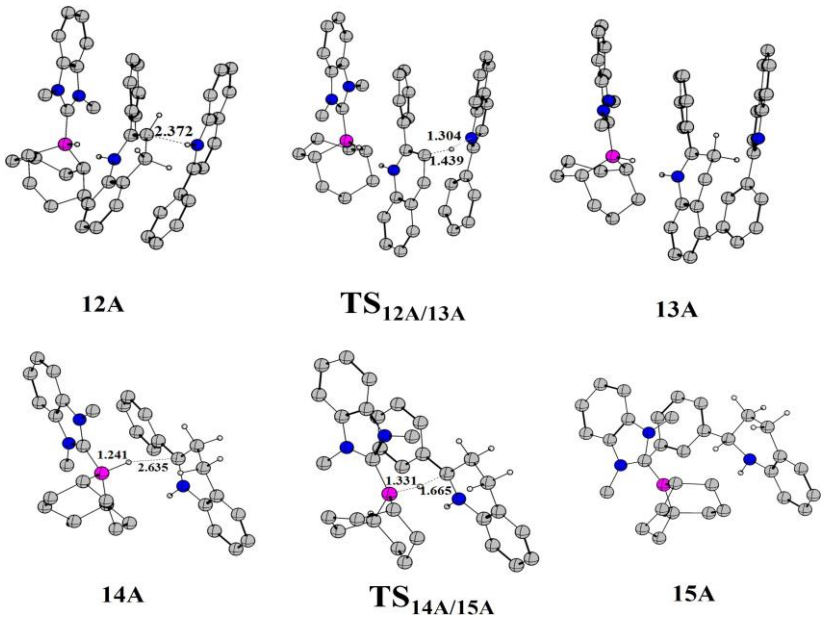

Figure 2.10: Geometry optimized structures of the intermediates/transition states involved in the third hydrogenation step.

2.4 Conclusion

In conclusion, our results suggest that the hydrogenation of quinoline by the borenium ion proceeds in a stepwise manner. At the beginning of the catalytic cycle the borenium ion **A**, in combination with quinoline base performs an FLP like H_2 cleavage and forms a quinolinium hydridoborate ion pair which acts as the key intermediate in the catalytic hydrogenation cycle. The next step is the 1,4-hydrogenation followed by the proton transfer and the hydride transfer to complete the C2=C3 double bond hydrogenation. In addition we have also found that the steric hindrance at the active centre of the aNHC stabelized borenium ion creates a deleterious effect on its catalytic reactivity.

2.5 References

[1] Blaser, H.-U.; Spindler, F.; Thommen, M. Wiley-VCH Verlag GmbH, 2008, pp. 1279–1324.

[2] Blaser, H. U. Top. Catal. 2010, 53, 9971001..

[3] Shimizu, H.; Nagasaki, I.; Matsumura, K.; Sayo, N.; Sai-to, T. Acc. Chem. Res. 2007, 40, 1385–1393.

[4] De Vries, J. G.; Elsevier, C. J. Wiley-VCH, Weinheim, 2007.

[5] Bullock, R. M. Wiley-VCH Verlag GmbH Co, 2010.

[6] Bullock, R. M. Science, 2013, 342, 1054-1055.

[7] Giustra, Z. X.; Ishibashi, J. S. A.; Liu, S.-Y. Coord. Chem. Rev. 2016, 314, 134181.

[8] Filonenko, G. A.; van Putten, R.; Hensen, E. J. M.; Pidko, E. A. Chem. Soc. Rev. 2018, 47, 14591483.

[9] Agbossou-Niedercorn, F.; Michon, C. Coord. Chem. Rev. 2020, 425, 213523..

[10] Wen, J.; Wang, F.; Zhang, X. Chem. Soc. Rev. 2021, 50, 32113237.

[11] Stephan, D. W. Science, 2016, 354, 1248–1256.

[12] Lam, J.; Szkop, K. M.; Mosaferi, E.; Stephan, D. W. FLP catalysis: Chem. Soc. Rev. 2019, 48, 35923612.

[13] Stephan, D. W.; Erker, G. Frustrated Lewis Pair Chemis-try: Development and Perspectives. Angew. Chem., Int. Ed. 2015, 54, 64006441.

[14] Stephan, D. W. Frustrated Lewis Pairs. J. Am. Chem. Soc., 2015, 137, 10018–10032.

[15] Stephan, D. W. Acc. Chem. Res., 2015, 48, 306–316.

[16] Scott, D. J.; Fuchter, M. J.; Ashley, A. E. Chem. Soc. Rev. 2017, 46, 56895700.

[17] Welch, G. C.; Juan, R. R. S.; Masuda, J. D.; Stephan, D. W. Science, 2006, 314, 1124-1126.

[18] Gazis, T. A.; Willcox , D.; Melen, R. L. Springer International Publishing, Cham, 2021, pp. 209–235..

[19] Chase, P. A.; Jurca, T.; Stephan, D. W. Chem. Commun. 2008, 17011703.

[20] Jeffrey, M. ; Hatnean, J. A. Stephan, D. W. J. Am. Chem. Soc. 2012, 134, 15728 15731.

[21] Nicasio, J. A.; Steinberg, S.; Ines, B.; Alcarazo, M. Chem. -Eur. J. 2013, 19, 1101611020..

[22] Liu, Y.; Du, H. J. Am. Chem. Soc. 2013, 135, 6810-6813.

[23] Mewald, M.; Fro hlich, R.; Oestreich, M .Chem. - Eur. J. 2011, 17, 94069414..

[24] Liu, Y.; Du, H. J. Am. Chem. Soc. 2013, 135, 12968-12971.

[25] Kolle, P.; Noth, H. Chem. Rev. 1985, 85, 399-41..

[26] De Vries, T. S.; Prokofjevs, A.; Vedejs, E. Chem. Rev. 2012, 112, 4246 4282.

[27] Piers, W. E.; Bourke, S. C.; Conroy, K. D. Angew. Chem., Int. Ed. 2005, 44, 50165036.

[28] Eisenberger, P.; Crudden, C. M. Dalton Trans. 2017, 46, 48744887.

[29] Bagutski, V.; Del Grosso, A.; Ayuso Carrillo, J.; Cade, I. A.; Helm, M. D.;

Lawson, J. R.; Singleton, P. J.; Solo-mon, S. A.; Marcelli, T.; Ingleson J. Am. Chem. Soc. 2013, 135, 474-487.

[30] Del Grosso, A.; Singleton, P. J.; Muryn, C. A.; Ingleson, M. J. Angew. Chem., Int. Ed. 2011, 50, 21022106.

[31] Lawson, J. R.; Clark, E. R.; Cade, I. A.; Solomon, S. A.; Ingleson, M. J. Angew. Chem., Int. Ed. 2013, 52, 75187522.

[32] Stahl, T.; Muether, K.; Ohki, Y.; Tatsumi, K.; Oestreich, M. J. Am. Chem. Soc. 2013, 135, 10978-10981.

[33] Eisenberger, P.; Bailey, A. M.; Crudden, C. M. J. Am. Chem. Soc. 2012, 134, 17384-17387.

[34] Lindsay, D. M.; McArthur, D. Chem. Commun. 2010, 46, 2474-2476.

[35] McArthur, D.; Butts, C. P.; Lindsay, D. M. Chem. Commun. 2011, 47, 6650-6652.

[36] Farrell, J. M.; Hatnean, J. A.; Stephan, D. W. J. Am. Chem. Soc. 2012, 134, 1572815731.

[37] Eisenberger, P.; Bestvater, B. P.; Keske, E. C.; Crudden, C. M. Angew. Chem., Int. Ed. 2015, 54, 24672471.

[38] Farrell, J. M.; Posaratnanathan, R. T.; Stephan, D. W. Chem. Sci. 2015, 6, 2010 2015.

[39] Huchenski, B. S. N.; Adams, M. R.; McDonald, R.; Fer-guson, M. J.; Speed, A. W. H. Organometallics 2016, 35, 3101-3104.

[40] Mercea, D. M.; Howlett, M. G.; Piascik, A. D.; Scott, D.J.; Steven, A.; Ashley, A. E.; Fuchter, M. J. Chem. Commun. 2019, 55, 70777080.

[41] Lam, J.; Gunther, B. A. R.; Farrell, J. M.; Eisenberger, P.; Bestvater, B. P.; Newman, P. D.; Melen, R. L.; Crudden, C. M.; Stephan, D. W. Dalton Trans. 2016, 45, 1530315316..

[42] Clarke, J. J.; Maekawa, Y.; Nambo, M.; Crudden, C. M. Organic Letters, 2021, 23, 6617-6621.

[43] Perez, E. A.; Rosenthal, A. J.; Donnadieu, B.; Parameswaran, P.; Frenking, G.; Bertrand, G. Science, 2009, 326, 18124–18137.

[44] Sau, S. C.; Hota, P. K.; Mandal, S. K.; Soleilhavoup, M.; Bertrand, G. Chem. Soc. Rev. 2020, 49, 12331252.

[45] Ung, G.; Bertrand, G. Chem.- Eur. J. 2011, 17, 8269-8272.

[46] Hahn, F. E.; Wittenbecher, L.; Boese, R.; Blaser, D. Chem.- Eur. J. 1999, 5, 19311935.

[47] Herrmann, W. A. Angew. Chem., Int. Ed. 2002, 41, 1290 1309.

[48] Bourissou, D.; Guerret, O.; Gabbai, F.; Bertrand, G. Sta-ble carbenes. Chem. Rev. 2000, 100, 3991.

[49] Sridharan, V.; Suryavanshi, P. A.; Menendez, J. C. Chem. Rev. 2011, 111, 7157 7259.

[50] Muthukrishnan, I.; Sridharan, V.; Menendez, J. C. Chem. Rev. 2019, 119, 50575191.

[51] Deraedt, C.; Ye, R.; Ralston, W. T.; Toste, F. D.; Somor-jai, G. A. J. Am. Chem. Soc. 2017, 139, 1808418092.

[52] Teichmann, D.; Arlt, W.; Wasserscheid, P.; Freymann, R. Energy Environ. Sci. 2011, 4, 27672773.

3

Investigating Tetrel based Neutral Frustrated Lewis Pairs for Hydrogen Activation

Work reported in this chapter is based on: Pallavi Sarkar, Shubhajit Das, Swapan K Pati, Inorganic Chemistry, 2021, 60, 20. 15180-15189. Reproduced with permission from American Chemical Society.

3.1 Introduction

The activation of the apolar H-H bond of hydrogen molecule (H_2) is challenging as well as the key step in any direct catalytic hydrogenation [1-5]. In this regard, the frustrated Lewis pair (FLP) chemistry has played a pivotal role in the development of transition metal (TM)-free routes to catalytic hydrogenations [6-11]. A wide range of LA/LB combinations has been exploited for H_2 activation in FLP literature. Compared to the diverse spectrum of the employed LB components, the range of LA has been quite confined. In fact, during the early stages of FLP chemistry, perfluorinated boranes were mainly used despite their drawbacks, such as moisture sensitivity and low functional group tolerance [12-15]. Nevertheless, these limitations of boranes drove a significant amount of research for exploring new LAs [16,17] and eventually group 14 tetrylium cations and phosphonium LAs were introduced in FLP chemistry [18,19].

Very recently, neutral tetrel LAs were introduced in FLP chemistry. Mitzel *et al.* reported a series of intramolecular geminal FLPs featuring neutral tetrel (E) atoms in combination with P donors $(C_2F_5)_3E\text{-}CH_2\text{-}P(tBu)_2$ (E = Si,Ge,Sn) [20-23]. They were utilized for activation of a range of small molecules like, CO_2, SO_2, including H_2. These findings indicate these geminal FLPs hold great potential for being prospective hydrogenation catalysts. Presumbly one advantage of these FLP combinations is their neutral form compared to the corresponding cationic group 14 FLPs which are accompanied by a counter anion for charge neutrality additionally complicating the reaction mechanism. Nevertheless, despite considerable experimental works, one point that remains to be fully understood is how these neutral E LA atoms participate in cooperative H_2 activation. According to the cooperative mechanistic model typically, the empty p_z orbital on the LA acts as the acceptor orbital to receive electrons from $\sigma(H_2)$ orbital [24-30]. But these tetra-coordinated E atoms have no formally empty p orbital to engage into electron

transfer with the H_2 molecule. Therefore in this current chapter, we attempt to answer this question through a detailed computational mechanistic investigation of the H_2 activation by a series of intramolecular FLPs bearing neutral E atoms.

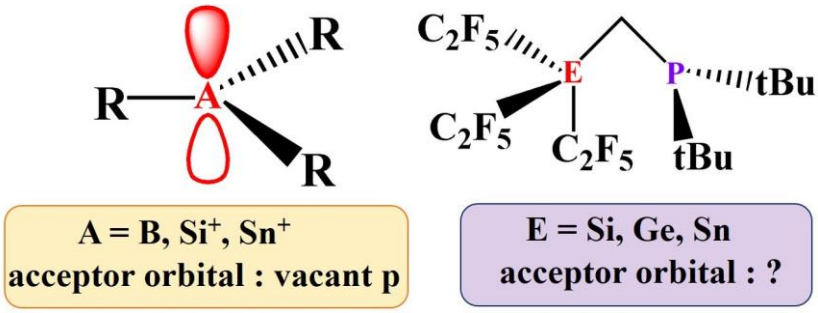

Figure 3.1: Group 13 and 14 LAs used in FLP chemistry (left), Intramolecular FLPs featuring neutral tetrel atom.

3.2 Computational details

All electronic structure calculations are performed using M062X [31,32] functional within density functional theory (DFT). In order to account for the non-covalent interactions, Grimme's D3 dispersion model is employed [34]. For lighter at-oms (C, H, N, P, O, F) we have used 6-311g(d,p) basis set while for the Si, Ge and Sn def2TZVP along with Stuttgart-Dresden effective core potential is employed [35]. This basis set combination (6-311G(d,p) for C, H, F, P, N + def2TZVP with SDD ECP for Si, Ge, Sn) is hereafter denoted as BS1. Harmonic vibrational frequency analysis is performed to characterize the structures to be minima (zero imaginary frequency) or transition states (one imaginary frequency). Transition states (TSs) are further verified by intrinsic reaction coordinate (IRC) calculations to con-firm their connection to two respective minimum structures. Based on M062X-D3/BS1 optimized geometries, the electronic energies are further refined with single-point energy calculations at the M062X-D3/BS2 level of theory (BS2: 6-311++G(d,p) for C, H, F, P, N + def2TZVP with SDD ECP for Si, Ge, Sn). All

thermochemical data are obtained with the ideal gas-rigid rotor-simple harmonic oscillator approximations at 298.15 K and 1 atm. Zero point-energy corrections are included in the Gibbs free energy values along with a concentration correction for c = 1 mol/dm^3 condition in the solvent. We have used THF as a solvent to estimate the relative stabilities of the reaction intermediates/TS involved in the reaction. The SMD solvation model is used to account for the solvent effects [36]. All natural bond orbital (NBO) analyses are performed using the NBO 3.1 package [37]. All calculations are performed using the Gaussian 16 suite of programs [38]. In this chapter we have used the following colour code C (grey), H (white), Si (purple), Ge (pale blue), Sn (green), O (red), N (blue), P (yellow) and F (fluorescent green).

3.2.1 Activation strain analysis

Activation-strain analysis is performed to analyze H_2 activation profiles by considering a bimolecular reaction between FLP and H_2 [39-41]. According to this model, potential energy surface ΔE is decomposed into two main contributions, the strain energy ΔE_{strain} which is the distortion energy experienced by the deformed reactants during the transformation and the interaction energy ΔE_{int}.

$\Delta E(r) = \Delta E_{strain}(r) + \Delta E_{int}(r)$

$\Delta E_{strain} = \Delta E_{strain}(FLP) + \Delta E_{strain}(H_2)$.

Here the reaction coordinate (r) is defined as the projection of the IRC onto the H-H distance which undergoes a well-defined change during the course of the reaction from the initial reaction complexes to the corresponding transition states.

3.2.2 Energy decomposition analysis

The interaction energy ΔE_{int} can be further divided into four components with the aid of energy decomposition analysis (EDA) [42-47].

$\Delta E_{int}(r) = \Delta V_{elstat}(r) + \Delta E_{Pauli}(r) + \Delta E_{orb}(r) + \Delta E_{disp}(r)$

The term ΔV_{elstat} accounts for the classical electrostatic interaction between the unperturbed charge distributions of the deformed reactants and is usually attractive. The Pauli repulsion, ΔE_{Pauli} corresponds to the destabilizing interactions between occupied orbitals and is responsible for any steric repulsion. The orbital interaction ΔE_{orb} originates from the mixing of orbitals, the charge transfer and the polarization between the isolated fragments. The last term ΔE_{disp} corresponds to the contribution that arises due to dispersion forces. The EDA analyses are performed on the M062X-D3/BS1 optimized geometries using PBE-D3/TZ2P method as implemented in ADF2017.01 [48]. Herein, PBE-D3/TZ2P level is used due to the nonavailability of M062X-D3 functional in ADF code. Reliability of PBE-D3/TZ2P level of theory in taking care of the weak noncovalent interactions of FLPs has also been shown by Skara *et al.* [49]. Computations were carried out without frozen core approximation using all-electron basis set. Scalar relativistic effects were considered using the zeroth-order regular approximation [50-51].

3.3 Results and discussions

To obtain a clear mechanistic idea and to identify various factors influencing the H_2 activation process, we examined a series of 18 intramolecular FLPs, comprised of Si, Ge, Sn LAs along with N and P donor atoms. In general, these FLPs are denoted as **1** (Figure 3.2) and while discussing specific systems, we have used the notation Y-E-D (Y=intermediate or transition state). Furthermore, different substituents (R=C_2F_5, CF_3, F; R'=tBu, iPr, Me) on the LA and LB sites are used to vary the steric as well as the electronic environment around the active sites. Note that, the majority of the investigated FLPs are already synthesized by the group of Mitzel [52-54]. A few additional combinations were used to complement the pool for a comprehensive under-standing of the H_2 activation step.

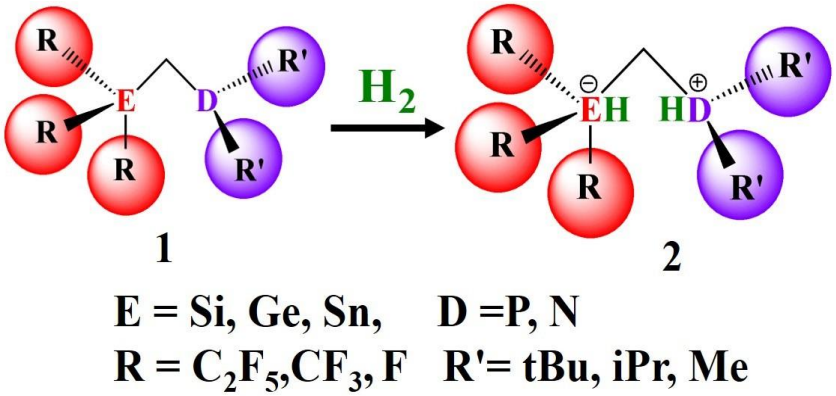

Figure 3.2: General structural framework and the series of the geminal FLP systems considered in this study for H_2 activation. Here E=Tetrel atom and D=Donor atom.

3.3.1 Structural features

We begin by analyzing the optimized geometries of three representatives FLPs, $(C_2F_5)_3$Si-CH_2-P(tBu)$_2$ (hereafter denoted as **1-Si-P**), $(C_2F_5)_3$Ge-CH_2-P(tBu)$_2$ (denoted as **1-Ge-P**) and $(C_2F_5)_3$Sn-CH_2-P(tBu)$_2$ (denoted as **1-Sn-P**). We found that these geminal systems feature a wide ∠(E-CH_2-P) angle. For example, **1-Si-P** and **1-Ge-P** have the ∠(E-CH_2-P) of the value of 119.1° and 117.5° respectively, whereas for **1-Sn-P**, the ∠(Sn-CH_2-P) is of 114.8°. Note that form the solid state structures ∠(E-CH_2-P) angles for **1-Si-P**, **1-Ge-P** and **1-Sn-P** are 120.4°, 117.8° and 113.9° which are in excellent agreement with our computed values. This wide-angle prevents any direct interaction between the E and the P sites which is reflected by a large separation of around 3.0 Å between the acidic and basic sites in these molecules (Figure 3.3). In contrast, the corresponding boron analogue $(C_2F_5)_2$B-CH_2-P(tBu)$_2$, is known to exist in the "quenched ring-closed form" compared to the ring-opened isomer [55]. These observations suggested that these geminal systems possess a significant FLP-type behaviour and therefore the unquenched reactivity at the acidic and basic sites of these systems can be utilized for the heterolytic splitting of the hydrogen molecule.

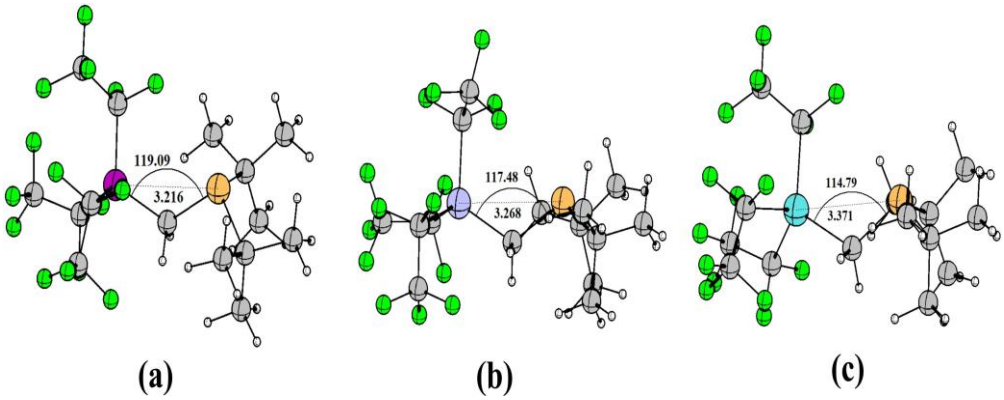

Figure 3.3: Optimized geometries of (a) $(C_2F_5)_3Si\text{-}CH_2\text{-}P(tBu)_2$ (b) $(C_2F_5)_3Ge\text{-}CH_2\text{-}P(tBu)_2$ and (c) $(C_2F_5)_3Sn\text{-}CH_2\text{-}P(tBu)_2$. Colour code C (grey), H(white), P (yellow), F (light green), Si (magenta), Ge (pale blue), Sn (green).

3.3.2 H_2 activation

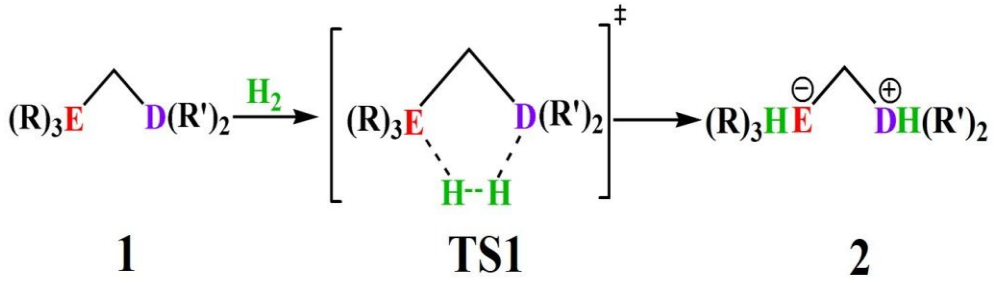

Figure 3.4: Schematic representation of H_2 activation reaction by **1**.

Figure 3.4 depicts the mechanism of H_2 activation by **1**. Initially, **1** forms a reactant complex **1-RC**, which results from a side-on interaction between H_2 and the E atom (Figure 3.5). **1-RC** passes through a single concerted five-membered transition state, **TS1**. At **TS1**, the H-H bond elongates from its equilibrium value (0.74 Å) which indicates the weakening of the H-H bond and eventually it leads to a heterolytic cleavage of the H_2 molecule. As a result, the hydride shifts to the E site while the proton attaches to the D atom, leading to the formation of the zwitterionic product **2**.

3.3.3 Mechanism of H_2 activation

Given the apparent resemblance of the optimized geometries of the stationary points, we expect no major deviation in the mechanistic pathway of H_2 activation for the FLPs that we have considered. Next, we turned our attention to establish a clear mechanistic picture of the H_2 activation pathway by **1**. We already mentioned that the two electron transfer events leading to the heterolytic splitting of the H-H bond by a typical FLP involve (1) Electron transfer from the σ bonding orbital of the H_2 to the empty orbital (typically LUMO) of the acceptor atom, and

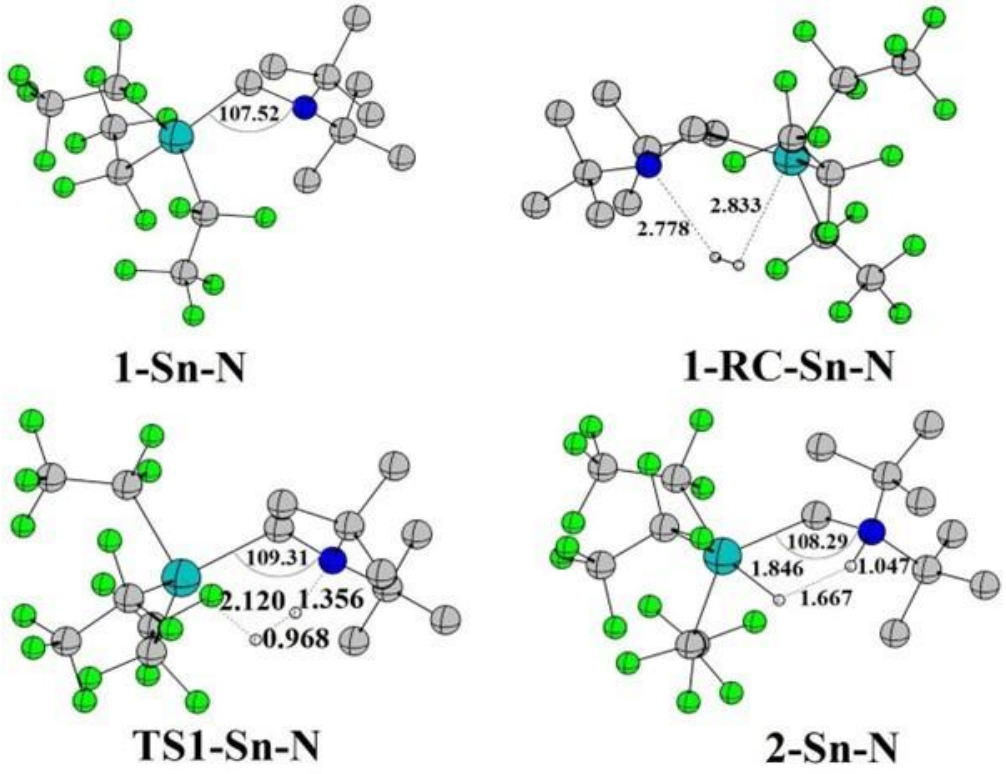

Figure 3.5: Geometry optimized structures of the intermediates/TSs involved in H_2 activation process by **1-Sn-N**. All distances are shown in Å. The hydrogen atoms are omitted for clarity.

(2) simultaneous electron transfer from a filled donor orbital to the σ^* anti-bonding orbital of the H-H bond. While we envisage that on the donor site this picture remains the same for **1**, on the acid site there ought to be a different

mechanistic rationale since there exist no formally empty orbitals.

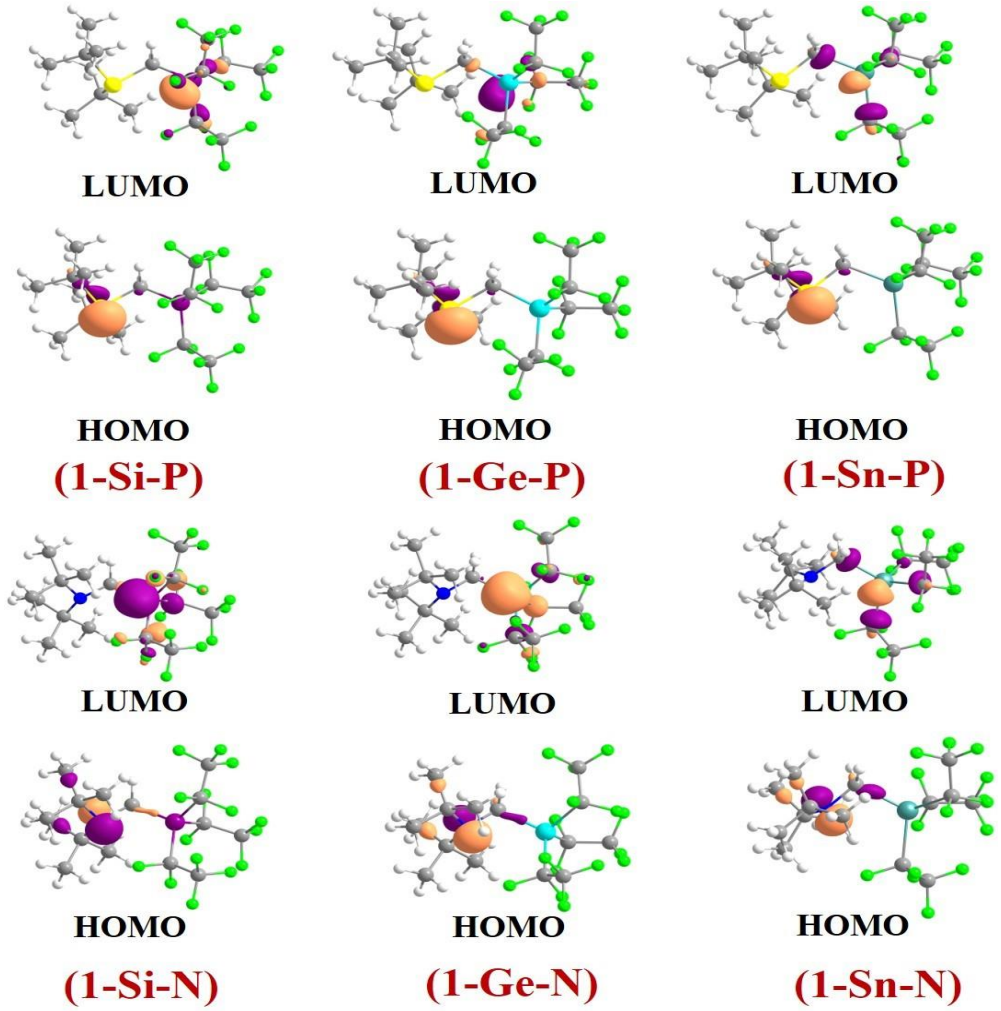

Figure 3.6: Frontier molecular orbitals of **1**s.

To find potential acceptor orbital(s), we first examined the FMOs of 1 (Figure 3.6). While the HOMO is located over the donor atom (N or P), the LUMO is found to be distributed over the E atom as well as over the E-CH_2 and E-R bonds. NBO analysis identifies the nature of these two orbitals as σ^*(E-CH_2) orbital and σ^*(E-R) orbital. The major difference upon varying the E atom is the composition of the LUMO, which changes from mainly σ^*(E-R) orbital for Si to more or less an equal distribution of both the orbitals for Sn. NBO analysis of **TS1** clearly

demonstrates the involvement of these two orbitals in the H_2 cleavage step. In their study of a similar molecule $(C_2F_5)_3SiON(Me)_2$, Mitzel and group have also found the presence of an electron donation from the nitrogen lone pair to the antibonding orbital of Si-C(C_2F_5) bond [56]. Similarly we also find substantial interaction between σ(H-H) orbital and σ^*(Si-R) and σ^*(Si-CH_2) orbitals (estimated $\Delta E^{(2)}$ =26.9 and 19.8 kcal/mol respectively) in the structure of **TS1-Si-N**. For **TS1-Si-P**, these interactions are already at a very advanced stage and we find that σ orbital of the newly formed Si-H bond is engaged in interaction with σ^*(Si-R) and σ^*(Si-CH_2) orbitals. This is presumably due to the different positions of those two TS structures on the potential enery surface as evident from their H-H distances (0.922 Å vs 1.046 Å for **1-Si-N** and **1-Si-P**, respectively). Thus, to have a fair comparison, we performed NBO analysis throughout the entire reaction pathway. Our results reveal that due to the preorganized nature of the intramolecular FLP **1**, from an early stage of the reaction the lone pair (LP) of D begins electron donation to σ^*(H-H) orbital along with concomitant electron transfer to σ^*(E-CH_2) and σ^*(E-R) orbitals from σH_2 orbital (Figure 3.7 and Figure 3.8). These two synergistic interactions develop further with the advancement of the reaction resulting in the progressive weakening of the H-H bond which ultimately leads to the formation of the product **2**. To understand the role of the four σ^* orbitals as the acceptor orbital further, the estimated D-A interaction energies are plotted as a function of the H-H stretch (Figure 3.9). While for **1-Si-P**, one of the σ^*(E-R) orbital acts as the predominant acceptor orbital (blue line), contributions from σ^*(E-CH_2) orbital (red line) becomes more and more significant upon changing the identity of the E by moving down the group. In fact, σ^*(E-CH_2) orbital is the predominant acceptor orbital in the case of **1-Sn-P**. The increasing influence of σ^*(E-CH_2) orbital can be correlated with the increasing Lewis acidity of E atoms in **1** along with the group.

It is interesting to note that phosphonium cations, where the Lewis acidity

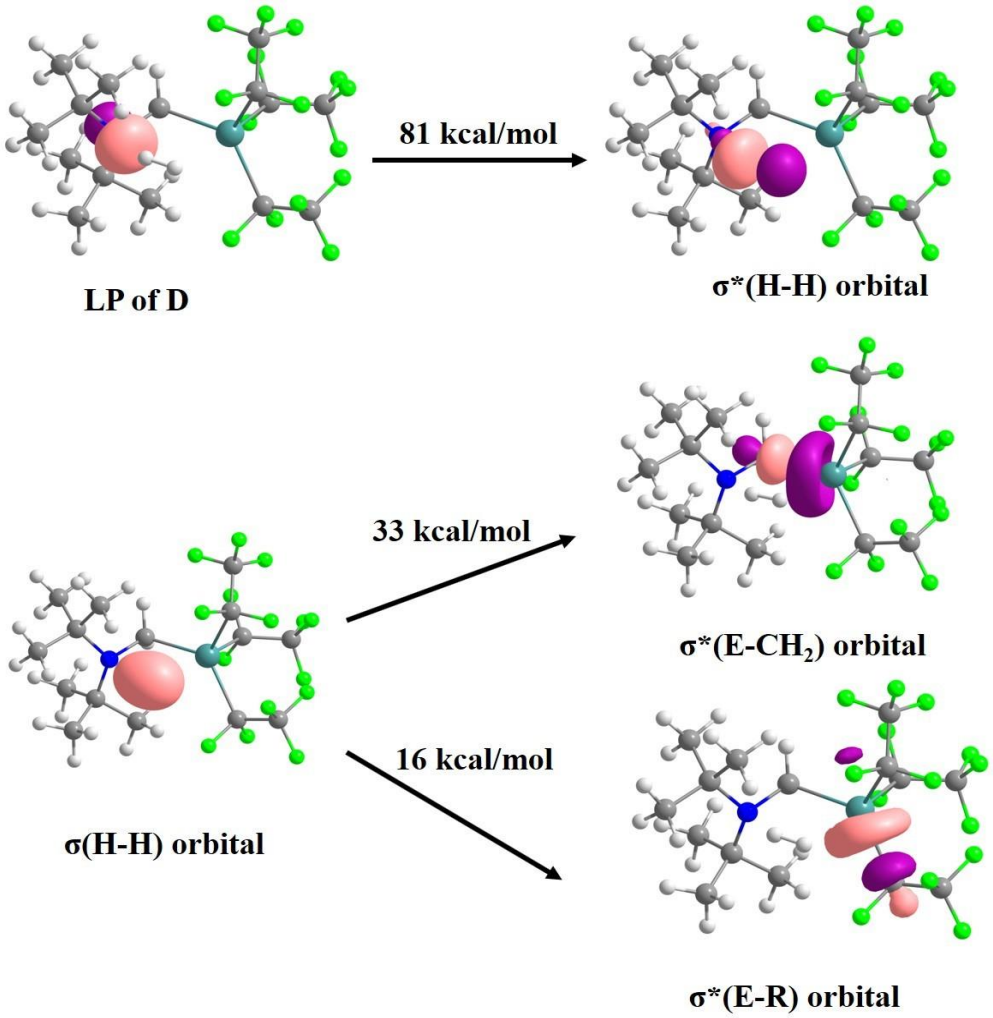

Figure 3.7: NBOs for **TS1** of **1-Sn-N** highlighting the major interactions .

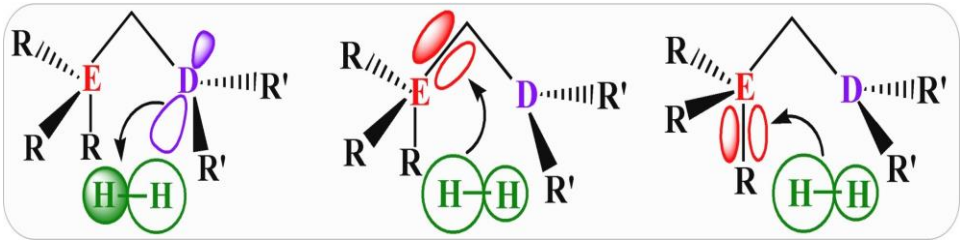

Figure 3.8: Schematic representation of the mechanism of H_2 activation by **1**.

of the pentacoordinate phosphorus atom resides in the σ^* orbital of its adjacent bond [57, 58]. We observed a similar effect by swapping the D site from P to N

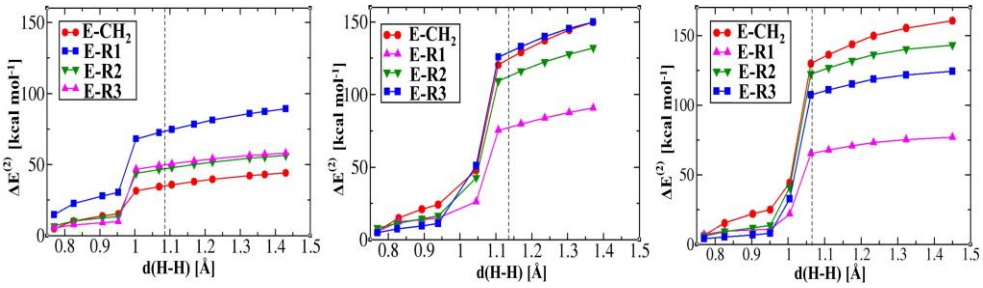

Figure 3.9: Donor-acceptor interaction energies estimated at the second-order perturbation theory level associated with interaction $\sigma H_2 \rightarrow \sigma^*(E\text{-}CH_2)/\sigma^*(E\text{-}R)$ along the minimum energy path for (a) **1-Si-P** (b) **1-Ge-P** and (c) **1-Sn-P**. The dotted lines denote the respective TSs.

as depicted in Figure 3.10. Due to the higher electronegativity of nitrogen, the bridgehead carbon acquires a more positive charge which instigates the $\sigma^*(E\text{-}CH_2)$ orbital a better acceptor orbital compared to when the donor centre is P. Overall, our findings reveal that the $\sigma^*(E\text{-}CH_2)$ and $\sigma^*(E\text{-}R)$ orbitals play a very crucial role in H_2 activation by accepting the electron density from the σH_2 orbital, particularly at the early stage of the reaction which eventually helps to weaken the H-H bond. The idea is further verified by replacing the -CH_2 with an electronegative oxygen atom which makes the adjacent tetrel atom more positively charged compared to its -CH_2 analogue. Therefore, the polarity of the E-O bond increases which makes the $\sigma^*(E\text{-}O)$ orbital a better acceptor orbital. As a consequence, while for $(C_2F_5)_3SiCH_2P(tBu)_2$ one of the $\sigma^*(E\text{-}R)$ orbital acts as a major acceptor orbital, in the case of $(C_2F_5)_3SiOP(tBu)_2$ contribution of $\sigma^*(E\text{-}O)$ orbital increases and it becomes the second major acceptor orbital (Figure 3.11). Thus, the neutral E atoms despite having no formally vacant p orbitals derive a considerable Lewis acidity from not only the σ^* orbitals of highly electron-withdrawing R groups attached to it but also from the $\sigma^*(E\text{-}CH_2)$ orbital.

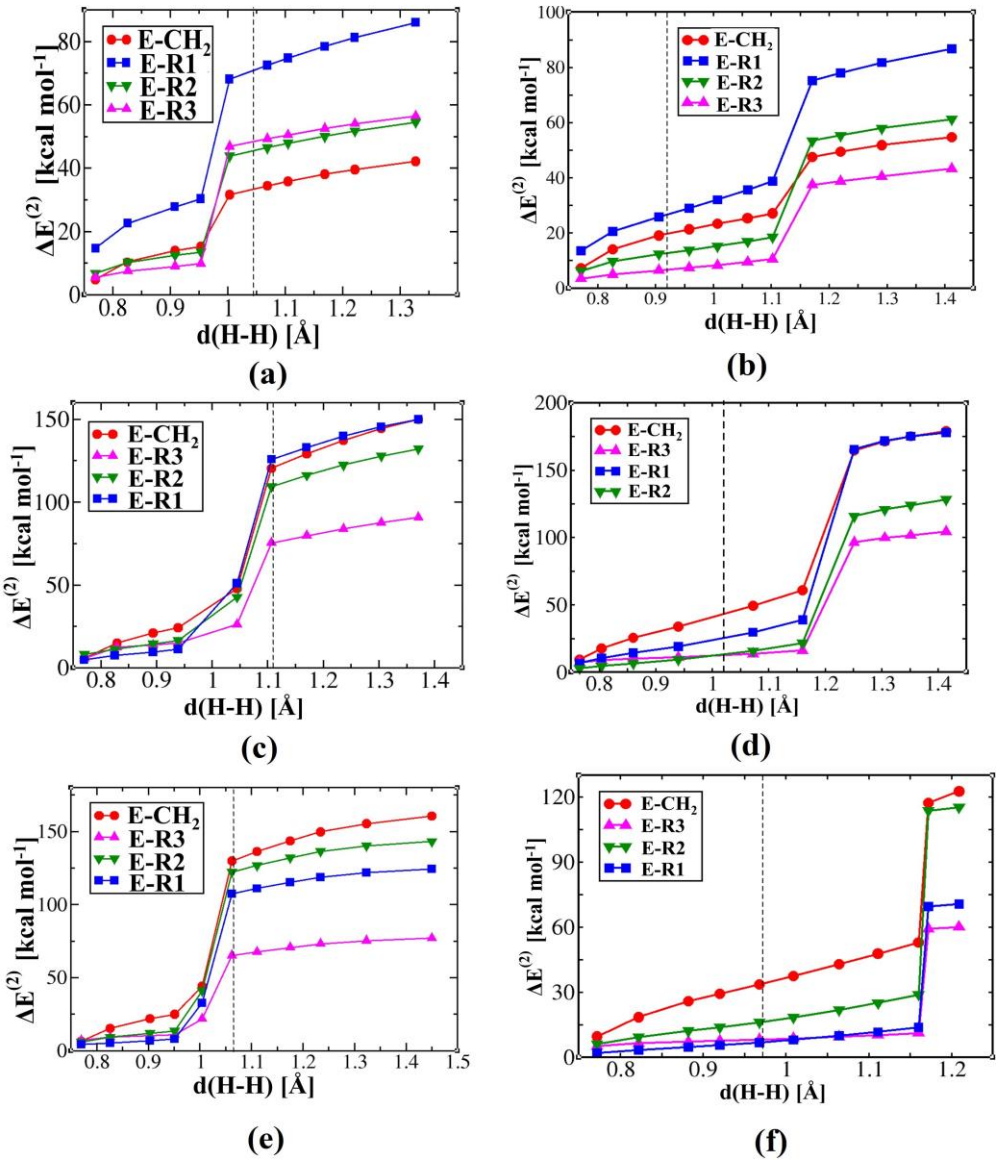

Figure 3.10: Donor-acceptor interaction energies estimated at the second-order perturbation theory level associated with interaction $\sigma H_2 \rightarrow \sigma^*(E\text{-}CH_2)/\sigma^*(E\text{-}R)$ along the minimum energy path for (a) **1-Si-P** (b) **1-Si-N**, (c) **1-Ge-P** (d) **1-Ge-N** (e) **1-Sn-P** and (f) **1-Sn-N**. The dotted lines denote the respective TS.

3.3.4 Energetics of H_2 activation

After deciding on the mechanism of H_2 activation we now compare the reactivity of the FLPs. Figure 3.12 shows the computed activation barriers (ΔG_a) along with

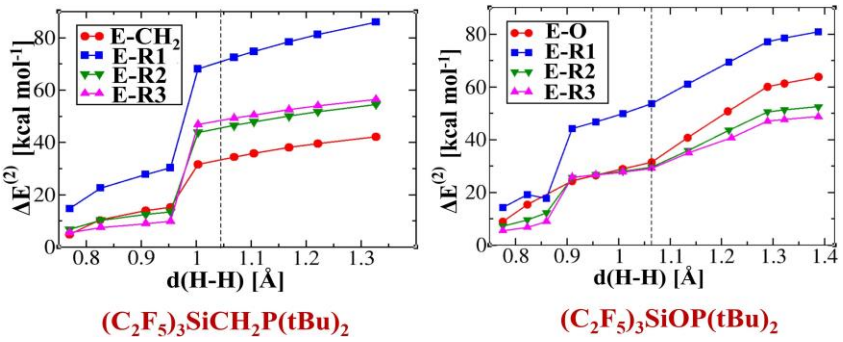

Figure 3.11: Donor-acceptor interaction energies estimated at the second-order peturbation level associated with interaction $\sigma H_2 \rightarrow \sigma^*(E\text{-}CH_2)/\sigma^*(E\text{-}R)$ along the minimum energy path for (a) **$(C_2F_5)_3SiCH_2P(tBu)_2$** (b) **$(C_2F_5)_3SiOP(tBu)_2$**.

the corresponding reaction free energies (ΔG_R) for all the FLPs. We find that for all the systems the H_2 splitting reaction is endergonic in nature. Moreover, the activation barriers differ widely among the candidates spanning a range of 12-35 kcal/mol. It is also observed that with a particular structural framework with different E atoms, the Ge containing FLP has the highest H_2 activation barrier.

Our computed results show **1-Ge-P** has an activation barrier of value 30.3 kcal/mol which is quite the highest among all the candidates whereas **1-Si-P** and **1-Sn-P** has a lower barrier of value 27.5 kcal/mol and 21.2 kcal/mol respectively. These findings are in line with experimental observations that **1-Si-P** and **1-Sn-P** activate hydrogen whereas **1-Ge-P** turned out to be inactive in this respect [20-23]. To rationalize the different reactivity of the E sites towards H_2 splitting a detailed activation-strain-analysis is performed along the entire reaction profile. The activation-strain pro-files (ASPs) are constructed with data obtained from the IRC calculations connecting the TS with two corresponding minima. The ASPs depicted in Figure 3.13 imply that **1-Sn-P** exhibit a lower activation energy barrier owing to stronger interaction energy (ΔE_{int}) and lower strain energy (ΔE_{strain}). The stronger interaction energy of **1-Sn-P** can be rationalized by its low-lying LUMO (-0.15 eV) compared to **1-Si-P** (0.25 eV) and **1-Ge-P** (0.38 eV),

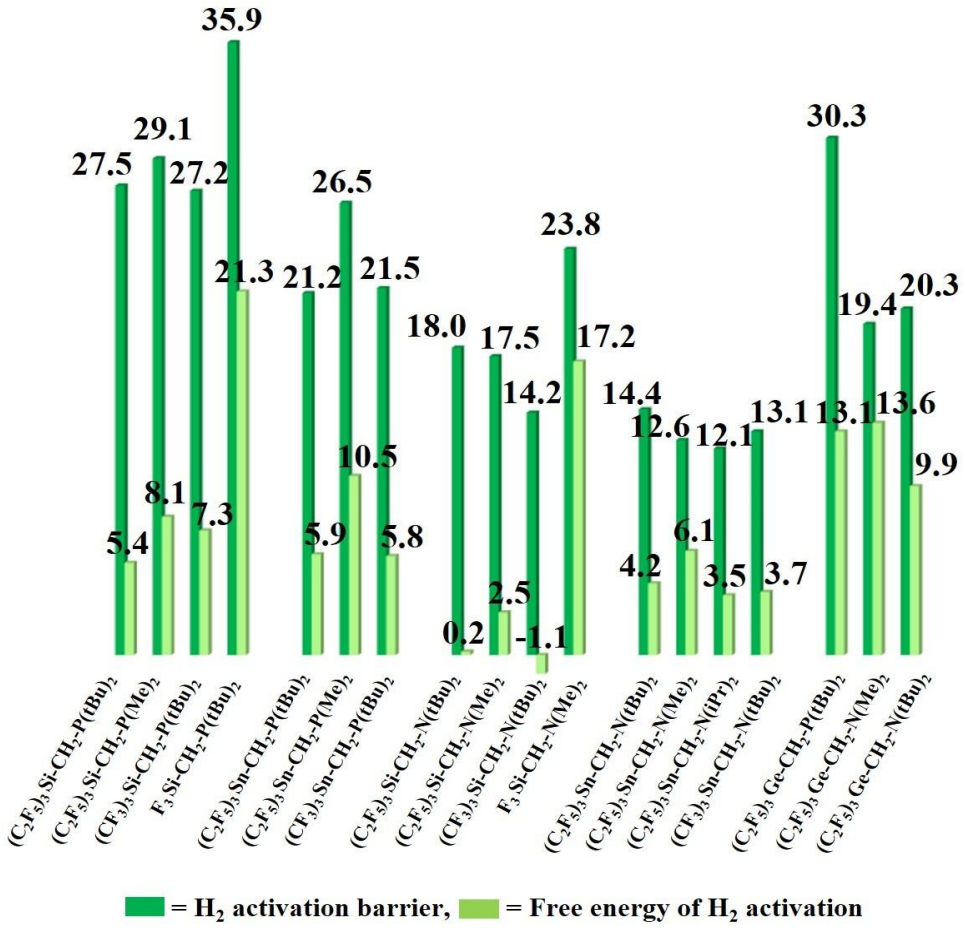

Figure 3.12: The computed values of H_2 activation barrier (ΔG_a) and Gibbs free energy of H_2 activation (ΔG_r) for all FLPs. All energies are given in kcal/mol.

leading to a more favorable interaction with the σH_2 orbital. Moreover in the case of **1-Si-P** and **1-Ge-P** while the ΔE_{int} terms are almost superimposed along the reaction pathway, the ΔE_{strain} term which is the distortion energy experienced by the reactants during the transformation widely differs for them and the highest energy barrier for **1-Ge-P** can be easily justified by its higher value of ΔE_{strain} (Figure 3.13). A closer examination of the relevant structures reveals that **1-Ge-P** suffers from a larger structural distortion to attain the required **TS1** geometry compared to **1-Si-P** and **1-Sn-P** which raise its activation barrier compared to

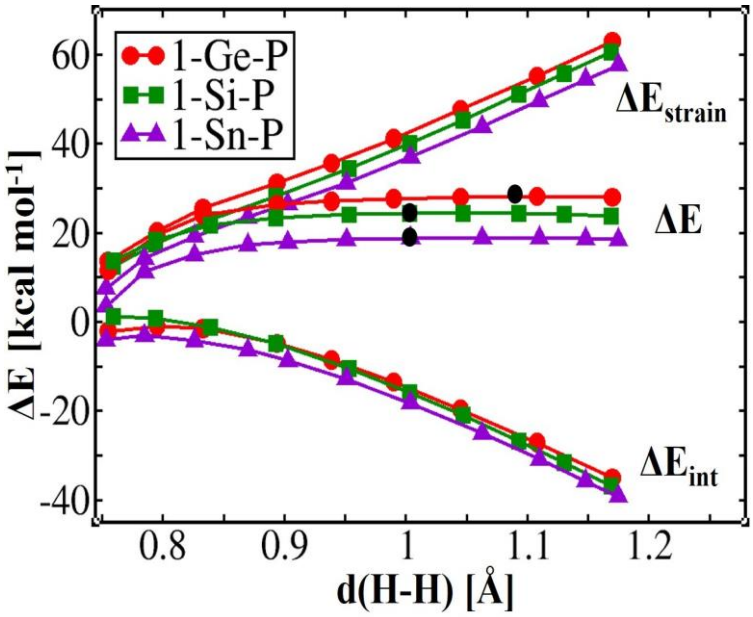

Figure 3.13: Activation-strain profiles for H_2 activation reaction by **1-Si-P** (green), **1-Ge-P** (red) and **1-Sn-P** (violet) along the reaction coordinate projected onto the H-H bond length. The black dots represent the respective TSs.

others.

Figure 3.12 also reveals that the different steric profiles of R and R' groups attached to the acidic and basic sites can also influence the energetics of the H_2 activation process. For example, the replacement of the bulky -C_2F_5 group by the -CF_3 group in the FLPs with nitrogen atom reduces the activation barrier as well as the reaction free energy. Nonetheless, this effect is less significant for the corresponding phosphorus containing FLP. Regardless of the donor site, replacing the R group from -C_2F_5 to sterically less demanding -F group has a significant impact on the energetics of H_2 activation with extremely endergonic reactions and high activation barriers which is in line with the experimental observation that F_3Si-CH_2-$P(tBu)_2$ fails to activate the dihydrogen [59]. This result can be rationalized by the back-bonding property of fluorine which is not present for C_2F_5 group [60-63]. NBO analysis shows in case of F_3Si-CH_2-$P(tBu)_2$, fluorine atom

donates its lone pair of electrons to its adjacent σ^*(C-F) orbitals which eventually reduces its ability to act as an acceptor orbital during H_2 splitting. A further careful inspection of the relevant structures reveals that in $F_3Si\text{-}CH_2\text{-}P(tBu)_2$, the coordination geometry at Si is an almost undistorted tetrahedral [three F-Si-C angles: 113.60° (113.00°),113.20° (113.00°) and 110.40° (112.70°)] whereas in $(C_2F_5)_3Si\text{-}CH_2\text{-}P(tBu)_2$ the Si atom resides in relatively distorted coordination environment (with three C-Si-C1 angles: 109.40° (109.70°), 110.10° (115.70°) and 116.30° (117.50°)]. However, the TS1 geometries for both FLPs feature a very similar distorted pentacoordinate geometry around the Si atom (at TS1, three F-Si-C angles: 124.30°,116.10° and 91.80°; three C-Si-C1 angles: 120.20°, 118.20° and 90.50°) which results in a larger rearrangement and therefore a higher strain for the F_3 substituted FLP systems. The influence of the R' group attached to the donor site of these intramolecular systems is also explored by varying the bulky -tBu group with the smaller -Me group that increases the endothermicity of the reaction. Interestingly, reducing the steric crowding at the D site slightly lowers the H_2 activation barrier for N-bearing FLPs, i.e, the activation barrier for $(C_2F_5)_3Sn\text{-}CH_2\text{-}N(Me)_2$ is reduced to 12.6 kcal/mol compared to $(C_2F_5)_3Sn\text{-}CH_2\text{-}N(tBu)_2$ with a barrier of 14.4 kcal/mol. However, for systems with a P atom, the opposite trend is observed. These findings indicate that along with the E, the D entre also plays an important role in the H-H bond cleavage by these geminal FLP systems. This assumption is further supported with another significant observation that in general, FLPs with nitrogen donor have lower activation barriers compared to analogous systems with phosphorous (Figure 3.12). Not only the H_2 activation barrier, the FLP systems with nitrogen as donor make the H_2 activation process much less endergonic. Thus, in general, N-containing FLPs exhibit a favourable H_2 activation profile compared to those with P. Similar observation is reported for closely related geminal FLPs ($Ph_2E'\text{-}CH_2\text{-}EMe_2$, E' =B, Al, Ga, In and E=N, P, As, Sb), where Fernandez and coworkers observed for a given E' LA the H_2

activation barrier follow the order N< P < As < Sb which can be correlated with the decreasing basicity of LB site along the group and has been rationalized by activation strain analysis and energy decomposition analysis [64]. To explain such a marked difference in reactivity between **1-Sn-P** and **1-Sn-N** we analyzed their H_2 activation profiles in more detail. Figure 3.14 illustrates the evolution of the E-H, D-H and H-H bonds (estimated by Wiberg bond indices plotted along the Y-axis) as a function of the progress of the reaction (estimated by plotting the H-H bond length on the X-axis).

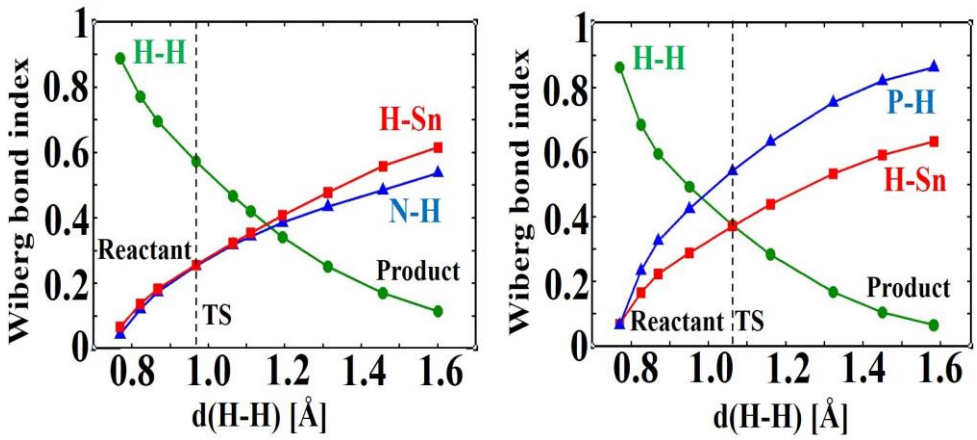

Figure 3.14: Evolution of the Wiberg bond index values for the H-H, E-H and D-H bonds for (a) **1-Sn-N** and (b) **1-Sn-P** along the pseudo-IRC path, depicted as a function of the H-H bond length. The dotted lines indicate the respective TSs.

We find that for **1-Sn-N**, from the very beginning of the reaction, the N atom engages in a donor-acceptor interaction involving σ^*(H-H) orbital. This interaction, together with and $\sigma H_2 \rightarrow \sigma^*(Sn\text{-}CH_2)$ interaction progressively weaken the H-H bond and eventually, the transition state (TS) appears around an H-H separation of 0.97 Å. At TS1, the H-H bond order drops to 0.57 with the concomitant formation of the Sn-H and N-H bonds (WBI 0.26 and 0.25 for Sn-H and N-H bond respectively), which appears to be nearly synchronous. On the contrary, for **1-Sn-P**, these two bond formations appear to be rather asynchronous with the P-H

bond formation preceding over the formation of the Sn-H bond. At the transition state, which appears relatively late at an H-H distance of 1.06 Å compared to **1-Sn-N**, the computed WBIs are 0.37, 0.37and 0.54 for H-H, Sn-H and P-H bond respectively. The earliness of P-H bond formation can be rationalized from the much lower electronegativity of P (compared to N) leading to a more facile electron transfer between the LP of the P atom and σ^*(H-H) orbital. Overall, the appearance of the TSs at different stages of the reaction profiles qualitatively explains the difference in the barrier between **1-Sn-N** and **1-Sn-P**. Thus it can be said that the lower activation energy barriers of N-bearing FLPs compared to FLPs with P donors is a consequence of the different positions of their transition states in the reaction coordinate which are shown by the black dots in their activation strain profiles. For further confirmation, good linear relationships are found by plotting the computed activation barriers against the respective H··H bond lengths in the transition states. Therefore, it can be concluded that lower activation energy barriers for N-bearing FLPs are associated with their early transition states and the higher activation energy barriers for P-containing FLPs are reflection of their late transition state, which is fully consistent with the Hammond–Leffler postulate (Figure 3.15).

A quantitative insight into the role of the D site in the H_2 activation process can be obtained by performing a detailed activation-strain-analysis for two representative systems **1-Sn-P** and **1-Sn-N**. As illustrated in Figure 3.16, both FLPs exhibit similar ASP features.A close inspection of Figure 3.16 suggests that both the strain energy (ΔE_{strain}) and the interaction energy (ΔE_{int}) terms play a decisive role in the different reactivity of **1-Sn-P** and **1-Sn-N**. For example, at an H-H distance of 1.0 Å, **1-Sn-P** shows ΔE_{strain} and ΔE_{int} value of 37.0 kcal/mol and -18.2 kcal/mol, respectively, while **1-Sn-N** features a lower ΔE_{strain} of 29.4 kcal/mol and a stronger ΔE_{int} value of -21.6 kcal/mol. Thus, the lower activation barrier in **1-Sn-N** is attributed to the stronger ΔE_{int} and lower ΔE_{strain} along the

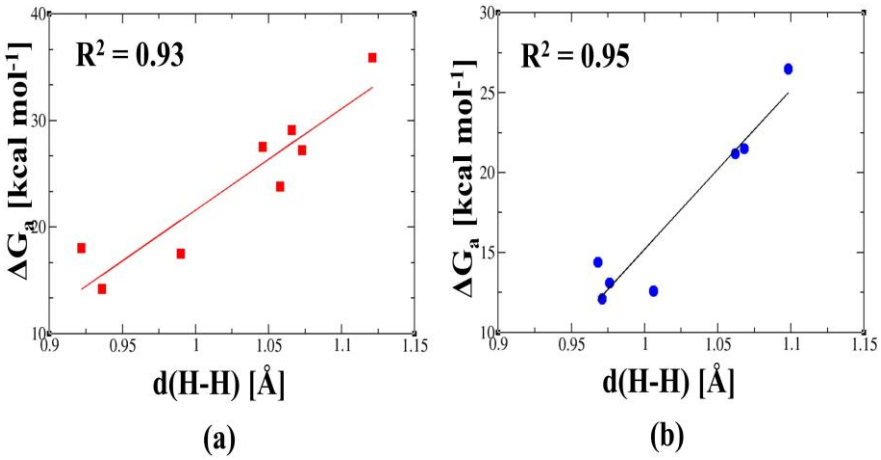

Figure 3.15: Plot of the computed activation barriers (ΔG_a) vs the H..H distance in the corresponding transition states for (a) all FLP systems with Sn Lewis acid (b) all FLP systems with Si Lewis acid.

entire reaction pathway. Such differences in the strain energy curve upon changing the D atom can be associated with the different degrees of structural alteration of the FLP motif during the progress of the reaction. One structural parameter that captures this structural difference well is the ∠E-CH_2-D angle. While at the very beginning stage of the reaction, **1-Sn-P** features a higher ∠E-CH2-D compared to **1-Sn-P** (∠Sn-C-P =114.80° and ∠Sn-C-N = 107.50°), at **TS1** this angle becomes nearly the same for both like ∠Sn-C-P = 109.10° and ∠Sn-C-N = 109.30°. This implies that to attain the **TS1** geometry, **1-Sn-P** experiences a large structural modification ($\Delta\theta$ = 5.70°) compared to **1-Sn-N** ($\Delta\theta$ = -1.80°), which is reflected in the higher activation barrier found in the former FLP. This conclusion is further confirmed by splitting the total ΔE_{strain} term into separate contributions arising from both reactants **1** and H_2 (Figure 3.17) and the plot manifests higher deformation of **1-Sn-P** than **1-Sn-N** which explains the observed trend.

Next, we analyzed the term ΔE_{int} which also plays a crucial role in determining the activation barrier. To rationalize the difference in the curve for the two systems, additional energy decomposition analysis (EDA) is performed which in-

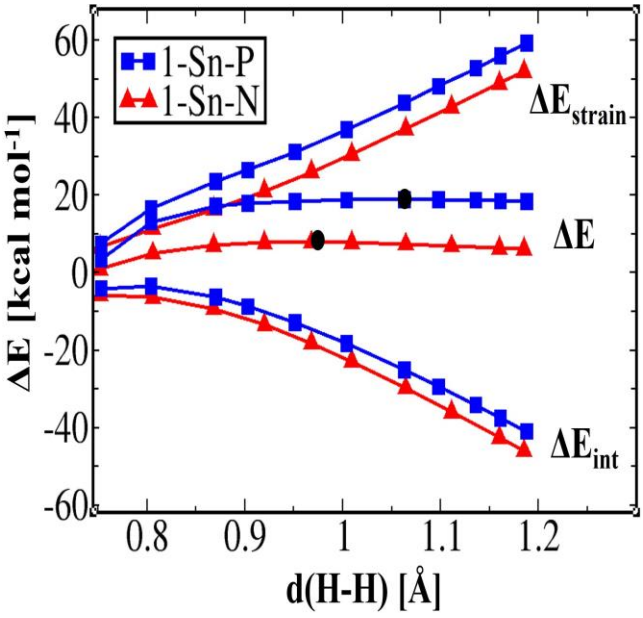

Figure 3.16: Activation-strain profiles for H_2 activation reaction by **1-Sn-P** (blue) and **1-Sn-N** (red) along the reaction coordinate depicted as a function of the H-H distance. The black dots represent the respective TSs.

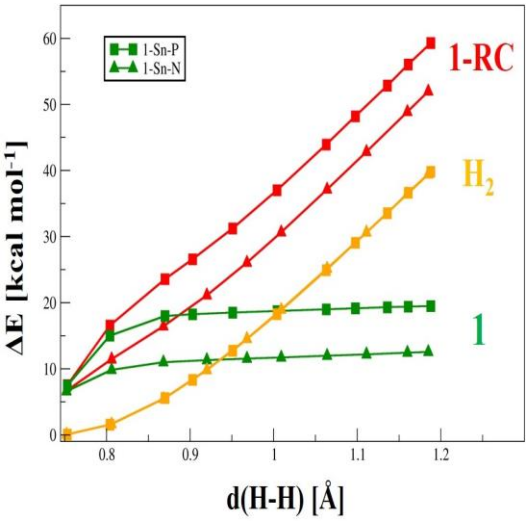

Figure 3.17: Division of strain term ΔE_{strain} into $\Delta E_{strain}(1)$ and $\Delta E_{strain}(H_2)$.

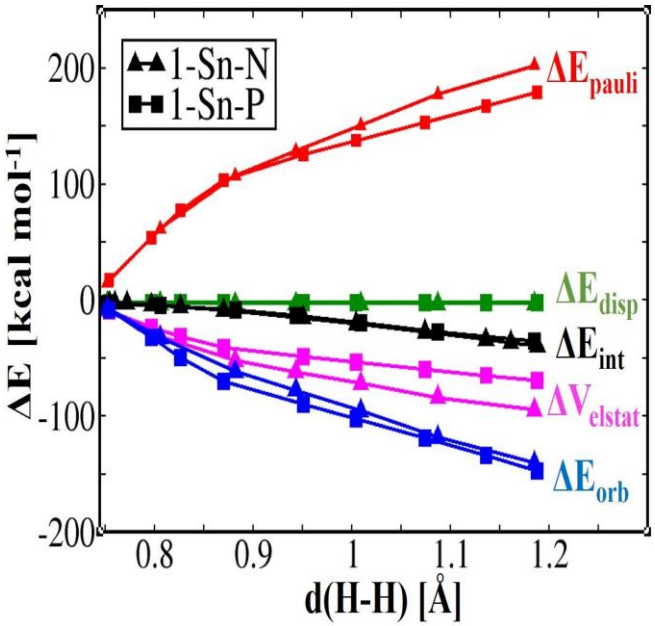

Figure 3.18: Energy-decomposition analysis for the H_2 activation reaction by **1-Sn-P** (square) and **1-Sn-N** (triangle) along the reaction coordinate depicted as a function of the H-H distance.

dicates (Figure-3.18) the different contributions of EDA terms along the reaction coordinate. We find that the contribution of the dispersion forces (ΔE_{disp}) is negligible throughout the entire reaction profile and the repulsive Pauli term (ΔE_{Pauli}) is roughly balanced by stabilizing orbital ($\Delta E_{orbital}$) and electrostatic interactions (ΔV_{elstat}). While $\Delta E_{orbital}$ is more or less comparable for Both **1-Sn-P** and **1-Sn-N** (-102.4 kcal/mol and -95.4 kcal/mol at H-H distance 1.0 Å for **1-Sn-P** and **1-Sn-N** respectively) the ΔV_{elstat} which arises due to the zwitterionic nature of the product **2**, seems to be a crucial determining factor for the different interaction energy curve in **1-Sn-P** and **1-Sn-N**. For example, at H-H =1.0 Å, ΔV_{elstat} for **1-Sn-P** is -53.3 kcal/mol but **1-Sn-N** has a much larger ΔV_{elstat} value of -71.9 kcal/mol. Overall, these findings indicate that more stabilizing ΔE_{int} and less destabilizing ΔE_{strain} explain the lower H_2 activation barrier in **1-Sn-N** compared to **1-Sn-P**. This similar rationale applies to all systems having N as D atom in general **1-E-N** FLPs are predicted to exhibit facile H_2 activation reactions.

3.4 Conclusion

In summary, in this chapter, we have investigated the mechanism of H_2 activation by a family of intramolecular FLPs featuring neutral E LA through DFT computations. Our results suggest that the H_2 activation follows a concerted pathway through a single five-membered transition state. We also found these neutral E sites, in absence of a vacant p orbital, derive a considerable Lewis acidity from not only the σ^*(E-R) orbital but also from the σ^*(E-CH_2) orbital. A detailed mechanistic investigation confirms that the two cooperative interactions LP(D)$\rightarrow\sigma^*H_2$ and $\sigma^*H_2\rightarrow\sigma^*$(E-$CH_2$)/$\sigma^*$(E-R) are responsible for cleavage of the H-H bond. By varying the substituents, the LA and the LB sites, we show how to tune the energetics of the H_2 activation. In particular, a significant difference in reactivity is observed by swapping the donor atom P to N since the latter FLPs follow a synchronous mechanism for H_2 activation resulting in an early transition state leading to lower activation barriers. Our activation-strain analyses further confirm this difference in reactivity is due to the lower value of strain energy as well as the stronger value of interaction energy between the deformed reactants along the entire reaction pathway for the N-bearing FLPs. The origin of such enhanced interactions is also analyzed employing energy decomposition analysis which discloses the stronger electrostatic interaction for FLPs with N as the donor atom. We have also gauged the influence of different E elements as the LA sites. We find Si and Sn-containing FLPs have much favourable H_2 activation energetics compared to those having Ge. This behaviour is rationalized by the ASPs which suggests stronger interaction energy and lower strain energy for Si and Sn counterparts compared to their Ge analogue.

3.5 References

[1] Niu, S.; Hall, M. B. Chem. Rev. 2000, 100 (2), 353-406.

[2] Torrent, M.; Sola, M.; Frenking, G. Chem. Rev. 2000, 100 (2), 439-494..

[3] He, T.; Tsvetkov, N. P.; Andino, J. G.; Gao, X.; Fullmer, B. C.; Caulton, K. G. J. Am. Chem. Soc. 2010, 132 (3), 910–911.

[4] Kimura, T.; Koiso, N.; Ishiwata, K.; Kuwata, S.; Ikariya, T. J. Am. Chem. Soc. 2011, 133 (23), 8880–8883.

[5] Camaioni, D. M.; Ginovska-Pangovska, B.; Schenter, G. K.; Kathmann, S. M.; Autrey, T. J. Phys. Chem. A 2012, 116 (26), 7228–7237.

[6] Paradies, J. Angew. Chem. Int. Ed. 2014, 53, 3552 – 3557.

[7] Hounjet, L. J.; Stephan, D. W. Org. Process Res. Dev. 2014, 18 (3), 385–391..

[8] Daniel J. Scott; Fuchter, M. J.; Ashley, A. E. Chem. Soc. Rev. 2017, 46, 5689-5700.

[9] Lam, J.; Szkop, K. M.; Mosaferi, E.; Stephan, D. W. Chem. Soc. Rev. 2019, 48, 3592.

[10] Paradies, J. Eur. J. Org. Chem. 2019, 283-294.

[11] Stephan, D. W.; Greenberg, S.; Graham, T. W.; Chase, P.; Has-tie, J. J.; Geier, S. J.; Farrell, J. M.; Brown, C. C.; Heiden, Z. M.; Welch, G. C.; Ullrich, M. Inorg. Chem. 2011, 50, 12338–12348.

[12] Gyömöre, A.; Bakos, M.; Földes, T.; Pápai, I.; Domján, A,; Soós, T. ACS Catal. 2015, 5 (9), 5366–5372.

[13] Scott, D. J.; Simmons, T. R.; Lawrence, E. J.; Wildgoose, G. G.; Fuchter, M. J.; Ashley, A. E. ACS Catal. 2015, 5 (9), 5540–5544.

[14] Bergquist, C.; Bridgewater, B. M.; Harlan, C. J.; Norton, J. R.; Friesner, R. A.; Parkin, G. J. Am. Chem. Soc. 2000, 122 (43), 10581–10590.

[15] Das, S.; Pati, S. K. Chem. Eur. J. 2017, 23, 1078 –1085. .

[16] Weicker, S. A.; Stephan, D. W. Bulletin of the Chemical Society of Japan

2015, 88, (8).

[17] Whittell, G. R.; Balmond, E. I.; Robertson, A. P. M.; Patra, S. K.; Haddow, M. F.; Manners, I. Eur. J. Inorg. Chem. 2010, 3967–3975.

[18] Schäfer, A.; Reißmann, M.; Schäfer, D. A.; Saak, W.; Haase, D.; Müller, P. D. T. Angew. Chem. Int. Ed. 2011, 50, 12636 –12638.

[19] Bayne, J. M.; V. Fasano; Szkop, K. M.; Ingleson, M. J.; Steph-an, D. W., Phosphorous(v) Lewis acids Chem. Commun. 2018, 54, 12467.

[20] Waerder, B.; Pieper, M.; Körte, L. A.; Kinder, T. A.; Mix, A.; Neumann, B.; Stammler, H.-G.; Mitzel, N. W. Angew. Chem. Int. Ed. 2015, 54, 13416 –13419.

[21] Kinder, T. A.; Pior, R.; Blomeyer, S.; Neumann, B.; Stammler, H.-G.; Mitzel, N. W. Chem. Eur. J. 2019, 25, 5899 –5903.

[22] Holtkamp, P.; Friedrich, F.; Stratmann, E.; Mix, A.; Neumann, B.; Stammler, H.-G.; Mitzel, N. W. Angew.Chem. Int. Ed. 2019, 58, 5114 –5118.

[23] Holtkamp, P.; Schwabedissen, J.; Neumann, B.; Stammler, H.-G.; Koptyug, I. V.; Zhivonitko, V. V.; Mitzel, N. W. Chem. Eur. J. 2020, 26, 17381 –17385. .

[24] Grimme, S.; Kruse, H. Goerigk, L.; Erker, G. Angew. Chem. Int. Ed. 2010, 49, 1402 –1405.

[25] Rokob, T. A.; Hamza, A.; Stirling, A.; Soos, T.; Pápai, I. Angew. Chem. Int. Ed. 2008, 47, 2435 –2438..

[26] Hamza, A.; Stirling, A.; Rokob, T. A.; Pápai, I. International Journal of Quantum Chemistry. 2009, 109, 2416 –2425.

[27] Rokob, T. A.; Hamza, A.; Stirling, A.; Pápai, I. J. Am. Chem. Soc. 2009, 131 (5), 2029–2036..

[28] Rokob, T. A.; Hamza, A.; Pápai, I. J. Am. Chem. Soc. 2009, 131 (30), 10701–10710.

[29] Rokob, T. A.; Bako, I.; Stirling, A.; Hamza, A.; Pápai, I. J. Am. Chem. Soc. 2013, 135 (11), 4425–4437.

[30] Rokob, T. A.; Pápai, I. Top. Curr. Chem. 2013, 332, 157-211.

[31] Zhao, Y.; Truhlar, G. D.Theor. Chem. Account. 2008, 120, 215241.

[32] Zhao, Y.; Truhlar, G. D. Acc. Chem. Res. 2008, 41, 157167.

[33] Semeniuk, O.; Csik, A.; Kökényesi, S.; Reznik, A. Ion-assisted deposition of amorphous PbO layers. Journal of Materials Science 2017, 52(13), 7937-7946.

[34] Grimme, S.; Antony, J.; Ehrlich, S.; Krieg, H. J. chem. phys. 2010, 132, 154104-154119.

[35] Andrae, D.; Haeussermann, U.; Dolg, M.; Stoll, H.; Preuss, H.Theor. Chem. Account. 1990, 77, 123-141.

[36] Marenich, A. V.; Cramer, C. J.; Truhlar, D. G. J. Phys. Chem. B. 2009, 113, 6378639.

[37] Glendening, D. E.; Reed, A. E.; Carpenter, J. E.; Weinhold, F., NBO, version 3.1.

[38] Frisch, M. J. et al., Gaussian 16 Revision A.03. 2016; Gaussian Inc. Wallingford CT.

[39] A. Diefenbach; De Jong; Bickelhaupt, G. T., Molecular Physics 2005, 103, 995–998.

[40] Bickelhaupt, F. M.; Houk, K. N., Angew. Chem. Int. Ed. 2017, 56, 10002–10002.

[41] Zeist, V.; Bickelhaupt ,W.-J. Organic biomolecular chemistry 2010, 8, 3118–3127.

[42] Ziegler, T.; Rauk, A. Inorganic Chemistry 1979, 18, 1755–1759.

[43] Ziegler, T.; Rauk, A. Theoretical Chemistry Accounts: Theory, Computation, and Modeling (Theoretica Chimica Acta) 1977, 46, 1-10.

[44] Mitoraj, M.; Michalak, A. Journal of molecular modeling 2007, 13, 347– 355.

[45] Srebro, M.; Michalak, A. Inorganic chemistry 2009, 48, 5361–5369.

[46] Mitoraj, M. P.; Michalak, A.; Ziegler, T. Journal of chemical theory and computation 2009, 5, 962–975.

[47] Michalak, A. M., M. The Journal of Physical Chemistry A 2008, 112, 1933–1939.

[48] ADF2017, SCM, Theoretical Chemistry, Vrije Universiteit, Amsterdam, The

Netherlands, https://www.scm.com.

[49] Skara, G.; Pinter, B.; J. Top; Geerlings, P.; Proft, F. D.; Vleeschouwer, F. D. Chemistry-A European Journal 2015, 21, 5510–5519.

[50] Lenthe, E. v.; Baerends, E. J.; Snijders, J. G. The Journal of chemical physics 1994, 101, 9783–9792.

[51] Lenthe, E. v.; Ehlers, A.; Baerends, E. J. The Journal of chemical physics 1999, 110, 8943–8953.

[52] Waerder, B.; Steinhauer, S.; Bader, J.; Neumann, B.; Stammler, H.-G.; Vishnevskiy, Y. V.; Hoge, B.; Mitzel, N. W. Dalton Trans. 2015, 44,13347-13358.

[53] Mitzel, N. W.; Vojinovic, K.; Foerster, T.; Robertson, H. E.; Borisenko, K. B.; Rankin, D. W. H. Chem. Eur. J. 2005, 11, 5114 – 5125.

[54] Kinder, T. A.; Blomeyer, S.; Franke, M.; Depenbrock, F.; Neu-mann, B.; Stammler, H.-G.; Mitzel, N. W. Eur. J. Inorg. Chem. 2019, 35, 3933-3939.

[55] Bertini, F.; Lyaskovskyy, V.; Timmer, B. J. J.; Kanter, F. J. J. d.; Lutz, M.; Ehlers, A. W.; Slootweg, J. C.; Lammertsma, K.J. Am. Chem. Soc. 2012, 134(1), 201–204.

[56] Waerder, B.; Steinhauer, S.; Bader, J.; Neumann, B.; Stammler, H.-G.; Vishnevskiy, Y. V.; Hoge, B.; Mitzel, N. W. Dalton Trans. 2015, 44,13347-13358.

[57] Christopher B. C.; Lindsay J. H.; Dobrovetsky, R.; Stephan, D. W. Science 2013, 341 (6152), 1374-1377.

[58] Swamy, K. C. K.; Kumar, N. S. Acc. Chem. Res. 2006, 39 (5), 324–333.

[59] Kinder, T. A.; Blomeyer, S.; Franke, M.; Depenbrock, F.; Neu-mann, B.; Stammler, H.-G.; Mitzel, N. W. Eur. J. Inorg. Chem. 2019, 35, 3933-3939.

[60] Wiesemann, M.; Hoge, B. Chem. Eur. J. 2018, 24, 16457 –16471.

[61] Böttcher, T.; Steinhauer, S.; Neumann, B.; Stammler, H.-G.; Röschenthaler, G. V.; Hoge, B. Chem.Commun. 2014, 50, 62046206.

[62] Mitzel, N. W.; Vojinovic, K.; Fröhlich, R.; Foerster, T.; Robert-son, H. E.; Borisenko, K. B.; Rankin, D. W. H. J. Am. Chem. Soc. 2005, 127, 1370513713.

[63] Mitzel, N. W.; Losehand, U.; Wu, A.; Cremer, D.; Rankin, D. W. H. J. Am. Chem. Soc. 2000, 122, 44714482.

[64] Cabrera-Trujillo, J. J.; Fernandez, I. Chem. Eur. J. 2018, 24, 1782317831.

4

Assessing Tetrel-based Neutral Frustrated Lewis Pairs for Catalytic Hydrogenation

Work reported in this chpater is based on: Pallavi Sarkar, Shubhajit Das, Swapan K Pati, J. Phys. Chem. C. 2021, 125, 41. 22522-22530. Reproduced with permission from American Chemical Society.

4.1 Introduction

In the previous chapter, we have presented detailed mechanistic studies on H_2 splitting by a series of Tetrel based neutral intramolecular frustrated Lewis pairs (FLPs). Continuing along the same line, in this chapter, we wish to extend our understanding to the full mechanism of the catalytic hydrogenation of unsaturated organic substrate by these geminal FLPs.

Since the demand for utilization of carbon dioxide (CO_2) as chemical feedstock is exponentially increasing and hydrogenation of CO_2 to formic acid is a leading approach to exploit CO_2 for the production of value-added chemicals [1] we are interested to know whether these neutral geminal FLPs can perform CO_2 hydrogenation or not. Additionally, we focused on the hydrogenation of carbonyl and imine substrates as these are the building blocks of a large number of organic reactions.

Hydrogenation of unsaturated bond by an FLP has been shown to occur with two pivotal steps (Figure 4.1). At first, the FLP which are generally represented as **1** performs heterolytic activation of hydrogen molecule. Note that homolytic splitting of H_2 by FLP via single electron transfer radical pathway has also been reported in the literature [2-3]. Next the H_2-activated product **2** can further transfer the proton and the hydride ions attached to it to an unsaturated bond X=Y. To incorporate the H_2 activation step into a catalytic hydrogenation cycle, we would require a close to reversible H_2 activation with a feasible activation barrier. To this end, we have selected a series of 13 representatives FLPs which have a feasible H_2 activation barrier and aim to (i) examine the possibility of dihydrogen release (DHR) toward, CO_2, carbonyl and imine and (ii) identify the features of the FLPs as well as the unsaturated substrates that influence the hydrogenation reactions.

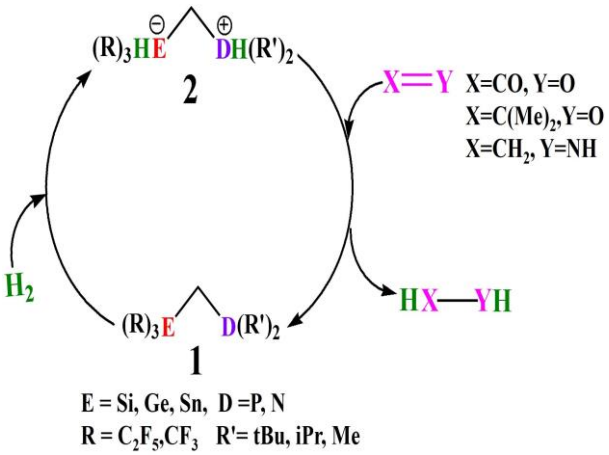

Figure 4.1: The proposed scheme for catalytic hydrogenation of an unsaturated substrate X=Y.

4.2 Computational details

All molecular geometries are optimized at the density functional theory (DFT) level using M062X functional [4-5]. For lighter atoms (C, H, N, P, O, F), 6-311G(d,p) basis set and def2TZVP for the Si, Ge and Sn including Stuttgart-Dresden effective core potential is employed [6]. Additionally, to account for the non-covalent interactions, Grimme's D3 dispersion model is used [7]. This basis set combination is hereafter denoted as BS-I. The electronic energies are further refined with single-point energy calculations using a higher basis set 6-311++G(d,p) for the lighter atoms. Here-after, we have denoted the basis set combination 6-311++G(d,p)(C, H, N, P, O, F)+(def2TZVP+ECP)(Si,Ge,Sn)// 6-311G(d,p)(C, H, N, P, O, F)+(def2TZVP+ECP)(Si,Ge,Sn) as BS2. For each optimized geometry harmonic vibrational frequency are computed to characterize the stationary points either as minima (zero imag-inary frequency) or first-order saddle points, one imaginary frequency. Transition states (TSs) are further verified by intrinsic reaction coordinate (IRC) calculations by checking their connection to two respective minimum structures. All thermochemical data are obtained with the ideal gas-rigid rotor-simple harmonic oscillator approximations at 298.15 K and 1 atm.

Zero point-energy corrections are included in the Gibbs free energy values along with a concentration correction for c = 1 mol/ dm^3 condition in the solvent. The solvent (THF) effects are taken into account by the SMD solvation model [8]. All-natural bond orbital (NBO) analyses are performed using the NBO 3.1 package [9]. All geometry optimization and single point energy calculations are performed using the Gaussian 16 suite of programs [10]. Note thai in this chapter following colour code C (grey), H (white), Si (purple), Sn (green), O (red), N(blue), F (fluorescent green) have been used.

4.2.1 Activation-strain analysis

Activation-strain analysis is performed to analyze by considering a bimolecular reaction between the hydrogenated FLP and the unsaturated substrate [11-13]. According to this model, potential energy surface ΔE is decomposed into two main contributions, the strain energy ΔE_{strain}, the distortion energy experienced by the deformed reactants during the transformation and the interaction energy ΔE_{int}.

$$\Delta E(r) = \Delta E_{strain}(r) + \Delta E_{int}(r)$$

$$\Delta E_{strain} = \Delta E_{strain}(2\text{-FLP}) + \Delta E_{strain}(X{=}Y)$$

Here the reaction coordinate (r) is defined as the projection of the IRC onto the (D/E)H…X distance which undergoes a well-defined change during the course of the reaction from the initial reaction complexes to the corresponding transition states.

4.3 Results and discussions

4.3.1 Catalytic hydrogenation of Carbon-dioxide

Figure 4.2 shows the relative Gibbs free energy profiles for the full catalytic cycle of CO_2 hydrogenation by a prototype system $(C_2F_5)_3Si\text{-}CH_2\text{-}N(tBu)_2$ (denoted as **1-Si-N**). The catalytic cycle begins with the heterolytic cleavage of the hydrogen molecule by the FLP. After H_2 activation the hydrogenated intermediate **2-Si-N** forms an initial reactant complex **3^{CO_2}-Si-N** where it establishes an N-H...O hydrogen bonding interaction with the O atom of CO_2 (Figure 4.3). As a result, the hydridophilicity of CO_2 is increased which is reflected by the higher NPA atomic charge of the carbon atom of bound CO_2 molecule in **3CO_2-Si-N** (1.071 vs 1.036) compared to that of the free CO_2. This interaction is further reinforced with the advancement of the reaction. Apart from this, another interaction like the σ(Si-H)→π^*(C=O) interaction, which is negligible at the beginning of

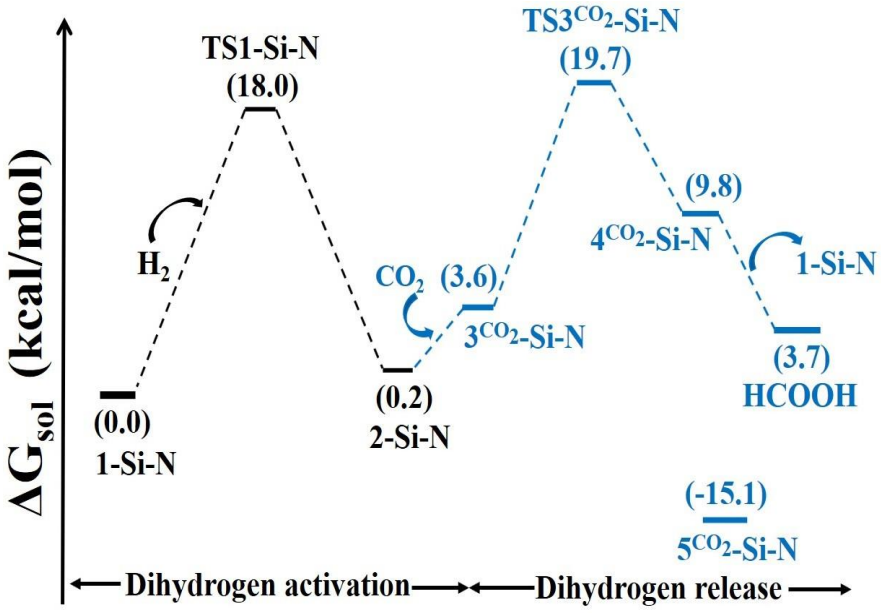

Figure 4.2: Relative Gibbs free energy profiles for catalytic hydrogenation of CO_2 by **1-Si-N**. Solvent-corrected Gibbs free energy (kcal/mol) values are given in parenthesis.

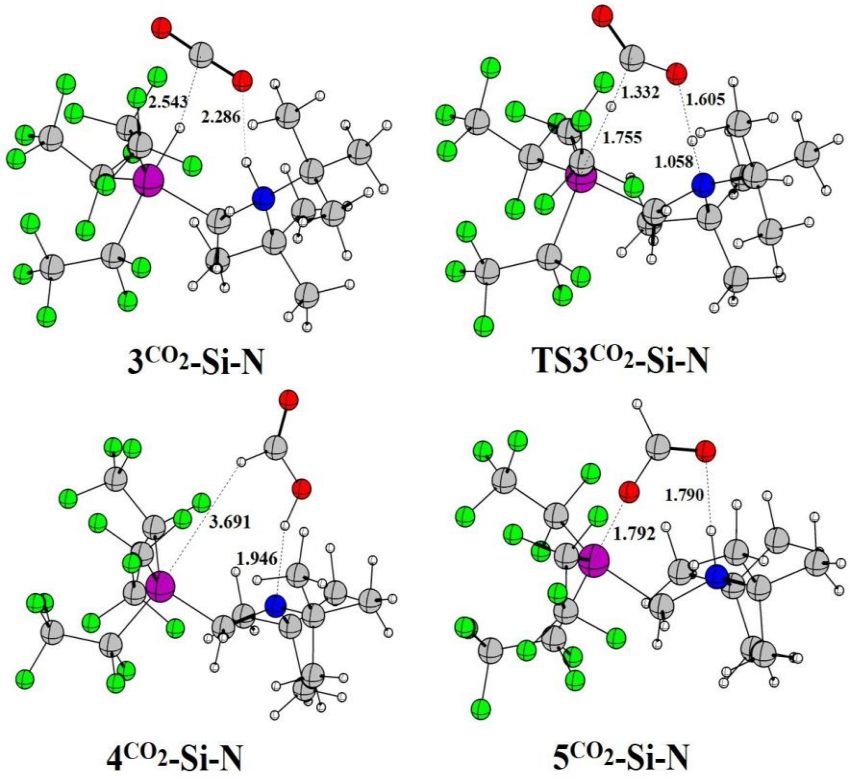

Figure 4.3: Geometry optimized structures of the intermediate(s)/TS involved in the DHR of **2-Si-N** to CO_2. All distances are given in Å. .

the hydrogenation process, becomes increasingly more significant with the progress of the reaction (Figure 4.4). Consequently, we find that the hydrogenation of CO_2 proceeds via a single concerted Transition state **TS3^{CO_2}-Si-N** with the migration of the hydride ion from the Si centre towards the carbon atom of CO_2 followed by a proton transfer from N centre towards the electronegative O atom. A closer inspection of the structure of the TS for DHR, **TS3^{CO_2}-Si-N** reveals that the hydride transfer (HT)/proton transfer (PT) is asynchronous. This is a typical case of Brønsted acid activation (BAA) in which the DH...O H-bonding interaction activates the unsaturated substrate towards the acceptance of the hydride. The nonparallel nature of the reaction can be demonstrated (Figure 4.5) by monitoring the evolution of Si-H, N-H, C-H and O-H bonds (estimated by Wiberg bond

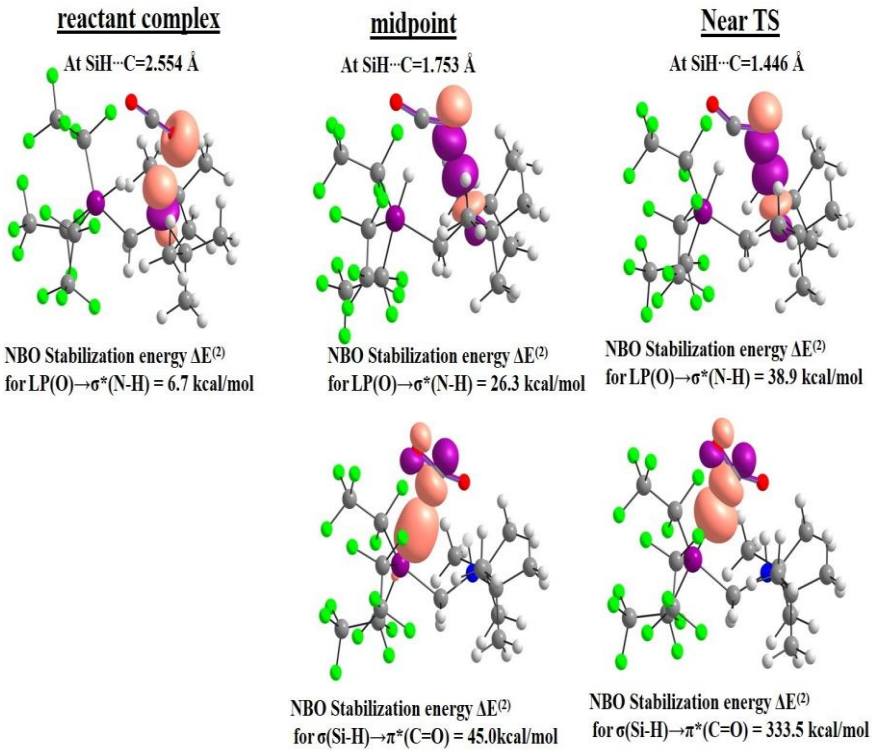

Figure 4.4: Natural Bond Orbitals (NBOs) for the reaction between **2-Si-N** and CO_2 highlighting the major interactions at three key points (reactant complex, midpoint amd TS) along the reaction coordinate.

indices along the Y-axis) with the progress of the reaction (estimated by plotting the SiH…C bond distance on the X-axis).As a result, formic acid is produced as a product that remains bound to the catalyst through a weak non-covalent interaction, leading to the formation of $\mathbf{4}^{CO_2}$**-Si-N**. Moreover, the formic acid can also engage in an H-bonding interaction with the D centre of the FLP which eventually leads to deprotonation of formic acid to formate ion. The deprotonated species is designated as $\mathbf{5}^{CO_2}$**-Si-N** which features an N-H bond and an alkoxide Si-O bond (Figure 4.3). This actually blocks the active centres of FLP for further H_2 activation. Therefore, thermal dissociation of this complex is required to resume the catalytic process.

Similar reaction profiles to that discussed above for the CO_2 hydrogenation

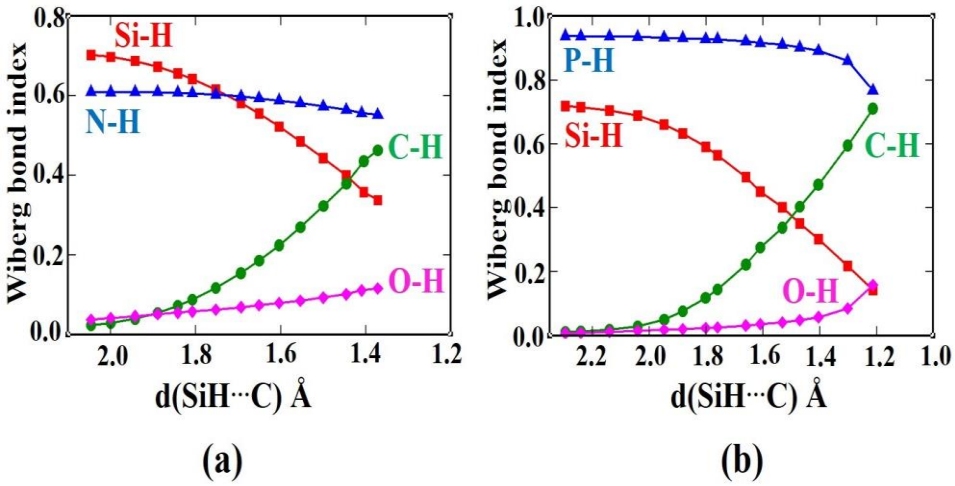

Figure 4.5: Evolution of Wiberg bond index values for the Si-H, D-H, C-H and O-H bonds for (a) **1-Si-N** and (b) **1-Si-P** along the pseudo-IRC path depicted as a function of the SiH...C distance for CO_2 hydrogenation.

have been computed for the rest of the systems. The resemblance of the optimized geometries of the associated saddle points suggests that all the FLPs follow a similar mechanism for CO_2 hydrogenation. Figure 4.6 depicts the computed activation energy barrier (ΔG_a) and the corresponding reaction energy ($\Delta G_4 CO_2$) for all the FLPs. We find the activation barrier for DHR differs widely among the systems spanning a range of 17-29 kcal/mol. It is observed under a similar structural framework the Ge containing systems have a higher barrier for CO_2 hydrogenation compared to other E centres and this trend is exactly in accordance with their H_2 activation barrier order (Ge > Si > Sn). As shown in Figure 4.6, electron-donating substituents R' attached to the D centre have an influence on the DHR barrier. For example, the replacement of the -tBu group of **1-Si-N** with a less bulky –Me group increases the activation barrier from 19.7 kcal/mol to 24.6 kcal/mol. On the contrary, the influence of R groups attached to the E centre is less pronounced which is reflected in the very close DHR barriers of $(C_2F_5)_3$Si-CH_2-N$(tBu)_2$ and $(CF_3)_3$Si-CH_2-N$(tBu)_2$ of value 19.7 kcal/mol and 17.6 kcal/mol respectively. We

find that among all the factors, particularly the D centre of the FLP largely controls the CO_2 hydrogenation barrier. It is found that the FLPs with N Lewis base can perform CO_2 hydrogenation with a much lower DHR barrier compared to the analogous systems with P.

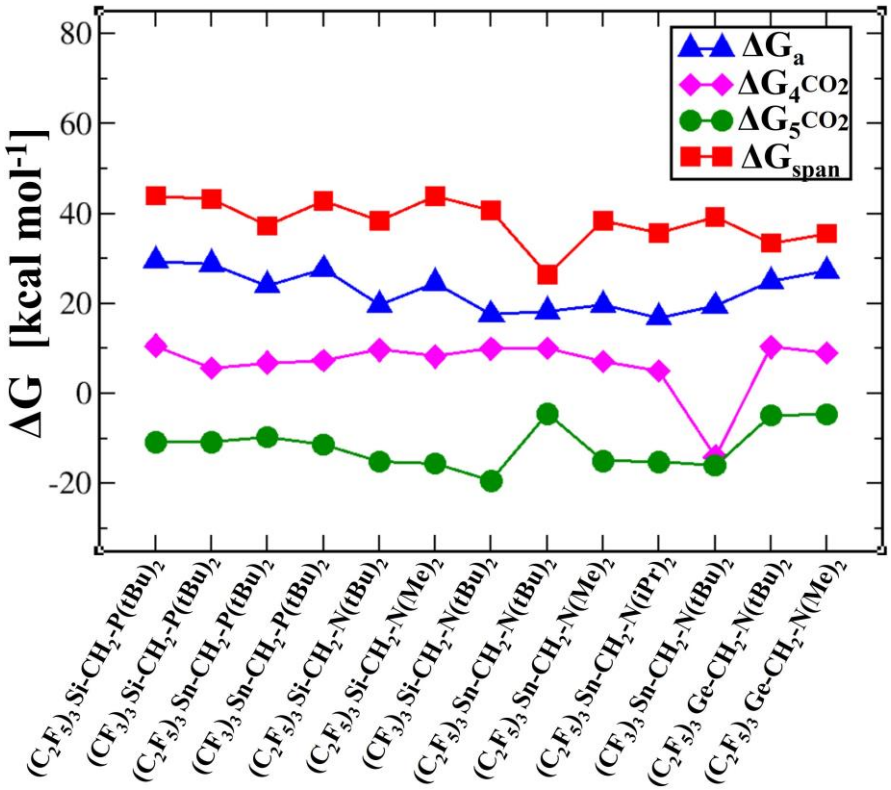

Figure 4.6: The computed values of CO_2 hydrogenation barrier, Free energies of CO_2 hydrogenation and the energy spans for all FLPs. All energies are given in kcal/mol.

To examine the underlying reason a detailed activation strain analysis is performed along the reaction coordinate, from reactant to TS, considering a bimolecular reaction between the hydrogenated FLP **2** and CO_2. Within this frame-work, the activation energy (ΔE_{act}) of CO_2 hydrogenation is decomposed into strain energy ΔE_{strain}, the distortion energy experienced by the deformed reactants during the transformation and the interaction energy ΔE_{int}.

$$\Delta E = \Delta E_{strain} + \Delta E_{int}$$

$\Delta E_{strain} = \Delta E_{strain}(2\text{-FLP}) + \Delta E_{strain}(CO_2)$

Figure 4.7 depicts the corresponding activation strain profiles (ASPs) projected along with the SiH…C bond-forming distance for the CO_2 bound complex of two representative systems $(C_2F_5)_3Si\text{-}CH_2\text{-}P(tBu)_2$ (denoted as **3-Si-P**) and $(C_2F_5)_3Si\text{-}CH_2\text{-}N(tBu)_2$ (denoted as **3-Si-N**). ASPs reveal that two systems have very close interaction energy; i.e, at SiH…C distance of 1.4 Å(very close to TS), **3-Si-N** shows ΔE_{int} value of 30.03 kcal/mol and for **3-Si-P**, ΔE_{int} is 31.0 kcal/mol. Whereas at the same distance ΔE_{strain} for **3-Si-P** and **3-Si-N** is 43.0 kcal/mol and 35.3 kcal/mol respectively. This result demonstrates the differences in their strain energy profile is the origin of the different reactivity of the two systems towards CO_2 hydrogenation. To analyze further the total ΔE_{strain} is divided into two contributions arising from reactants **2-FLP** and CO_2. Figure 4.8

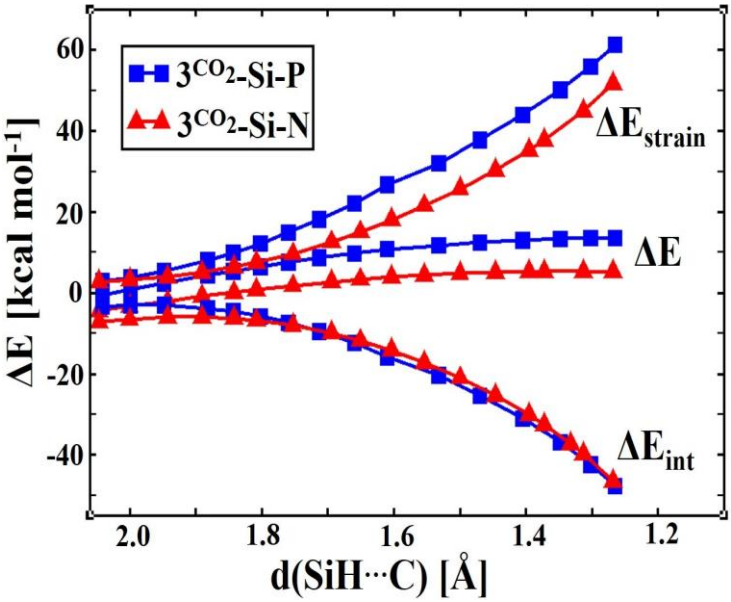

Figure 4.7: Activation-strain profiles for CO_2 activation reaction by **3-Si-P** (blue) and **3-Si-N** (red) along the reaction coordinate depicted as a function of the SiH…C distance.

demonstrates the higher deformation of **2-Si-P** than **2-Si-N** particularly at the initial stage of the reaction. Towards the TS, the difference in the distor-

tion energies of CO_2 molecules in two FLP-complexes becomes pronounced which explain the higher hydrogenation barrier for **3-Si-P**.

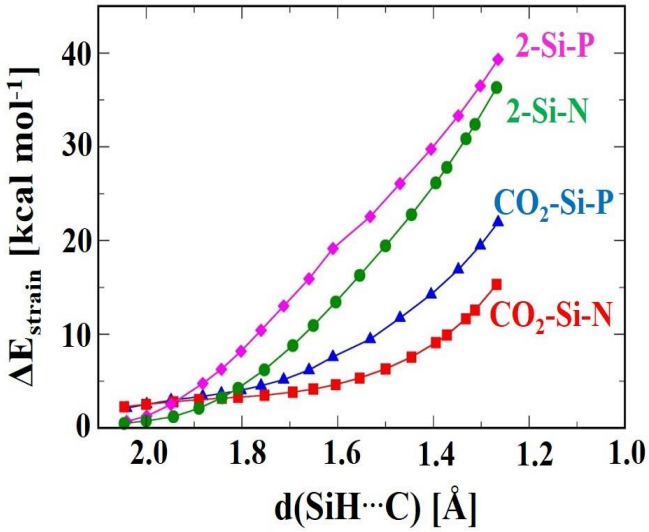

Figure 4.8: Division of strain term ΔE_{strain} into ΔE_{strain}(2-FLP) and $\Delta E_{strain}(CO_2)$.

Apart from the DHR barrier the main difficulty of CO_2 hydrogenation lies in the formation of $\mathbf{5}^{CO_2}$ species which lies quite downhill in the free energy profile for some of the FLPs (Figure 4.6). Along with the DH...O H-bonding interaction, NBO analysis of $\mathbf{5CO_2}$ complex reveal the presence of LP of (C)O→σ^*(E-R)/σ^*(E-CH_2) interaction (estimated 2nd order PT level ΔE(2)=73.47 kcal/mol for $\mathbf{5CO_2}$**-Si-N**) which provides an extra stabilization. Therefore, the thermal dissociation of this complex will also contribute to the overall energy barrier. Our computational results reveal that the DHR barrier $\mathbf{TS3}^{CO_2}$ is higher in every case compared to the H_2 activation barrier **TS1**. In this context, we applied the energetic span model (ESM) proposed by Kozuch and Shaik to compute free energy spans for CO_2 hydrogenation by these geminal FLP systems [14].

According to the ESM the energetic span ΔE can be defined as

ΔE = TTDTS - ITDI if TDTS appears after TDI

ΔE = TTDTS - ITDI + ΔG if TDTS appears before TDI

Where TTDTS is the energy of the turnover determining transition state (TDTS), ITDI is the energy of the turnover determining intermediate (TDI) and ΔG is the free energy change of the reaction.

For the CO_2 hydrogenation cycle, TDTS corresponds to **TS3CO$_2$** and **5CO$_2$** constitutes the TDI. Figure 4.6 indicates that $(C_2F_5)_3Sn\text{-}CH_2\text{-}N(tBu)_2$ with an energy span of 26.8 kcal/mol, can be a suitable candidate to perform CO_2 hydrogenation reaction under experimentally accessible conditions while a higher temperature will be required to perform the reaction for other systems.

4.3.2 Catalytic hydrogenation of carbonyls and imines

Next, we turn our attention to examine the hydrogen transfer ability of these geminal FLP systems towards carbonyl and imine substrates. To this end, Me_2CO and H_2C=NH have been selected as model carbonyl and imine substrates. The geometry optimized structures of the intermediates and the TSs involved in the hydrogenation pathway of Me_2CO and H_2C=NH substrates are shown in Figure 4.9. Figure 4.10 depicts the corresponding relative Gibbs energy profiles of hydrogenation reaction by **1-Si-N**. At the beginning of the hydrogenation cycle an initial reactant complex, **3^{XY}-Si-N** (XY represents CO and im for Me_2CO and H_2CNH, respectively) is formed which features an NH···O/N hydrogen bonding interaction between **2-Si-N** and the basic O/N atom of the substrate. Similar to CO_2 hydrogenation, dihydrogen release to Me_2CO and H_2C=NH also occurs via a single concerted TS, **TS3^{XY}-Si-N**. Owing to a very similar electrophilic character Me_2CO hydrogenation follows a very similar mechanism to CO_2. The H-bonding interaction of Me_2CO with the **2** increases the electrophilicity of the carbonyl carbon atom (NPA charge of C is 0.67 in **3^{CO}-Si-N** compared to 0.61 in free Me_2CO) and the oxygen atom becomes more electron-rich in nature (NPA charge of O is

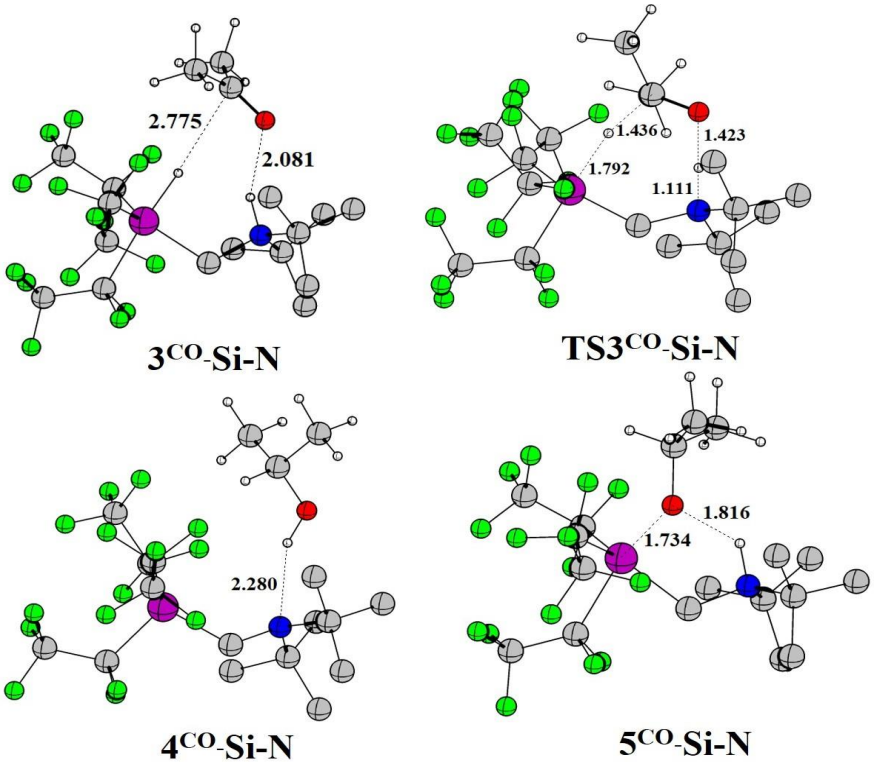

Figure 4.9: Geometry optimized structures of the intermediate(s)/TS involved in the DHR of **2-Si-N** to Me_2CO. All distances are given in Å. The hydrogen atoms attached to the carbon atoms of FLP are omitted for clarity.

-0.643 in **3^{CO}-Si-N** vs 0.549 in free Me_2CO). As a result, a hydride transfer takes place from the E centre of the FLP system towards the electrophilic carbon of Me_2CO which is followed by the subsequent proton transfer from the D centre to the oxygen atom. However, it is observed that whereas most of the FLPs follow the above-mentioned mechanism for Me_2CO hydrogenation, only for two **Si/P** systems, $(CF_3)_3Si\text{-}CH_2\text{-}P(tBu)_2$ and $(C_2F_5)_3Si\text{-}CH_2\text{-}P(tBu)_2$, the proton transfer process competes with the hydride transfer rate (Figure 4.10). This behaviour can be rationalized by the lower electronegativity of the P centre which allows the oxygen centre of Me_2CO to access the proton attached with the P centre much more easily compared to other systems.

Figure 4.11 depicts that the transition state **$TS3^{XY}$-Si-N** lies at 28.4 and 20.1

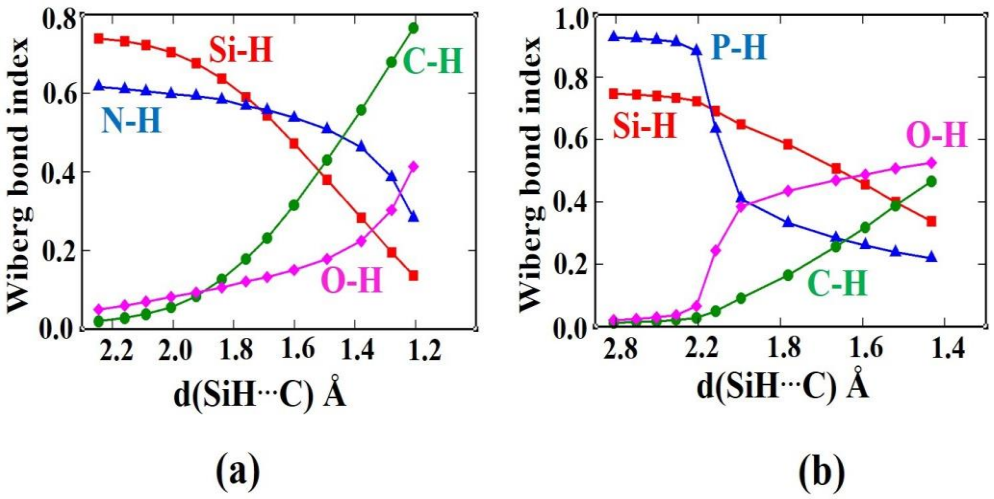

Figure 4.10: Evolution of Wiberg bond index values for the Si-H, D-H, C-H and O-H bonds for (a) **1-Si-N** and (b) **1-Si-P** along the pseudo-IRC path depicted as a function of the SiH...C distance for Me_2CO hydrogenation.

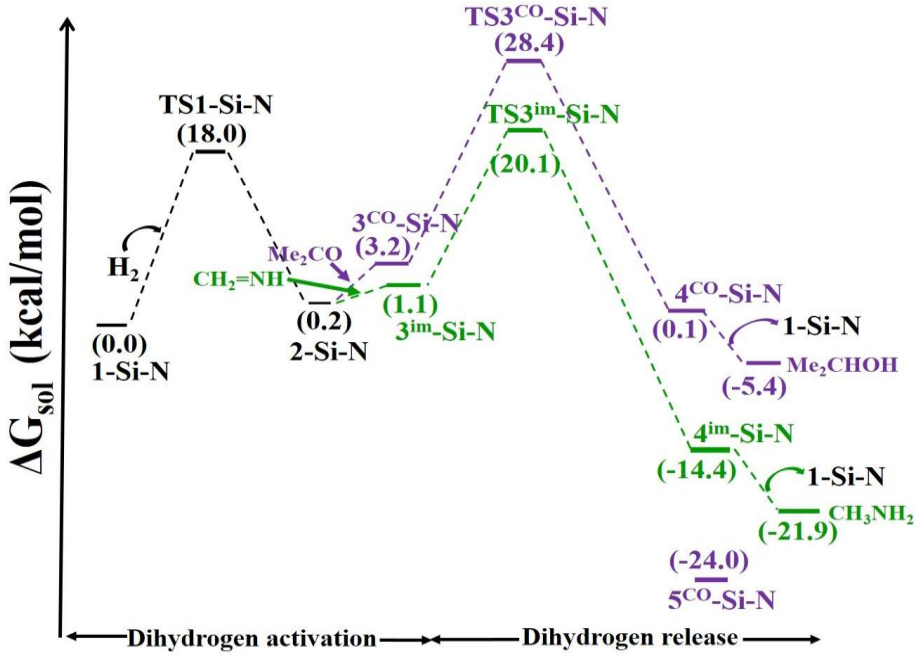

Figure 4.11: Relative Gibbs free energy profiles for catalytic hydrogenation of Me_2CO (violet line) and H_2CNH (green line) by **1-Si-N**. Solvent-corrected Gibbs free energy (kcal/mol) values are given in parenthesis.

kcal/mol in the energy profile for Me_2CO and H_2CNH respectively. Hydrogenation of Me_2CO and H_2CNH produce alcohol Me_2CHOH and amine CH_3NH_2 as a product, thermal dissociation of this complex restores the catalyst **1-Si-N** with the elimination of the hydrogenated product. However, in the case of Me_2CO, the alcohol bound complex $\mathbf{4^{CO}}$**-Si-N** can undergo a proton transfer process where the O-H bond of alcohol gets dissociated, and the proton gets attached to the nitrogen centre. As a result, similar to the CO_2 hydrogenation reaction, an alkoxide complex $\mathbf{5^{CO}}$**-Si-N** with a Si-O and an N-H bond is generated (see Figure 4.9) which block the active centres of the catalyst system.

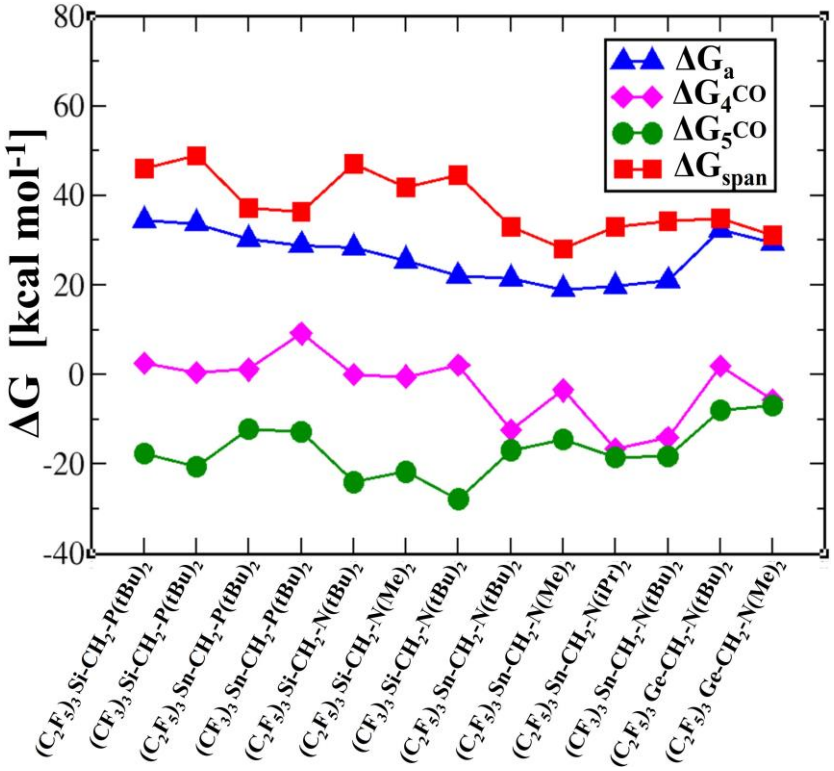

Figure 4.12: The computed values of Me_2CO hydrogenation barrier, Free energies of Me_2CO hydrogenation and the energy spans for all FLPs. All energies are given in kcal/mol.

Figure 4.12 shows that the DHR barriers of Me_2CO hydrogenation span quite a long-range from 19-34 kcal/mol among the different systems. Following the

similar behaviour as CO_2 hydrogenation, **Si/N** and **Sn/N** FLPs possess a lower DHR barrier among all the candidates. For a particular FLP system, Me_2CO hydrogenation has a higher value of **TS3** compared to the CO_2 hydrogenation reaction. Moreover, unlike CO_2 hydrogenation, the $\Delta G4^{CO}$ value for Me_2CO hydrogenation reaction largely varies. For most of the systems, the reaction is nearly reversible to moderately endergonic but particularly for **Sn/N** FLPs, the alcohol bound product $\mathbf{4^{CO}}$ lies quite downhill in the energy profile.

A closer inspection of the optimized geometries reveals shorter OH···N distance and therefore stronger H-bonding interactions for $\mathbf{4^{CO}}$**-Sn/N** systems which induce extra stabilization in these FLPs compared to others (Figure 4.13). Nonetheless, formation of the $\mathbf{5^{CO}}$ complex is quite exothermic for all the systems. According to ESM, $\mathbf{5^{CO}}$ constitute the TDI with $\mathbf{TS3^{CO}}$ is found to be the TDTS. Figure

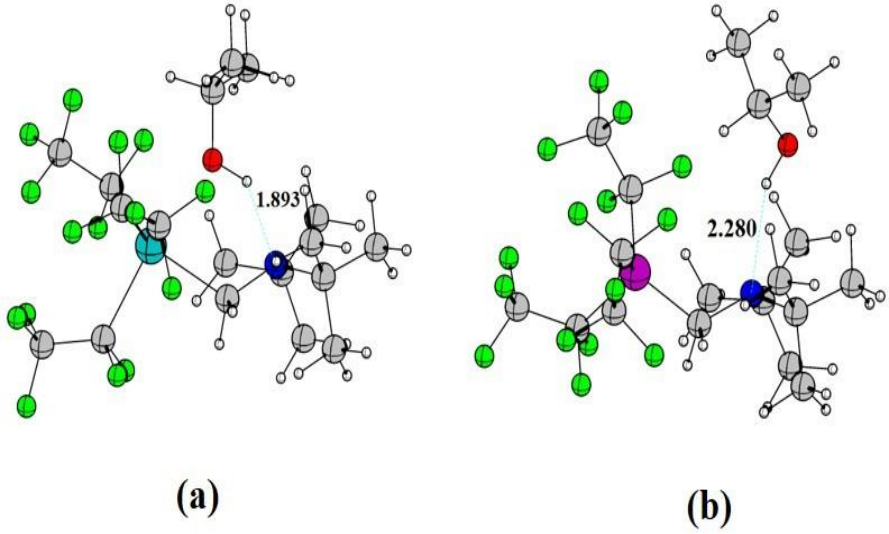

Figure 4.13: Geometry optimized structures of (a) $\mathbf{4^{CO}}$**-Sn-N** (b) $\mathbf{4^{CO}}$**-Si-N**.

4.12 indicates among all the systems, $(C_2F_5)_3Sn\text{-}CH_2\text{-}N(Me)_2$ and $(C_2F_5)_3Ge\text{-}CH_2\text{-}N(Me)_2$ have a lower energy span of 28.1kcal/mol and 29.6 kcal/mol respectively. For the rest of the catalyst systems, the computed free energy spans are

relatively higher and therefore an elevated reaction condition is required for Me_2CO hydrogenation by these FLP systems.

The IRC calculations along the reaction coordinate for imine hydrogenation reveal a slightly different mechanistic scenario. It is observed that for the FLPs with N, in the initial reactant complex **3^{im}** the imine is bound with the hydrogenated FLP in a parallel manner whereas for P containing FLPs it binds almost perpendicularly (Figure 4.14). This behaviour is reflected in their dihydrogen release profile which shows for N containing FLPs a simultaneous migration of hydride

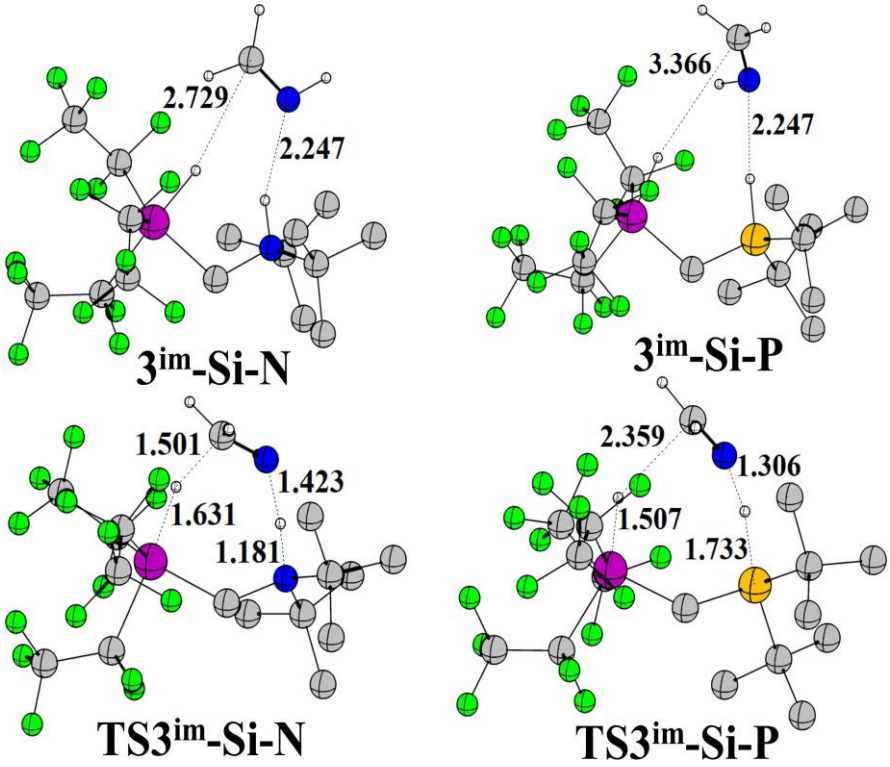

Figure 4.14: Geometry optimized structures of the intermediate(s)/TS involved in the DHR of **2-Si-N** to H_2CNH. All distances are given in Å. The hydrogen atoms attached to the carbon atoms of FLP are omitted for clarity.

and proton take place whereas, for FLPS with P centre, transfer of proton occurs at a much faster rate which activates the H_2CNH carbon toward the acceptance of the hydride (Figure 4.14). Nonetheless, these mechanistic differences

among the systems are not reflected in their DHR barriers. Figure 4.15 depicts that all these FLP systems have a very close value of **TS3^{im}** with an average of 20 kcal/mol. Interestingly it is found that two FLPs with similar structural

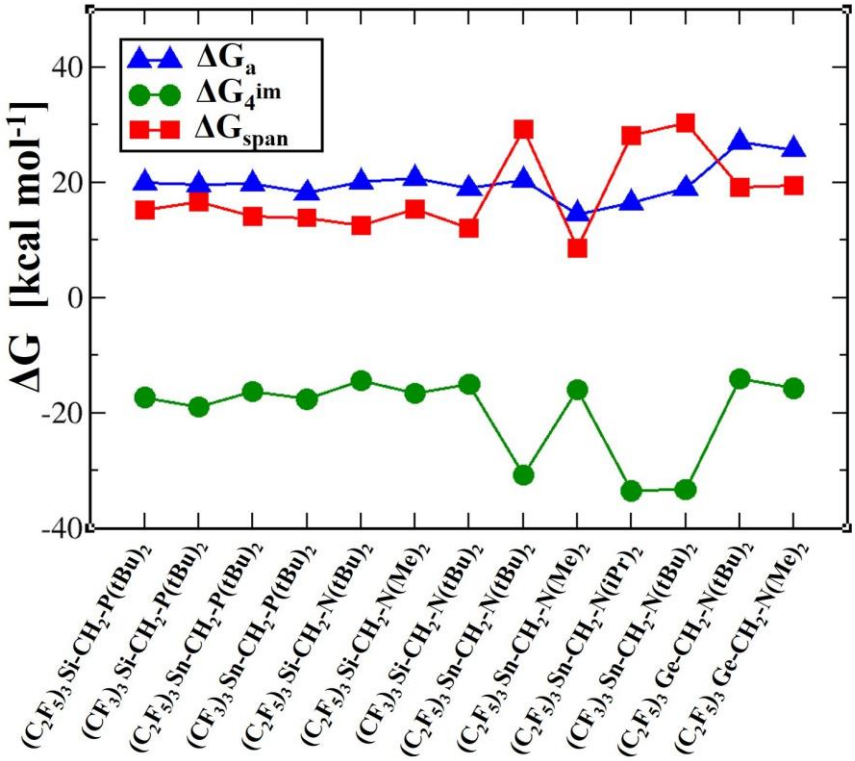

Figure 4.15: The computed values of H_2CNH hydrogenation barrier, Free energies of H_2CNH hydrogenation and the energy spans for all FLPs. All energies are given in kcal/mol.

frameworks but with different bases have very close imine hydrogenation barriers. For example, the **TS3^{im}** lies at 19.9 kcal/mol and 20.1 kcal/mol in the Gibbs free energy profile for **1-Si-N** and **1-Si-P** respectively. This is in contrast to our previous observations that show swapping the D centre can increase the DHR barrier significantly. To rationalize this observation activation strain analysis is performed along with the reaction coordinates with two representative systems **3^{im}-Si-P** and **3^{im}-Si-N** . The corresponding ASPs (Figure 4.16) unveils that at any point of the reaction coordinate **3^{im}-Si-P** has high strain energy as well as

interaction energy. However, the combined effect of large destabilizing ΔE_{strain} and a large stabilizing ΔE_{int} give rise to a moderate ΔE value for **3^{im}-Si-P** which is very close to the ΔE value obtained for **3^{im}-Si-P**. Unlike CO_2 and Me_2CO

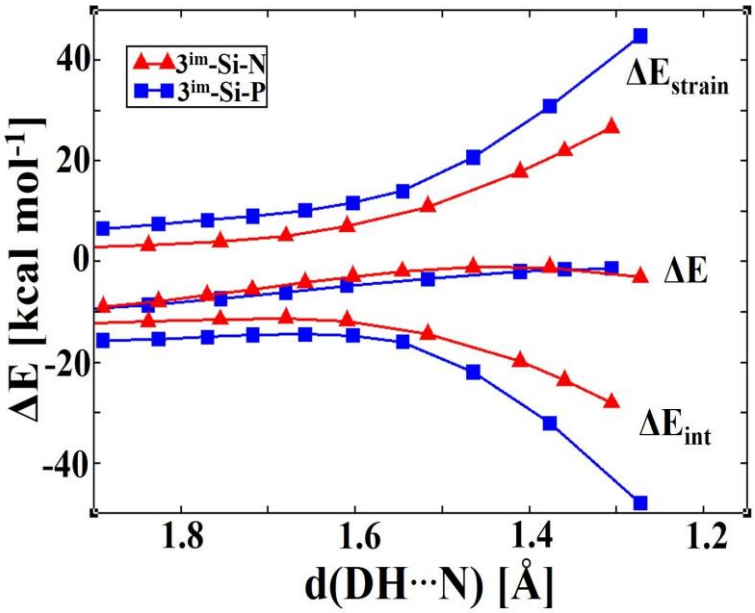

Figure 4.16: Activation-strain profiles for H_2CNH activation reaction by **3-Si-P** (blue) and **3-Si-N** (red) along the reaction coordinate depicted as a function of the DH...N distance.

hydrogenation, the H_2CNH hydrogenation product amine $MeNH_2$ does not involve a further proton exchange process with the D centre of the FLP. Nonetheless, the amine-bound species (**4^{im}**) lies quite downhill in the energy profile (Figure 4.15) and constitute the TDI of the catalytic cycle. Application of ESM indicates that for all the N bearing FLPs, the dihydrogen release step, **TS3^{im}** is the TDTS whereas for the P-containing FLPs the barrier for dihydrogen activation, **TS1** is found to be the TDTS of the imine hydrogenation cycle. Figure 4.15 imply that all these intramolecular FLPs have a very suitable energy span to perform the reaction at ambient conditions. Moreover, results indicate along with the FLPs with N donor, the P-containing FLP systems can also be potential catalysts for imine hydrogenation reaction.

4.3.3 Side reactions

One important point of investigating any catalytic cycle is to study the possible side reactions which can hamper the main reaction pathway. For the present case, such reactions are discussed in detail as follow

4.3.4 Propensity of dimer formation

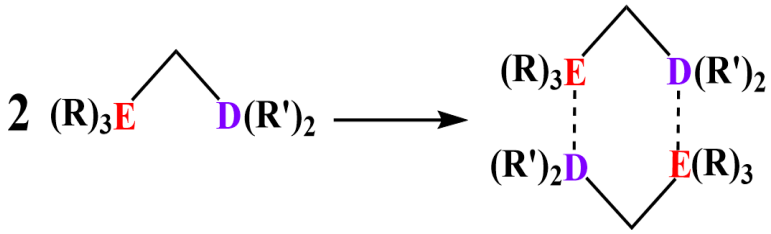

Figure 4.17: Schematic representation of dimer formation by **1**.

Since these intramolecular FLPs can undergo a dimer formation reaction (Figure 4.17) we have calculated the gibbs free energies of dimer formation (ΔG_{dimer}) for all the FLPs (Figure 4.18). We found that the computed values of (ΔG_{dimer}) are positive for all the candidates and therefore dimer formation is a thermodynamically unfavourable process for these geminal FLPs. So, we can conclude that dimer formation would not be an inhibiting side reaction for these geminal FLP systems.

1	ΔG_{dimer} (kcal/mol)
$(C_2F_5)_3Si\text{-}CH_2\text{-}P(tBu)_2$	9.3
$(CF_3)_3Si\text{-}CH_2\text{-}P(tBu)_2$	5.7
$(C_2F_5)_3Sn\text{-}CH_2\text{-}P(tBu)_2$	4.5
$(CF_3)_3Sn\text{-}CH_2\text{-}P(tBu)_2$	5.2
$(C_2F_5)_3\text{-}Si\text{-}CH_2\text{-}N(tBu)_2$	9.5
$(C_2F_5)_3Si\text{-}CH_2\text{-}N(Me)_2$	3.3
$(CF_3)_3Si\text{-}CH_2\text{-}N(tBu)_2$	5.5
$(C_2F_5)_3Sn\text{-}CH_2\text{-}N(tBu)_2$	2.0
$(C_2F_5)_3Sn\text{-}CH_2\text{-}N(Me)_2$	6.2
$(C_2F_5)_3Sn\text{-}CH_2\text{-}N(iPr)_2$	2.9
$(CF_3)_3Sn\text{-}CH_2\text{-}N(tBu)_2$	7.7
$(C_2F_5)_3Ge\text{-}CH_2\text{-}N(tBu)_2$	0.4
$(C_2F_5)_3Ge\text{-}CH_2\text{-}N(Me)_2$	3.6

Figure 4.18: Computed values of (ΔG_{dimer}) by **1**.

4.3.5 Reductive elimination decomposition pathway

In their study of H_2 activation by $(C_2F_5)_3Sn\text{-}CH_2\text{-}P(tBu)_2$ Mitzel and coworkers observed that following H-H bond cleavage, the corresponding product **2-Sn-P** undergoes a reductive elimination (RE) reaction which eventually leads to the removal of HC_2F_5 group with the formation of a phosphonium stannate(II) complex [15]. This reaction constitutes a deactivation pathway hindering the possible hydrogenation activity of **2-Sn-P** by releasing the proton and hydride to an unsaturated organic substrate. Thus, we investigated the mechanism of this relevant

deactivation pathway in detail (Figure 4.19). We find that the RE from **2** is an extreme manifestation of the ET involving σ^*(R-E) and σ(E-H) orbitals during H_2 activation. NBO analysis of **2** confirms a donor-acceptor interaction between these orbitals ($\sigma E^{(2)}$ = 143.9 kcal/mol, for **2-Sn-P**) weakening the corresponding R-E bond. The structure of the TS for the RE (**TS^{elm}**) features an elongated E-H bond (for **TS^{elm}**-Sn-P, E-H= 1.76 Å, Figure 4.19) as a result of the interaction between the carbon centre of the -R group with the σ^*(E-H) orbital. This leads to the gradual rupture of the Sn-H bond and H-R bond formation take place followed by the formation of **3** and elimination of **R-H**.

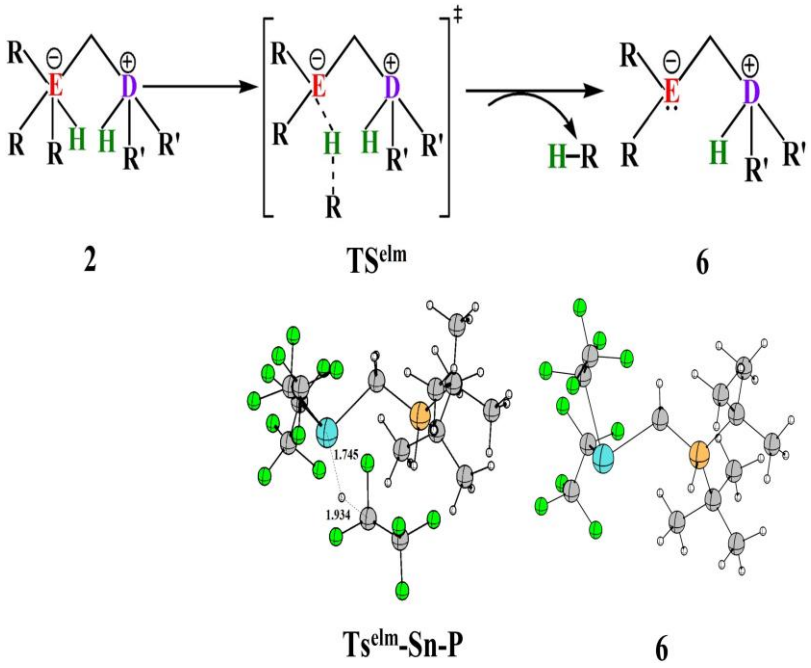

Figure 4.19: Schematic representation of reductive elimination reaction by **2** (top). Geometry optimized structures of the stationary points involved in the reaction by **1-Sn-P** (bottom). All distances are given in Å.

Since it can be a potential side reaction for these catalysts we examined this pathway in detail for all investigated FLPs. The computed Gibbs free energy profiles indicates this elimination reaction is exergonic in nature. Interestingly for

FLPs with Si LA, this decomposition pathway is moderately exergonic with ΔG_r ranging from -1.7 kcal/mol to -8.7 kcal/mol. For other candidates with Sn and Ge centres, this process is highly exothermic which may outweigh the catalytic hydrogenation process. However, all the systems have to cross a certain activation barrier (**TS3^{elm}**) for this elimination reaction and the computed barriers have

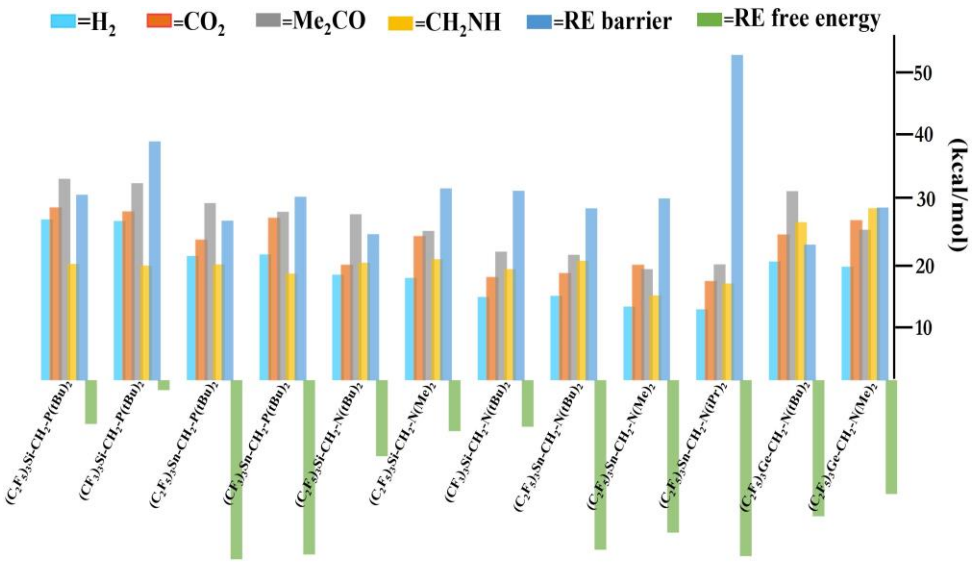

Figure 4.20: A comparison of the TS1 and (TS3^{XY}) values with the activation barrier (TS3^{elm}) and reaction gibbs free energy of reductive elimination for all FLPs. All energies are given in kcal/mol.

a wide range from 23-55 kcal/mol among the systems. We found for **1-Sn-P**, (**TS3^{elm}**) (27.3 kcal/mol) and the H_2 activation barrier **TS1** (21 kcal/mol) lies close in the free energy profile. This result can explain the experimentally observed RE for **1-Sn-P**. Similarly, Computed results reveal for $(C_2F_5)_3$Si-CH_2-P(tBu)$_2$, (C)2F$_5$)$_3$Ge-CH_2-N(tBu)$_2$ and $(C_2F_5)_3$Ge-CH_2-N(Me)$_2$, TS3^{elm} is comparable with **TS1** or **TS3^{XY}** which may hinder their expected catalytic performances whereas $(CF_3)_3$Si-CH_2-P(tBu)$_2$ and $(CF_3)_3$Sn-CH_2-P(tBu)$_2$ and particularly **Si/N** and **Sn/N** FLPs can activate dihydrogen and can release the activated dihydrogen

with a much lower activation barrier compared to RE process. Hence the **Si/N** and **Sn/N** geminal FLPs are predicted to be promising hydrogenation catalysts.

4.4 Conclusions

In this chapter, Recently a series of intramolecular FLPs $R_3E\text{-}CH_2\text{-}PR'_2$ (E= Si, Ge, Sn) featuring neutral E atoms as acceptor centres, were reported for activation of small molecules at ambient conditions. Additionally, they are able to perform heterolytic cleavage of dihydrogen molecule. In this work, we have explored their ability to act as hydrogenation catalysts. Our results show that the migration of activated dihydrogen from FLP towards unsaturated substrates like CO_2, carbonyl and imine occurs via a single concerted TS. However, this transfer process follows an asynchronous pathway which is governed by the donor/acceptor centre of the FLP as well as the nature of the unsaturated substrates like CO_2, carbonyl and imine occurs via a single concerted TS. However, this transfer process follows an asynchronous pathway which is governed by the donor/acceptor centre of the FLP as well as the nature of the unsaturated substrate. In the case of the electrophilic substrate like CO_2 and carbonyl, we observe an initial hydride transfer which is followed by a subsequent proton transfer. For imine hydrogenation, the sequence of this dihydrogen transfer process is controlled by the D centre of the FLP. For FLPs with N centre, a simultaneous migration of proton and hydride takes place while for P bearing FLPs, the initial release of proton-induced polarization of the C=N bond allows the subsequent hydride transfer. NBO analysis reveals that the two interactions $LP(Y)\rightarrow\sigma^*(D\text{-}H)$ and $\sigma(E\text{-}H)\rightarrow\pi^*(X{=}Y)$ dominates along the course of the reaction. Considering the overall free energy profiles these neutral geminal FLPs are predicted to be promising catalysts for imine hydrogenation whereas $(C_2F_5)_3Sn\text{-}CH_2\text{-}N(tBu)_2$ particularly can perform CO_2 hydrogenation at experimentally accessible conditions. Finally, possible side reactions such as dimerization

of the catalysts and reductive elimination decomposition reactions are investigated in detail. Results unveil that dimer formation is not a favourable process. Reductive elimination reaction can be a possible side reaction for some of the FLPs but nitrogen-containing FLPs and $(CF_3)_3Si\text{-}CH_2\text{-}P(tBu)_2$ and $(CF_3)_3Sn\text{-}CH_2\text{-}P(tBu)_2$ can surpass this decomposition reaction due to their lower dihydrogen release barrier and therefore can act as potential hydrogenation catalysts.

4.5 References

[1] Johnson, T. C.; Morris, D. J.; Willis, M., Hydrogen generation from formic acid and alcohols using ho-mogeneous catalysts. Chem. Soc. Rev. 2010, 39, 81-88.

[2] Merk, A.; Großekappenberg, H.; Schmidtmann, M.; Luecke, M-P.; Lorent, C.; Driess, M.; Oestreich, M.; Klare, H. F. T.; Mgller, T., Single-Electron Transfer Reactions in Frustrated and Conventional Silylium Ion/Phosphane Lewis Pairs. Angew. Chem. Int. Ed. 2018, 57, 15267 –15271.

[3] Liu, L. L.; Cao, L. L.; Shao, Y.; Menard, G.; Steph-an, D. W., A Radical Mechanismfor Frustrated Lewis Pair Reactivity. Chem 2017, 3, 259-267.

[4] Zhao, Y.; Truhlar, G. D., Theor. Chem. Account. 2008, 120, 215241.

[5] Zhao, Y.; Truhlar, G. D.Acc. Chem. Res. 2008, 41, 157167..

[6] Andrae, D.; Haeussermann, U.; Dolg, M.; Stoll, H.; Preuss, H.,Theor. Chem. Account. 1990, 77, 123-141.

[7] Grimme, S.; Antony, J.; Ehrlich, S.; Krieg, H.,J. chem. phys. 2010, 132, 154104-154119.

[8] Marenich, A. V.; Cramer, C. J.; Truhlar, D. G.,J. Phys. Chem. B. 2009, 113, 6378639. .

[9] Glendening, D. E.; Reed, A. E.; Carpenter, J. E.; Weinhold, F., NBO, version 3.1.; University of Wis-consin: Madison, WI, 1993

[10] Frisch, M. J. rucks, G. W.; Schlegel, H. B.; Scuseria, G. E.; Robb, M. A.;

Cheeseman, J. R.; Scalmani, G.; Barone, V.; Mennucci, B.; Petersson, G. A. et al. Gaussian 16, Revision A.03. 2016; Gaussian Inc. Wallingford CT..

[11] Diefenbach, A.; De Jong; Bickelhaupt, G. T., Molecular Physics. 2005, 103, 995–998.

[12] Bickelhaupt, F. M.; Houk, K. N., Angew. Chem. Int. Ed. 2017, 56, 10002–10002.

[13] 3. Zeist, V.; Bickelhaupt,W.J., , Organic biomolecular chemistry. 2010, 8, 3118–3127.

[14] Kozuch, S.; Shaik, A. S., Accounts of chemical research. 2011, 44, 101-110.

[15] Holtkamp, P.; Schwabedissen, J.; Neumann, B.; Stammler, H-G.; Koptyug, I. V.; Zhivonitko, V. V.; Mitzel, N. W., Chem. Eur.J. 2020, 26, 17381 –17385 .

5

On the Mechanism ofCopper hydride-Lewis Pair Cooperative Catalysis for CO_2 Hydrogenation

Work reported in this chpater is based on: Pallavi Sarkar, Shubhajit Das, Swapan K Pati (manuscript under preparation)

5.1 Introduction

From the enviromental perspective, hydrogenation of carbon dioxide is a very demanding field since the value added products generated from its reduction can act as promising alternative to fossil fuel [1-4]. Along that particularly formic acid or formate ion generation pathway is of of particular interest, as these are safer to transfer than hydrogen and contain a larger energy density [4,5]. Several transition metal catalysts like iridium, ruthenium, platinum and rhenium manganese, iron, cobalt, nickel and copper have susscessfuly performed the reaction with good yield [6-16]. However, toxicity and the cost associated with these heavy transition metals make this process less sustainable. Therefore the need to develop a CO_2 hydrogenation protocol using an environmentally benign main group catalyst is extremely desirable.

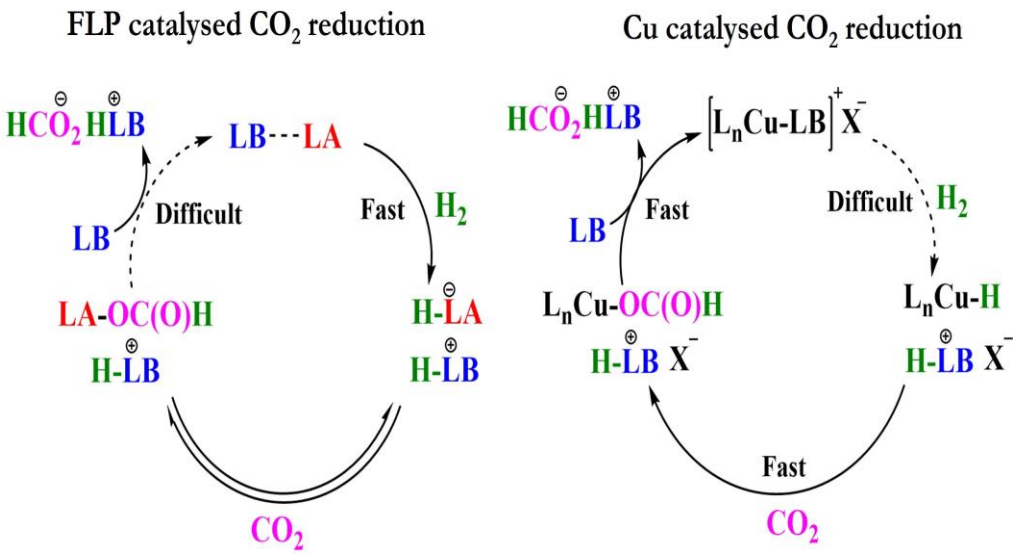

Figure 5.1: Limitation of a typical FLP catalysed CO_2 hydrogenation and a Copper catalysed CO_2 hydrogenation catalytic cycle.

Frustrated Lewis Pair (FLP) plays a significant role in this area [17-19]. The unquenched reactivity of the sterically precluded Lewis acid (LA) and Lewis base (LB) centres of FLPs has been utilised to split the H-H bond and H_2 activation

becomes a hallmark of FLP chemistry. Not only the splitting of the H_2 bond, but FLP can also successfully transfer the proton and hydride to some unsaturated substrates like CO_2, carbonyl, imines, alkane, alkynes and many more. Thus it develops a metal-free catalytic hydrogenation protocol.

However, as we discussed in the previous chapter, the main problem for the FLP-mediated CO_2 or carbonyl hydrogenation lies in the formation of a very stable LA-O bond in the alkoxide complex which makes the process energy-demanding and therefore prevents the process from being catalytically active (Figure 5.1). Recently Bertrand *et al.* designed a unique approach where a transition metal hydride has been reported to work in tandem with a Lewis pair. In this hybrid approach, CO_2 has been activated by a monomeric copper hydride complex supported by cyclic(alkyl)(amino) carbene (CAAC) ligand [20]. It is already known that copper hydride has been widely utilized as an efficient catalyst for several carboxylation reactions [21-22]. As depicted in Figure 5.2 CO_2 insertion in the C-H bond of (CAAC)CuH leads to a copper formate complex (CAAC)CuOCOH.

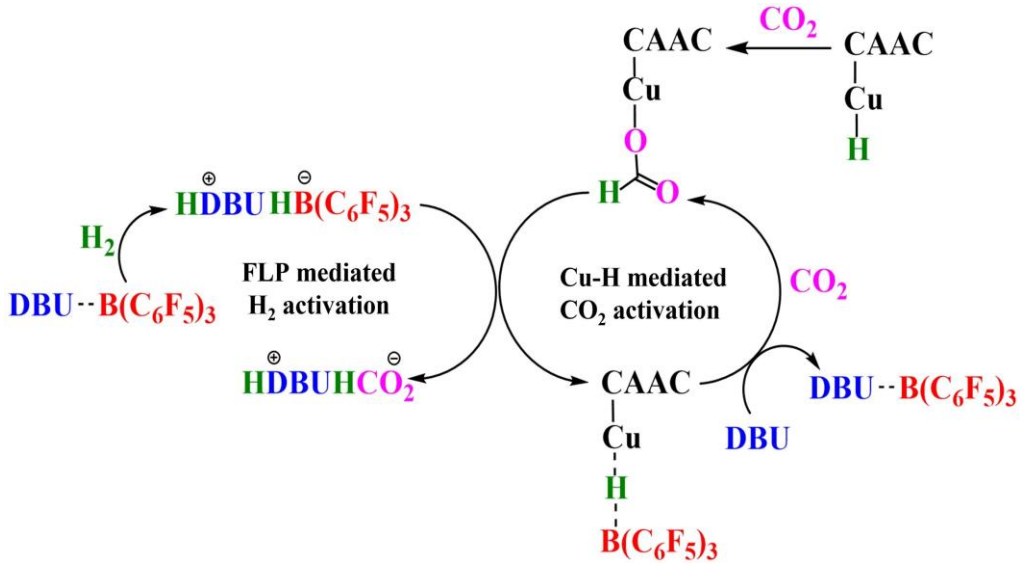

Figure 5.2: Possible reaction route for the copper-hydride/Lewis pair catalysed hydrogenation of carbon dioxide.

In this way, formation of the LA-O complex is avoided. However, the metal has difficulties activating H_2. To solve this problem a Lewis pair (LP) has been employed, which can easily split the H-H bond. The resulting zwitterion $[LAH]^-[LBH]^+$ interacts with copper formate (CAAC)CuOCOH which leads to the regeneration of copper hydride (CAAC)CuHLA species with the release of formate salt $[LBH]^+[HCO_2]^-$. This synergistic action between the copper hydride and the LP leads to superior catalytic performance (TON = 1881 for 24 h) with a low catalyst loading of only 0.025%. Thus it significantly outperforms both the independent Cu(I) and FLP systems. However, apart from these interestings findings there are some points that need further attention, like (1) the underlying mechanistic picture for the cooperative interaction between the copper and LP. (2) the mechanism of dihydrogen activation by BCF/DBU LP is quite ambiguous as the formation of $[HBCF]^-[HDBU]^+$ ion pair is not observed. At the same time, (3) the reason for the inefficiency of the PMP/BCF FLP towards the catalytic turnover remains to be realized. This has prompted us to perform a detailed computational study to elucidate the mechanistic picture of the Copper hydride/LP mediated carbon dioxide hydrogenation.

5.2 Computational details

All the electronic structure calculations are performed using M06 functional under the framework of Density Functional Theory. For lighter atoms (C, H, N, B, O, F) we have considered the def2svf basis set while for Cu def2TZVP along with Stuttgart-Dresden effective core potential. This basis set combination is here-after denoted as BS-I. Harmonic vibrational frequency analysis is performed to characterize the structures to be minima (no imaginary frequency) or transition states (one imaginary frequency). Transition states are further verified by in-trinsic reaction coordinate (IRC) calculations to confirm their connection to two respective minimum structures. Based on M06/BS-I optimized geometries, the electronic energies are further refined with single-point energy calculations at the M06/def2TZVP level of theory. All the thermochemical data are obtained with the ideal gas-rigid rotor-simple harmonic oscillator approximations at 298.15 K and 1 atm. Zero point-energy corrections are included in the Gibbs free energy values along with a concentration correction for c = 1 mol/ dm^3 condition in the solvent. We have used THF as a solvent to estimate the relative stabilities of the reaction intermediates / transition state (TS) involved in the reaction. The SMD solvation model is used to account for the solvent effects [24]. All calculations are performed using the Gaussian 16 suite of programs [25]. Note that, we have used the following atom colouring to visualize the molecular geomteris: C (grey), H (white), N (blue), O (red), F (fluorescent green), B (pink), Cu (yellow).

5.3 Results and discussion

Catalytic CO_2 hydrogenation constitutes of three steps which are discussed as follow-

5.3.1 Activation of CO_2 by Copper hydride

First, CO_2 is inserted in the Cu-H bond of LCuH (**A1**), where L=CAAC, resulting in a formate complex LCuOCHO (**B1**). The activation barrier of this process is 17.1 kcal/mol with an associated free energy change of -5.0 kcal/mol.

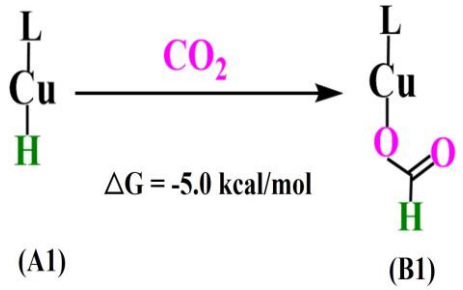

Figure 5.3: CO_2 activation by Copper-hydride complex.

5.3.2 Activation of H_2 by FLP

The Next task is to split the H-H bond. For this Bertrand *et al.* first employed the 1,2,2,6,6-pentamethylpiperidine (PMP) and tris(pentafluorophenyl)borane (BCF) as Lewis base (LB) and Lewis acid (LA) respectively. Therefore, at first, we have also examined the H_2 activation reaction by the PMP/BCF pair. In agreement with the experimental results, our computed energy profile (Figure 5.4) also suggests this FLP combination can successfully break the H-H bond resulting in $[PMPH]^+[HBCF]^-$ (**1**) zwitterion.

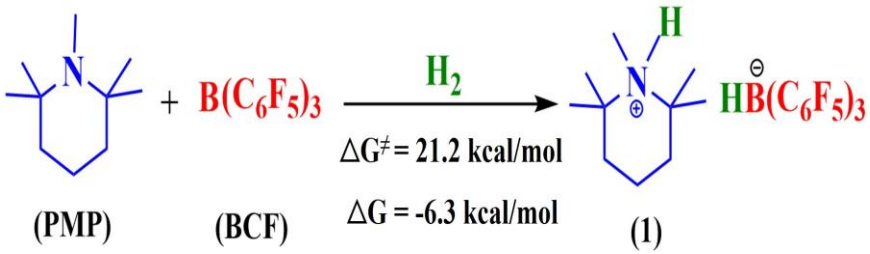

Figure 5.4: H_2 activation by PMP/BCF FLP.

5.3.3 Regeneration of Cu-H using H-BCF

Following that, zwitterion **1** reacts with **B1**. It forms the formate salts (**2**) and the Cu-H bond (**C1**) is regenerated (Figure 5.5).

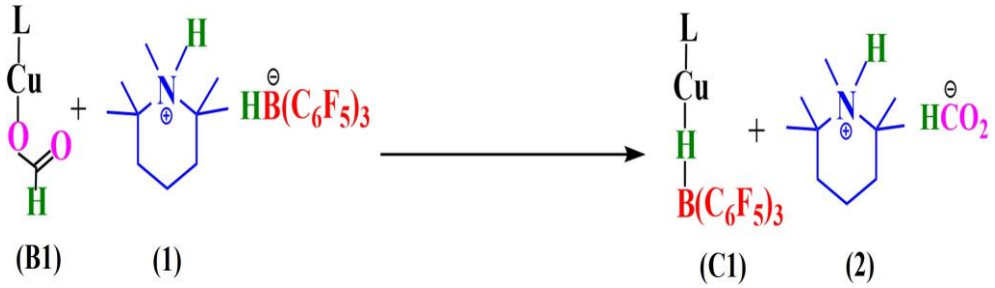

Figure 5.5: Reaction of **1** with **B1** resulting in the formation of **C1**

However, it is observed that under catalytic condition BCF/PMP FLP fails to give the turnover. Conversely, the less sterically hindered bases like Lutidine, Triazabicyclodecene (TBD) or 1,8-Diazabicyclo(5.4.0)undec-7-ene (DBU) successfully perform the catalytic reaction. Particularly DBU produces an excellent yield when paired with BCF. This result seems quite surprising since an FLP that performs stoichiometric H_2 activation fails under catalytic conditions whereas a classical Lewis pair like DBU/BCF succeed. The question remains unanswered. Therefore we next focus on the DBU/BCF mediated H_2 activation.

5.3.4 Activation of H_2 by DBU/BCF

The addition of DBU with BCF leads to the formation of a Lewis pair **3**. The optimized geometry of **3** (Figure 5.6) shows a small distance of 1.634 Å between N and B which is in excellent agreement with the experimentally obtained bond distance of 1.61 Å [20]. Figure 5.6 also depicts that the formation of **3** is a highly exergonic process. Moreover, the transition state (**TS3**) for H_2 activation by **3** lies at 18.9 kcal/mol in the energy profile. Therefore the computed energy span

for this reaction becomes 34.0 kcal/mol.

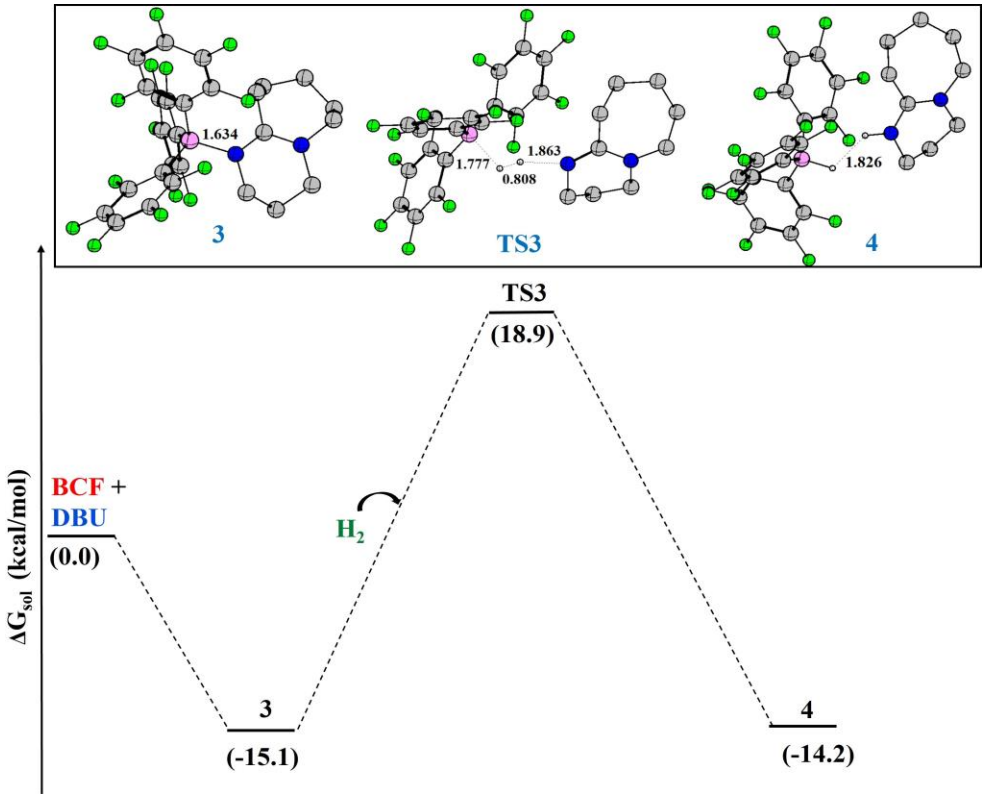

Figure 5.6: The relative gibbs free energy profile for the H_2 activation by DBU/BCF pair.The upper panel shows the geometry optimized structures of the intermediate(s)/TS involved in this process.

This high energy span makes the H_2 splitting by DBU/BCF pair quite unfeasible. This result is also in line with the experimental observation that even after the application of 10 bar of H_2 at the dichloromethane solution of BCF and DBU, the H_2 cleaved product $[DBUH]^+[HBCF]^-$ **4** is not observed [20]. However, when a mixture of the copper formate **B1** and the Lewis pair **4** was subjected to 20 bar of H_2 at 80°c in THF, clear formation of copper hydride borane and HDBU formate salt is observed [20]. The possible explanation given by Bertrand and coworkers is that both **3** and **4** are in equilibrium and the formation of **4** is endergonic which prevents its observation. Although the computed energy profile as shown in Figure 5.6 agrees well with the equilibrium condition of the **3** and the Zwitterionic

product **4**, it clearly shows that the formation of H_2 activated product **4** is highly exergonic. Thus it opens the question that how the BCF/DBU pair activate the H_2 molecule or does it actually split the H-H bond?

5.3.5 Alternative Lewis pair in the system: H_2 activation by THF/BCF Lewis pair

Meanwhile, we observed that in addition to DBU, BCF can also react with another base THF which is present as a solvent in the system. The interaction of BCF with THF forms complex **5** where the distance between the oxygen and the boron centre is 1.623 Å. It is interesting to note that this Lewis pair (LP) can

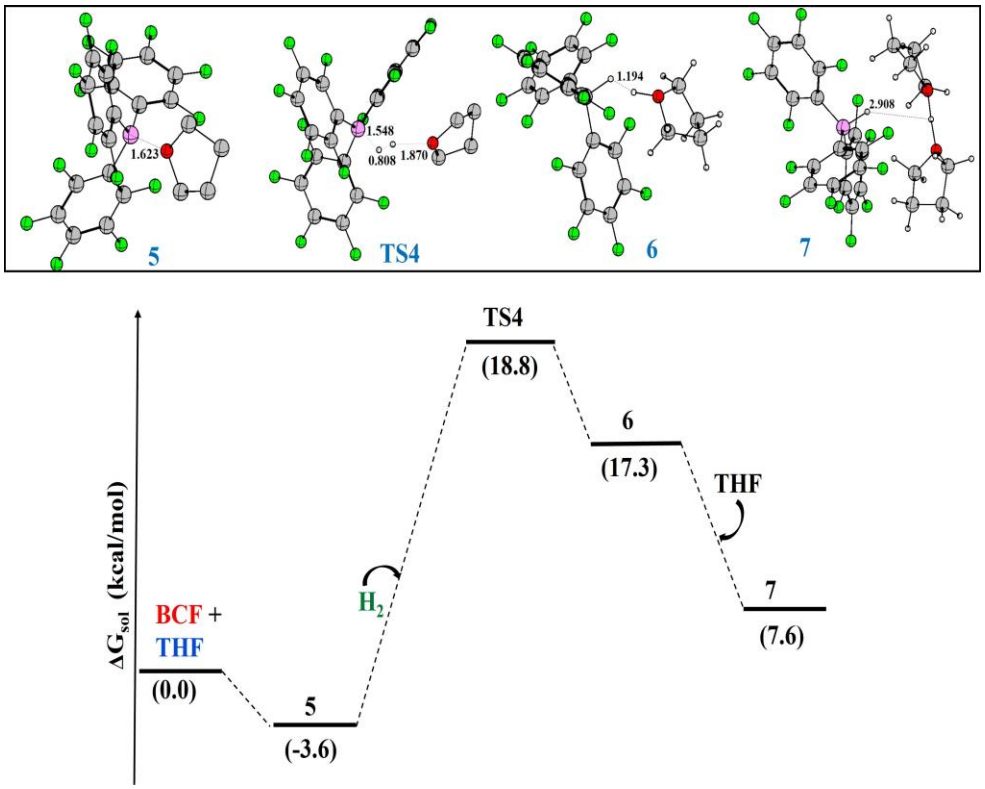

Figure 5.7: The relative gibbs free energy profile for the H_2 activation by THF/BCF pair.The upper panel shows the geometry optimized structures of the intermediate(s)/TS involved in this process.

also break the H-H bond and the energy required for this process is very close (18.6 kcal/mol, Figure 5.7) to the value associated with the DBU-BCF pathway (18.9 kcal/mol, Figure 5.6). Nonetheless, unlike DBU, the formation of the THF-BCF complex (**5**) is exergonic by only 3.7 kcal/mol. Consequently, the overall energetic span of the process is much lower (22.0 kcal/mol) and thus the H_2 molecule can be easily cleaved by the THF-BCF LP system.

5.3.6 Activation of H_2 by L-Cu-(DBU)$^+$

Recently Appel and coworkers studied a very similar triphosphine-ligated Cu(I) complex which successfully hydrogenates CO_2 in presence of a base [15]. In their computational study, they have shown that the base DBU replaces the formate from LCuOCOH and forms LCu(DBU)$^+$ which acts as the resting state of the catalyst during the reaction. Moreover, this LCu(DBU)$^+$ complex is actually responsible for the H_2 activation in an FLP-like manner [26]. Therefore we have also investigated a similar pathway for **B1**. Figure 5.8 depicts that initially DBU replace the formate from **B1** and forms the **LCu(DBU)**$^+$ complex, which is 4.6 kcal/mol higher in energy from the reference point. This complex interacts with H_2 and eventually passes a transition state **TS5** and forms the H_2-activated product **[LCuH][HDBU]**$^+$. The optimized geometry of **TS5** reveals an elongated H-H bond length of 0.904 Å with one H atom interacting with the Cu centre whereas the other H atom points towards the N centre of DBU. However, this process is associated with a high activation barrier (32.0 kcal/mol). Thus the possibility of H_2 activation by the **LCu(DBU)**$^+$ can be ruled out in this case. Hence from the above discussions we can conclude that among all the possible pathways of H_2 activation, BCF/THF LP can perform the reaction with a lower activation barrier compared to others.

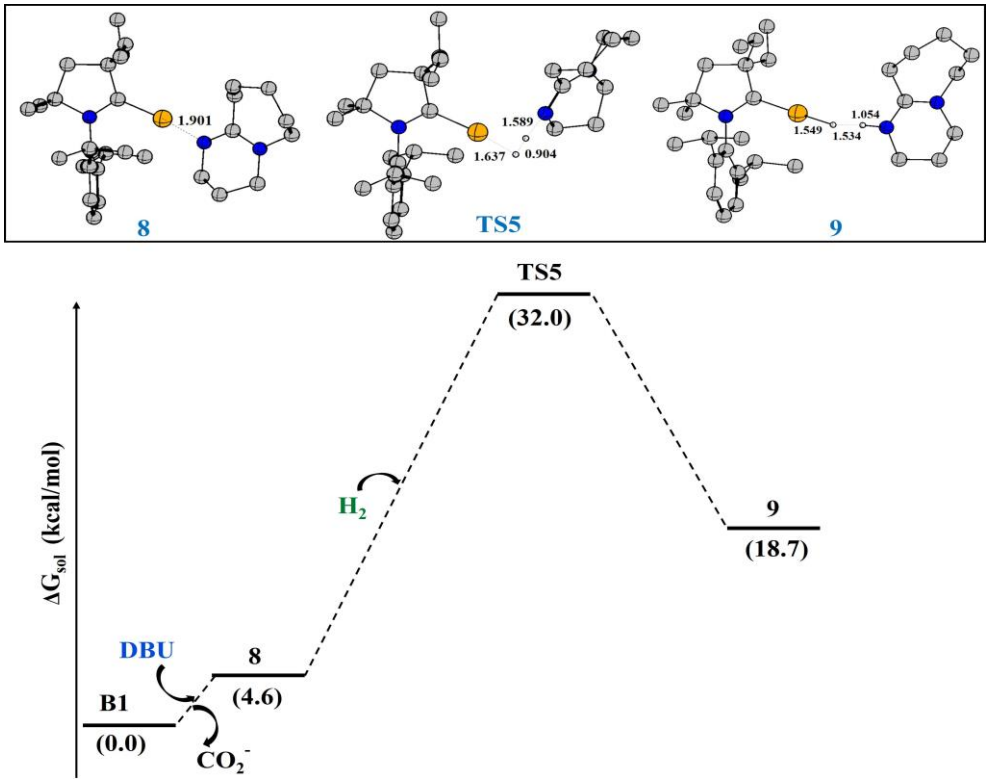

Figure 5.8: The relative gibbs free energy profile for the H_2 activation by **LCu(DBU)**$^+$ .The upper panel shows the geometry optimized structures of the intermediate(s)/TS involved in this process.

5.3.7 Regeneration of Cooper hydride

After successful hydrogen activation, the next step is to release the formate from **B1** and regenerate the copper hydride catalyst. A plausible mechanism for this process is depicted in Figure 5.9. The zwitterion $[THFH]^+[HBCF]^-$, results from the H_2 activation by THF/BCF, reacts with **B1** and the proton is transferred from THF to the carbonyl oxygen of formate. As a result, the Cu-O bond gets elongated. The free energy associated with this process is -5.2 kcal/mol. The base DBU present in the reaction mixture then takes up the proton from LCuOOH and form the $[DBUH]^+[HBCF]^-$ ion pair. The high basicity of DBU makes this step exothermic in nature (-21.7 kcal/mol). This $[DBUH]^+$ then form the formate

salt $[DBUH]^+[HCO_2]^-$ and the copper hydride borane adduct LCuHBCF complex (**C1**) is produced.

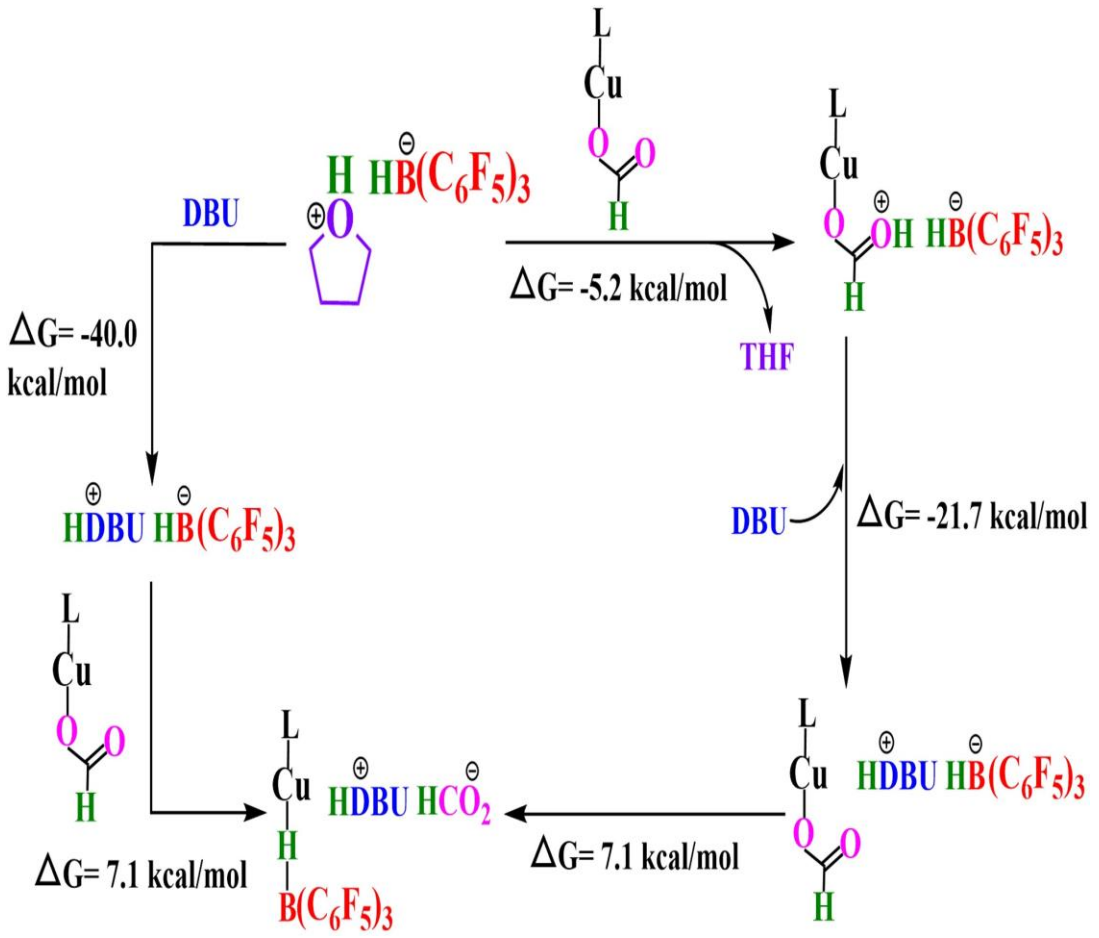

Figure 5.9: Proposed catalytic cycle for the regeneration of Copper-hydride.

On the other hand, an alternative pathway is also possible where the $[THFH]^+[HBCF]^-$ ion pair at first reacts with DBU itself. Due to the high basicity of DBU, it easily takes up the proton from $THFH^+$ (ΔG_R = -44.0 kcal/mol) and $[DBUH]^+[HBCF]^-$ ion pair is formed. Thus it can be said that the solvent THF plays a noninnocent role in this catalytic reaction. It participates actively in the H_2 activation and it acts as a proton shuttle to transfer the proton to DBU.

5.3.8 Next catalytic cycle

After this the **C1** complex should further enter into the next catalytic cycle. It is experimentally observed that the reaction of **C1** with 20 bar of CO_2 at 100°C in the presence of DBU forms the copper formate **B1** along with the Lewis pair **3**.

L-Cu-H-BCF (C1)+CO_2+DBU =L-Cu-HCOO(B1)+BCF-DBU(3)

This is also in agreement with the computed free energy change ΔG_R = -0.5 kcal/mol of the reaction.

Note that for a similar reaction catalyzed by PMP the free energy change is highly endergonic, ΔG_R = 25.4 kcal/mol. This clearly explained the inefficiency of the BCF-PMP FLP for the catalytic turnover is due to their weak binding. Thus the weak base PMP fails to replace the BCF from **C1**.

L-Cu-H-BCF (C1)+CO_2+PMP =L-Cu-HCOO(B1)+BCF-PMP

Therefore this crucial reaction of the catalytic cycle, the generation of **B1** from **C1** needs further attention. Apart from its thermodynamics, it is important to study the associated kinetics of the different steps like the addition of CO_2 and replacement of BCF by DBU to form the ion-pair **3**. The plausible pathways for this reaction are shown in Figure 5.10.

Pathway-1 involves the release of BCF from **C1** and generates **LCuH**. This **LCuH** can reacts with CO_2 to form **B1** and BCF reacts with DBU to form **3**. However, the computed free energy change (19.6 kcal/mol) for the first step of this process ruled out this possibility.

L-Cu-H-BCF = L-Cu-H + BCF, ΔG_R=19.6 kcal/mol

L-Cu-H+CO_2 = L-Cu-HCOO, ΔG_a=17.1 kcal/mol, ΔG_R=-5.0 kcal/mol

BCF + DBU = BCF-DBU (3), ΔG_R=-15.1 kcal/mol

This result shows the presence of a strong interaction between the hydride and BCF in **C1**. Therefore a possible way (pathway-2) may be the release of $HBCF^-$ from **C1** which can activate CO_2 and the resulting HCO_2^- species binds with

[L-Cu]$^+$.

L-Cu-H-BCF = L-Cu$^+$ + [H-BCF]$^-$, ΔG_R=11.4 kcal/mol

[H-BCF]$^-$ + CO$_2$ + DBU = BCF-DBU + HCOO$^-$

L-Cu$^+$ + HCOO$^-$ = L-Cu-HCOO, ΔG_R = -33.3 kcal/mol

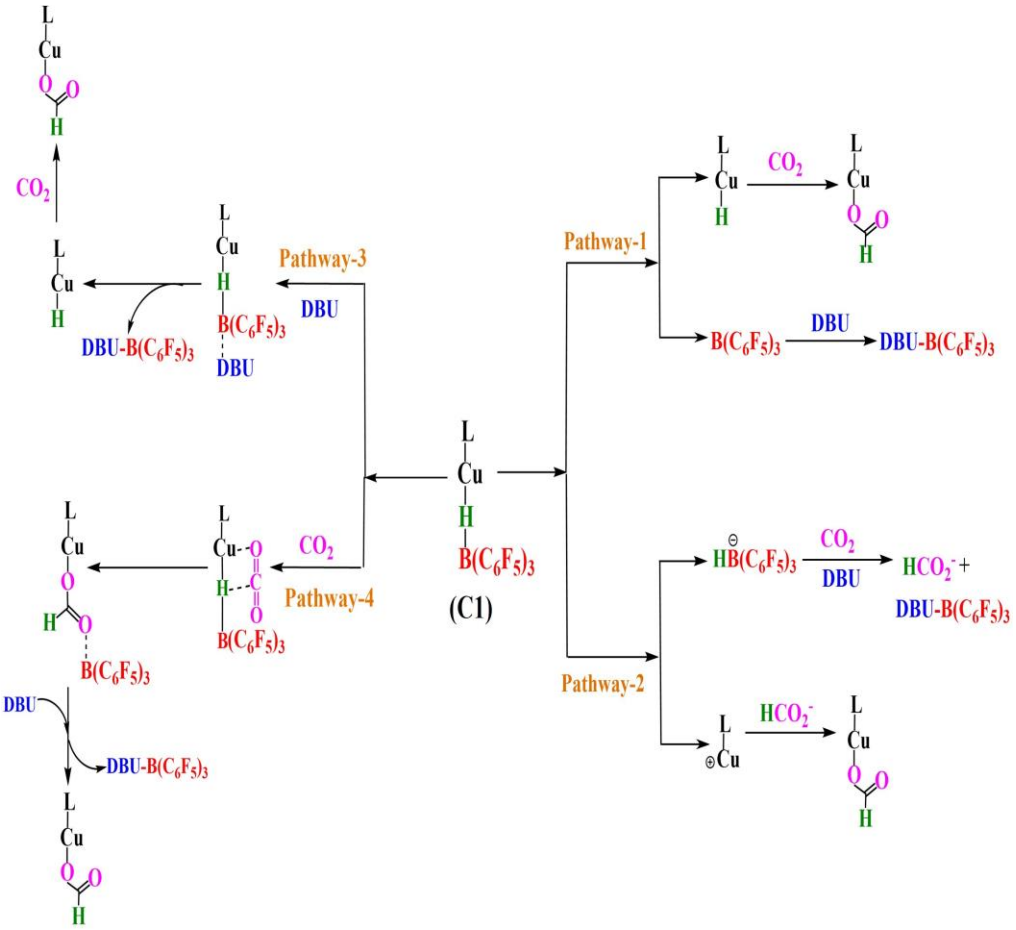

Figure 5.10: The plausible reaction pathways for the conversion of **C1** to **B1**.

Our results show that although the first step of pathway-2 is less endergonic than that of pathway-1, however, it is difficult for BCF alone to transfer the hydride to CO_2.

Thus an alternative pathway is also proposed (pathway-3) where the DBU interacts with **C1** and is released as DBU-BCF (**3**) complex. This pathway is

associated with an activation barrier of 44.1 kcal/mol (Figure 5.11). The resulting L-Cu-H (**A1**) species further activates CO_2 and generates the **B1** complex.

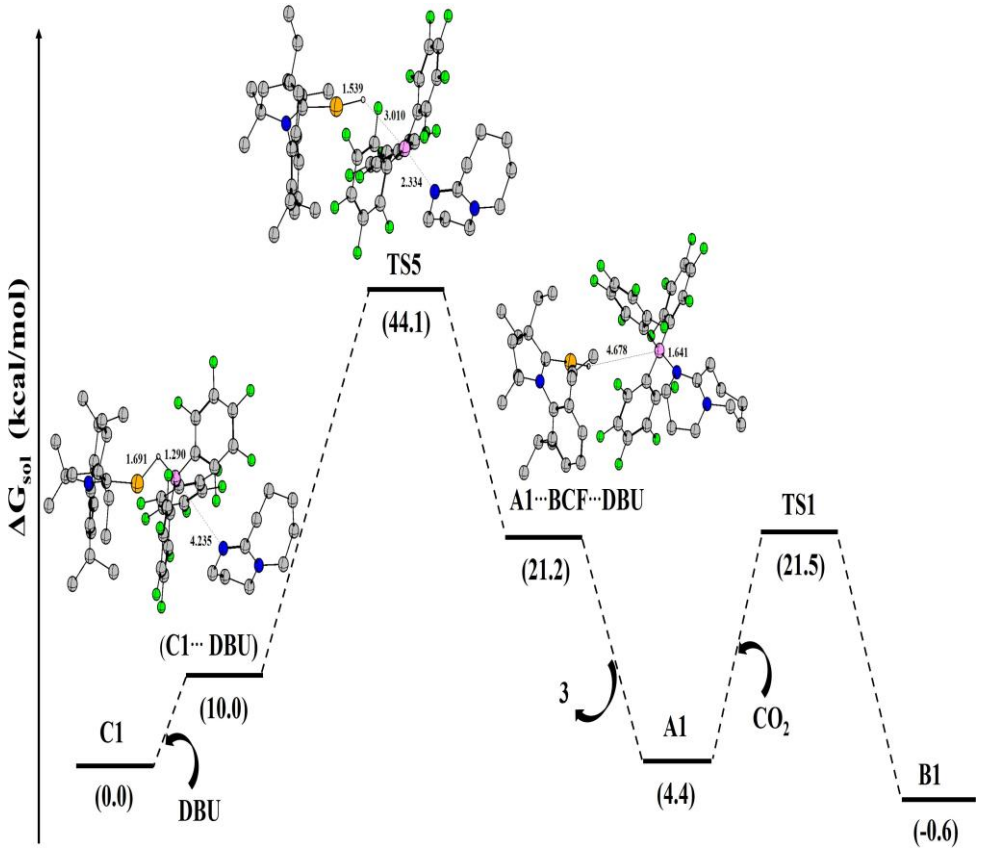

Figure 5.11: The gibbs free energy profile for the conversion of **C1** to **B1** according to pathway-3.

Similarly, another pathway is possible (pathway-4) where initially a CO_2 bound complex **C1. . . CO$_2$** is formed which is only 3.1 kcal/mol higher in energy than **C1**. This complex passes through **TS6** where a hydride transfer takes place from the Cu centre to the carbon atom of CO_2 (Figure 5.12). The activation barrier to this process is 44.3 kcal/mol. As a result, the Copper-formate complex (**B1. . . BCF**) is generated (Figure 5.12). The optimized geometry of **B1. . . BCF** complex reveals an interaction between one oxygen atom of CO_2 with the boron centre of BCF, which is reflected by a close distance of 1.563 Å. As a result of this stabilizing

interaction the **B1. . . BCF** complex lies at 3.7 kcal/mol in the energy profile. This is further reflected in the high reaction barrier of the next step (**TS7**) where DBU enters into the reaction and displaces the BCF with concomitant formation of **3** and **B1**.

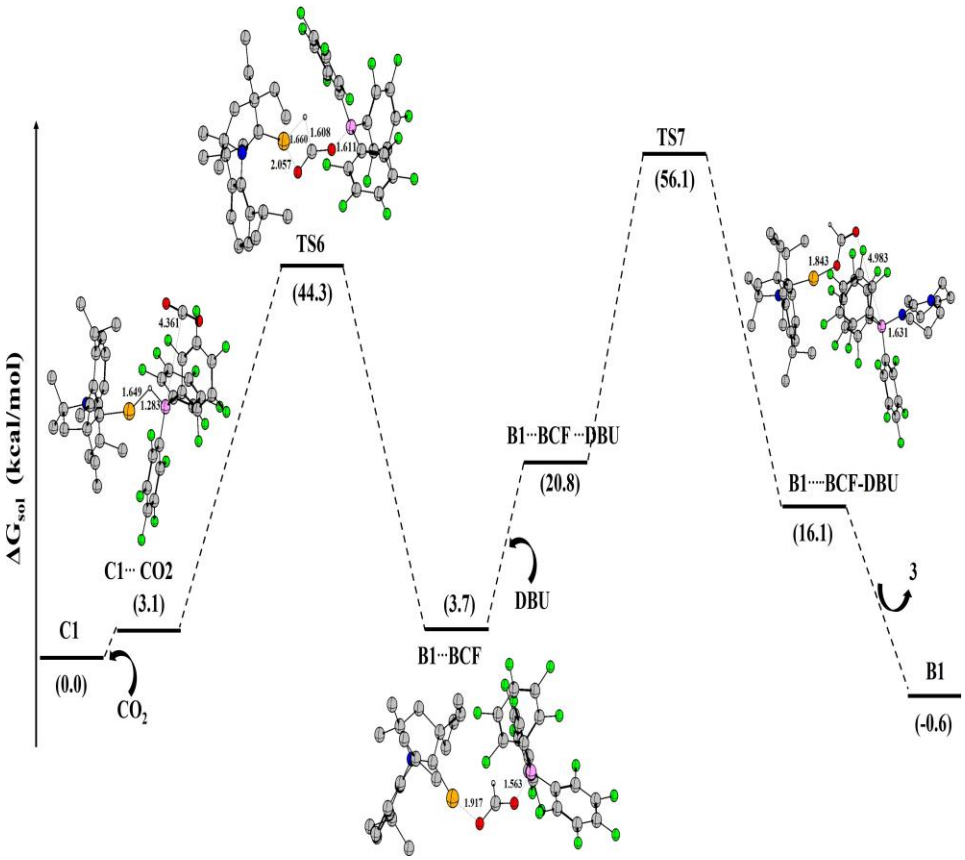

Figure 5.12: The gibbs free energy profile for the conversion of **C1** to **B1** according to pathway-4.

Therefore the above discussions indicate that among all the possible pathways, pathway 3 exhibits the most feasible energy profile. Thus the base DBU plays an important role in the conversion of **C1** to **B1** species by displacing the BCF which makes the copper-hydride centre available for the reaction with the next CO_2 molecule.

5.4 Conclusions

In summary, we have elucidated the mechanism of cooperative interaction between Cu-H and Lewis pair catalysts during CO_2 reduction reaction. We have also explored the H_2 activation pathways by all possible Lewis pairs as well as copper-DBU complex. Computed results show that solvent tetrahydrofuran plays a noninnocent role which actually activates dihydrogen and transfers the activated proton to base DBU. The protonated DBU then forms the formate salt by replacing the formate group from the copper formate species. The regenerated copper hydride can resume the next catalytic cycle. Additionally, we also studied this CO_2 hydrogenation cycle in presence of PMP Lewis base and it is found that the inefficiency of PMP-BCF FLP towards catalytic turnover is related to weak basicity of PMP.

5.5 References

[1] Olah, G. A.; Prakash, G. K. S.; Goeppert, A. J. Am. Chem. Soc. 2011 , 133 , 12881 12898.

[2] Aresta, M.; Dibenedetto, A.; Angelini, A . Chem. Rev. 2014 , 114 , 1709 1742.

[3] Cokoja, M.; Bruckmeier, C.; Rieger, B.; Herrmann, W. A.; Kuhn, F. E Angew. Chem., Int. Ed. 2011, 50 , 8510-8537 .

[4] Leitner, W. Angew. Chem., Int. Ed. 1995 , 34 , 2207 2221.

[5] Enthaler, S.; von Langermann, J.; Schmidt, T. Energy Environ. Sci. 2010 , 3 , 1207 1217.

[6] Inoue, Y., Izumida, H. Hashimoto, H. Chem. Lett. 5, 863–864 (1976).

[7] Dong, K., Razzaq, R., Hu, Y. Ding, K. Top. Curr. Chem. 375, 1–26 (2017).

[8] Tanaka, R., Yamashita, M. Nozaki, K. J. Am. Chem. Soc. 131, 14168–14169 (2009).

[9] Bertini, F. et al. Chem. Sci. 8, 5024–5029 (2017).

[10] Langer, R. et al. Angew. Chem. Int. Ed. 50, 9948–9952 (2011).

[11] Zhang, Y. et al. Chem. Sci. 6, 4291–4299 (2015).

[12] Jeletic, M. S., Mock, M. T., Appel, A. M. Linehan, J. C. A J. Am. Chem. Soc. 135, 11533–11536 (2013).

[13] Vogt, C. et al. Nat. Catal. 1, 127–134 (2018).

[14] Watari, R., Kayaki, Y., Hirano, S.-I., Matsumoto, N. Ikariya, T. Adv. Synth. Catal. 357, 1369–1373 (2015).

[15] Zall, C. M., Linehan, J. C. Appel, A. M. ACS Catal. 5, 5301–5305 (2015).

[16] Zall, C. M., Linehan, J. C. Appel, A. M. J. Am. Chem. Soc. 138, 9968–9977 (2016).

[17] G. C. Welch, R. R. S. Juan, J. D. Masuda, D. W. Stephan, Science 2006, 314, 1124–1126.

[18] P. A. Chase, G. C. Welch, T. Jurca, D. W. Stephan, Angew. Chem. Int. Ed. 2007, 46, 8050–8053.

[19] G. C. Welch, D. W. Stephan, J. Am. Chem. Soc. 2007, 129, 1880–1881.

[20] Romero, E.A., Zhao, T., Nakano, R. et al. Nat. Catal. 2018, 743–747.

[21] Wang, S., Du, G. Xi, C. Org. Biomol. Chem. 2016, 14, 3666–3676.

[22] Liu, Q., Wu, L., Jackstell, R. Beller, M. Nat. Comm. 2015, 6, 5933.

[23] Zhao, Y.; D. G. Theoretical Chemistry Accounts: Theory, Computation and Modeling (Theoretica Chimica Acta) 2008, 120, 215-241.

[24] Marenich, A. V.; Cramer, C. J.; Truhlar, D. G. J. Phys. Chem. B 2009, 113, 63786396.

[25] Frisch, M. J. et al. Gaussian 16 Revision A.03. 2016; Gaussian Inc. Wallingford CT.

[26] Persaud, R. R.; Fang, Z.; Zall, C. M.; Appel, A. M. Dixon, D. A. J. Phys. Chem. A 2021, 125, 30, 6600–6610.

6

Reductive Functionalization of CO_2 for Methylation of Amide

Work reported in this chpater is based on: Arpan Das, Pallavi Sarkar, Subir Maji, Swapan K Pati, Swadhin K Mondal, submitted (2022)

6.1 Introduction

Since their first isolation and characterization by Arduengo *et al.* in 1991, N-heterocyclic carbenes (NHCs) have found numerous applications in designing various main group and transition metal catalysts [1-4]. Substitution of the C2 position of NHC by "=E" (E = -NR, -CR_2, -PR -O, -S) gives rise to a different class of compounds containing a highly polarised exocyclic double bond [5-6]. As a result of such substitutions, the inherent nucleophilicity of these compounds is introduced to the exocyclic double bonds. When the substituting group (E) is -NH, the resulting compound is designated as N-heterocyclic imine (NHI), first introduced by in 1995 by khun and coworkers [7]. Due to the presence of high ylidic character of the exocyclic imine moiety, NHIs are expected to be as excellent donors and super nucleophilic in character [8-9]. For the last two decades, an extensive research efoorts have been devoted to NHIs. However, the potential of NHIs to act as metal-free catalyst was overlooked [10-19]. Very recently, the use of NHIs for reversible activation of CO_2 has been reported [9, 20]. For example, Dielmann *et al.* reported photoswitchable NHIs for the CO_2 capture by light irradiation [9] while Sarkar *et al.* reported the isolation of triazole-based mesoionic imines (MIIs) III-IV (Figure 6.1) synthesized from mesoionic carbenes (MICs) and investigated its interaction with CO_2 [20]. These reports documented the reversible CO_2 activation by both NHI and MII probed by spectroscopy [9, 21]. However, such CO_2 activation by NHI or MII was never translated into catalytic transformation [9, 20, 22]. Therefore it can be realized that by improving the nucleophilicity of such nitrogen centre may improve this issues.

Previous results demonstrates that abnormal N-heterocyclic carbenes (aNHCs) have higher nucleophilicity and donor ability than the normal N-heterocyclic carbenes (NHC) as well as mesoionic carbenes (MIC) [23]. Thus it can be anticipated that the mesoionic N-heterocyclic imines (mNHIs) V-VI from aNHC, may have

higher nucleophilicity than NHIs I-II, and recently reported MIIs III-IV (Figure 6.1).

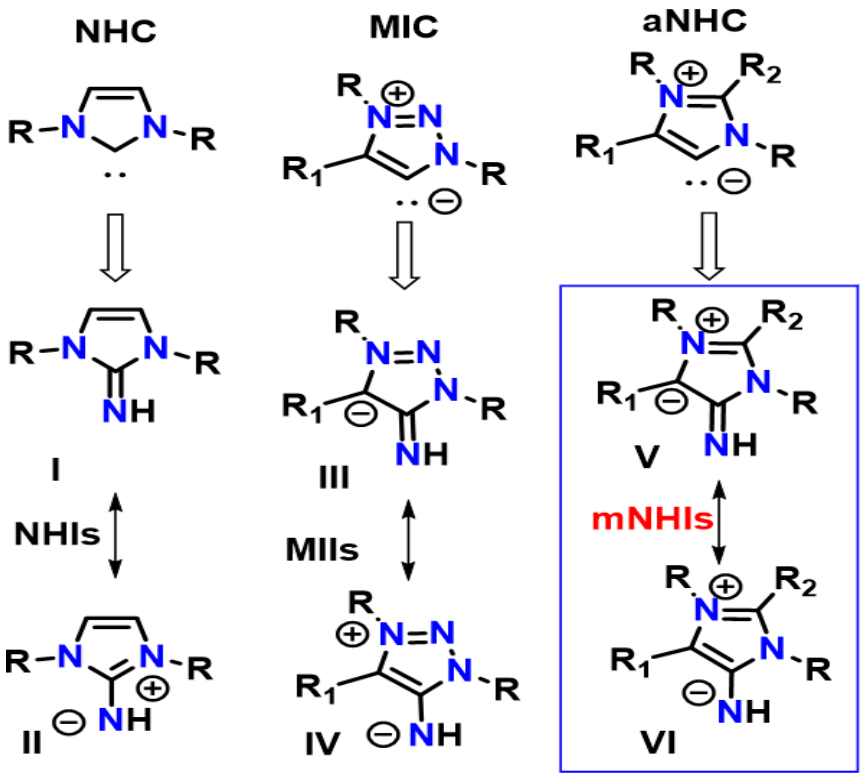

Figure 6.1: Comparison among NHIs, MIIs, and mNHIs.

Recently Mandal and coworkers have synthesized a series of mesoionic N-heterocyclic imines (mNHIs) starting from abnormal N-heterocyclic carbenes (aN-HCs). These super nucleophiles are used in capturing CO_2 and next the captured CO_2 capture is integrated into a catalytic cycle. For this amide functionalization has been chosen with concomitant reduction of CO_2 (Figure 6.2). It may be noted, amides are extremely difficult to be functionalized because of very low basicity and the less availability of nitrogen lone pair of electrons as it delocalizes with adjacent C=O moiety. In other words, in this approach two inert molecules such as CO_2 and amide are activated and catalytically integrated under completely metal-free conditions using mNHI as a catalyst. This results inspired us to initiate a com-

putational study to explore possible reaction intermediates and transition states (TSs) involved in the catalytic pathway.

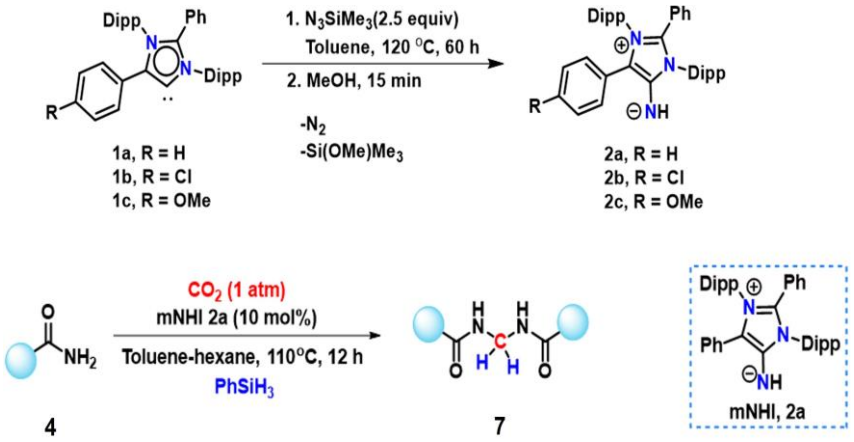

Figure 6.2: Reductive functionalization of amide in presence of CO_2 catalysed by mNHI.

6.2 Computational details

All the electronic structure calculations were performed within density functional theory (DFT) framework. M062X exchange correlation functional along with 6-311g(d,p) basis set have been used for geometry optimizations [24-25]. Proton affinities (PAs) were calculated according to: E(PA) = E(NHI)(protonated) – E(NHI). PA and TDDFT calculations are performed at B3LYP-gd3bj/def2-TZVP level of theory [26,31]. Next all optimized structures are subjected to harmonic vibrational frequency analysis to characterize them as minima (zero imaginary frequency) or transition states (one imaginary frequency). Transition states (TSs) are further verified by intrinsic reaction coordinate (IRC) calculations to confirm their connection to two respective minimum structures. The optimized geometries are further refined with single-point energy calculations at the M062X/6-311++g(d,p) level of theory. The SMD solvation model is used to account for the

solvent (toluene) effects [32]. Thermal corrections were computed at T=383.15K and P=1atm within the rigid rotor simple harmonic oscillator approximation [33]. NRT calculations were performed with NBO 6.0 [34] implemented into the Gaussian16 program suite [35].

6.3 Results and Discussion

At first we devoted our attention to understand the unique nature of this NHI catalysts, **2a**, **2b**, and **2c**. To get an comparative idea about their nucleophilic character and donating ability, we calculated proton affinity (PA) of theses catalysts along with various NHIs, MIIs, mNHIs.The computed values obtained at [B3LYP-gd3bj/def2-TZVP] level of theory indicates that the calculated proton affinities (PA) for mNHIs (for **2a**: 282.0 Kcal/mol, for **2b**: 278.5 Kcal/mol,

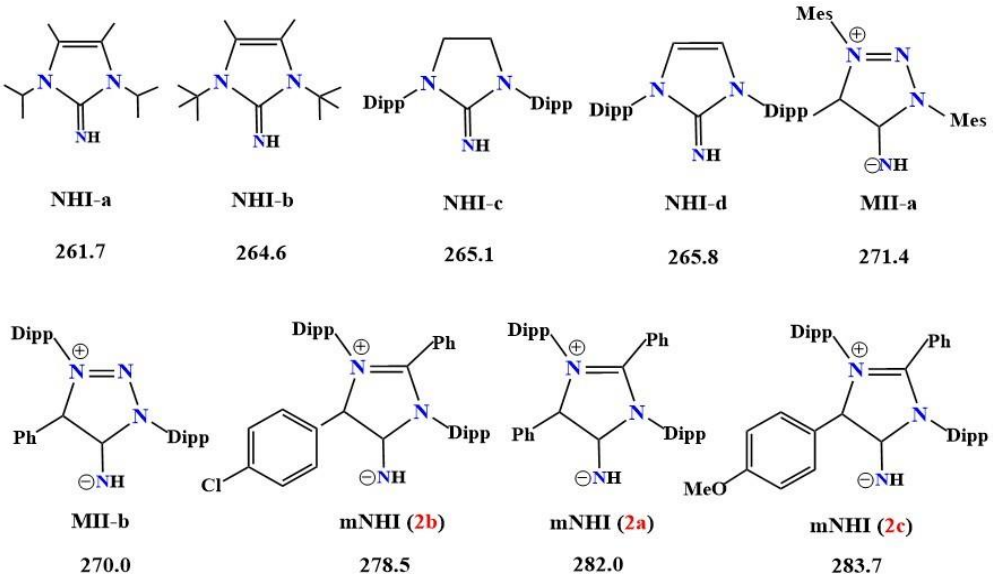

Figure 6.3: Comparison of proton affinity values among various NHIs, MIIs, and mNHIs. All values are reported in kcal/mol.

for **2c**: 283.7 Kcal/mol respectively) are in the highest region among all the NHIs (for NHI-a: 261.7), MIIs (for MII-a: 271.4 Kcal/mol) reported so far (Figure 6.3).

Being mesoionic in nature, these mNHIs cannot be satisfactorily described by a single covalent or polar structure. Rather they are expressed as a resonance hybrid of a series of dipolar canonical structures. In this context, we have performed Natural resonance theory (NRT) calculations of **2a** to determine the relative contributions of all the resonance structures. The results suggest that the ylidic polarization of this mNHI is significantly higher compared to NHIs, mNHOs. Thus it can be said that the high nucleophilicity and high proton affinity of these catalysts arising due to major ylidic structure.

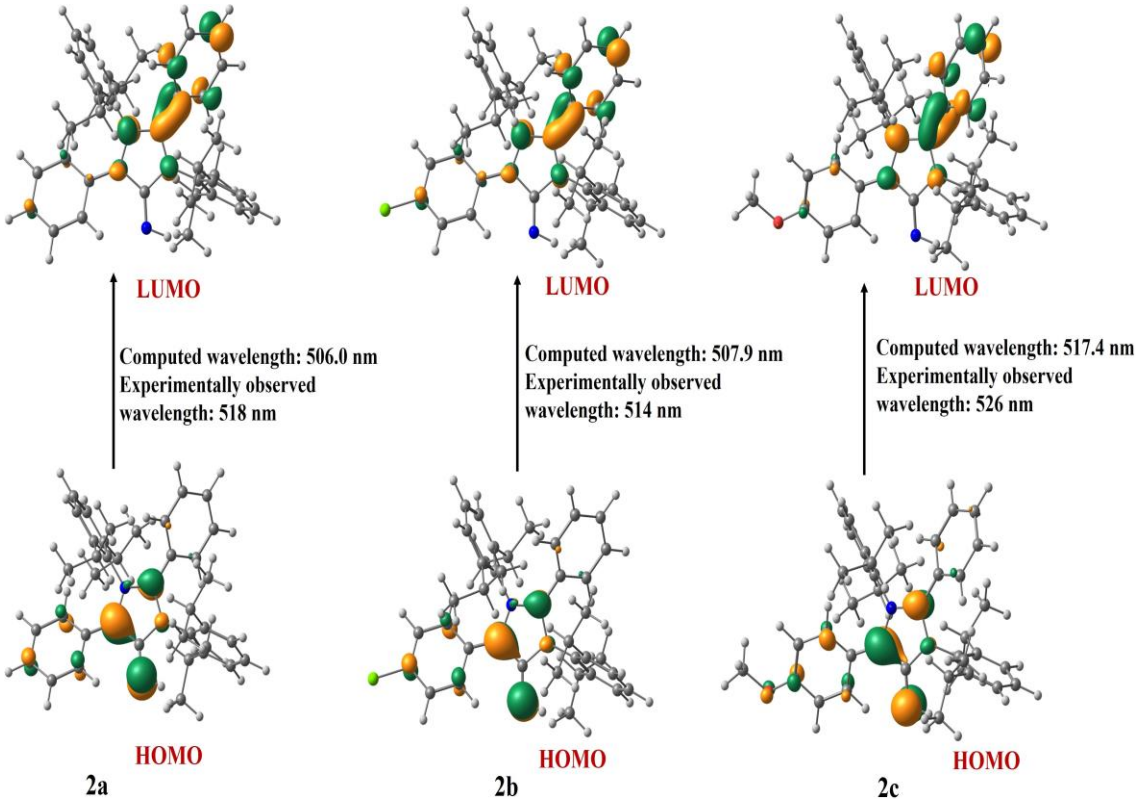

Figure 6.4: Natural transition orbitals (NTOs) for the major absorptions of **2a**, **2b** and **2c** obtained from TDDFT calculations. .

Another unique feature of these catalysts is that, in contrast to other NHIs, which are generally colourless, the mesoionic N-heterocyclic imines (mNHIs) are all bright orange coloured. To understand the origin of such colour, we have performed TDDFT calculations. We found that the computed absorption wavelengths, obtained at [B3LYP-gd3bj/def2-TZVP] level of theory are in good agreement with the experimental findings. Moreover, we observed that the intense absorption observed in these mNHIs arises due to HOMO→LUMO charge transfer transitions from the negatively polarized -NH moiety to the cationic N-heterocyclic moiety of these the mNHIs (Figure 6.4).

After rationalizing the high nucleophilicity of the catalyst, next we focus on understanding the mechanism of the catalytic process. For this, a plausible catalytic cycle is proposed (Figure 6.5).

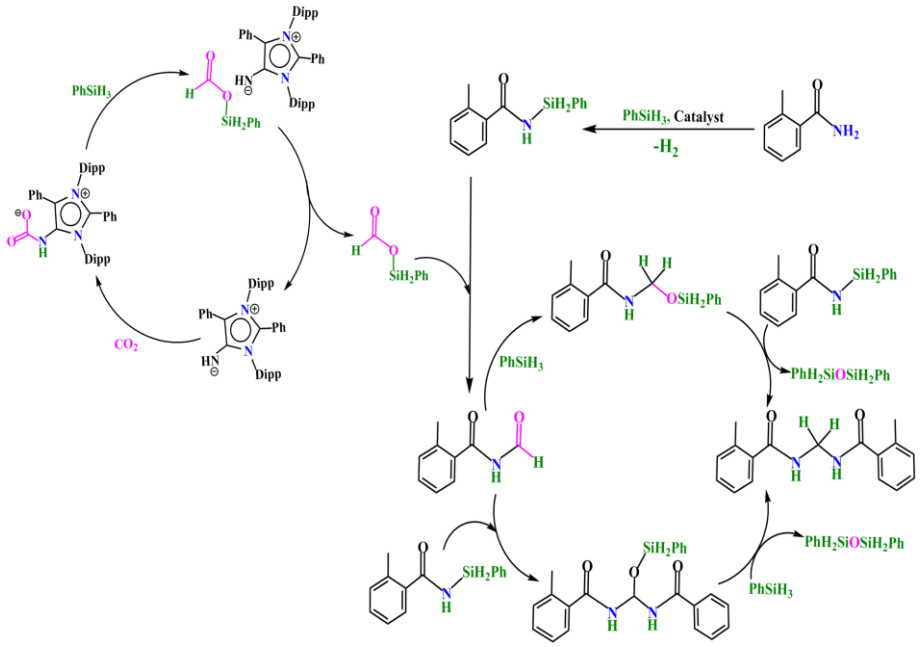

Figure 6.5: Proposed reaction mechanism for the reductive functionalization of CO_2.

The reaction mainly consists of three steps, conversion of CO_2 to silyl formate (step **I**), formation of N-formyl amide from N-silylated amide (step **II**) and CN bond formation (step **III**). These three steps will be described in order. Computa-

tional results reveal that being a strong donor, the catalyst **2** can very easily react with CO_2 and forms a complex **Int1** which can be seen from the value of activation barrier (5.6 kcal/mol) and free energy change (-1.2 kcal/mol) associated with this process. This **Int1** species then attack $PhSiH_3$ through nucleophilic addition,

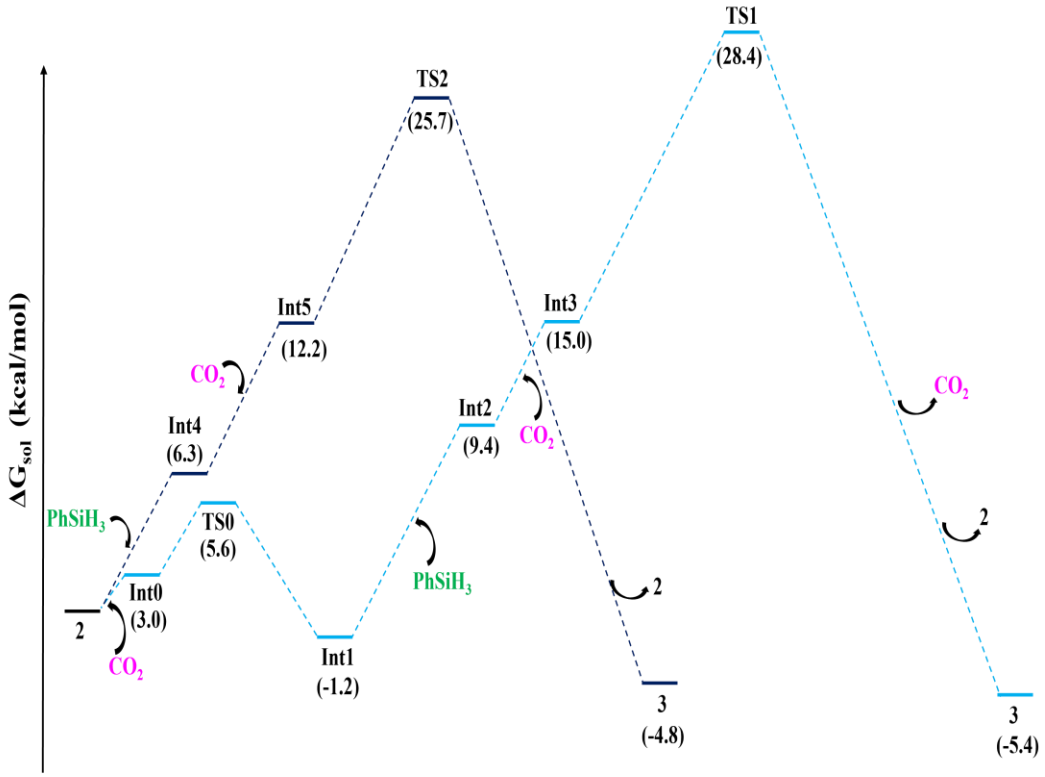

Figure 6.6: The solvent corrected Gibbs free energy profile for the conversion of CO_2 to silyl formate.

forming the active hypervalent silicon compound **Int2**. This **Int2** intermediate is more active donor than $PhSiH_3$ and thus in the next step second CO_2 abstracts the hydride from **Int3** via an SN2-like transition state **TS1** and generates the silane formate. The energy barrier for this hydride transfer process is 28.4 kcal/mol.

At the same time, we found that another pathway is also possible where **2** initially reacts with $PhSiH_3$ itself and results in another hypervalent complex **Int4**. This complex can also transfer the hydride to CO_2 via the transition state **TS2**

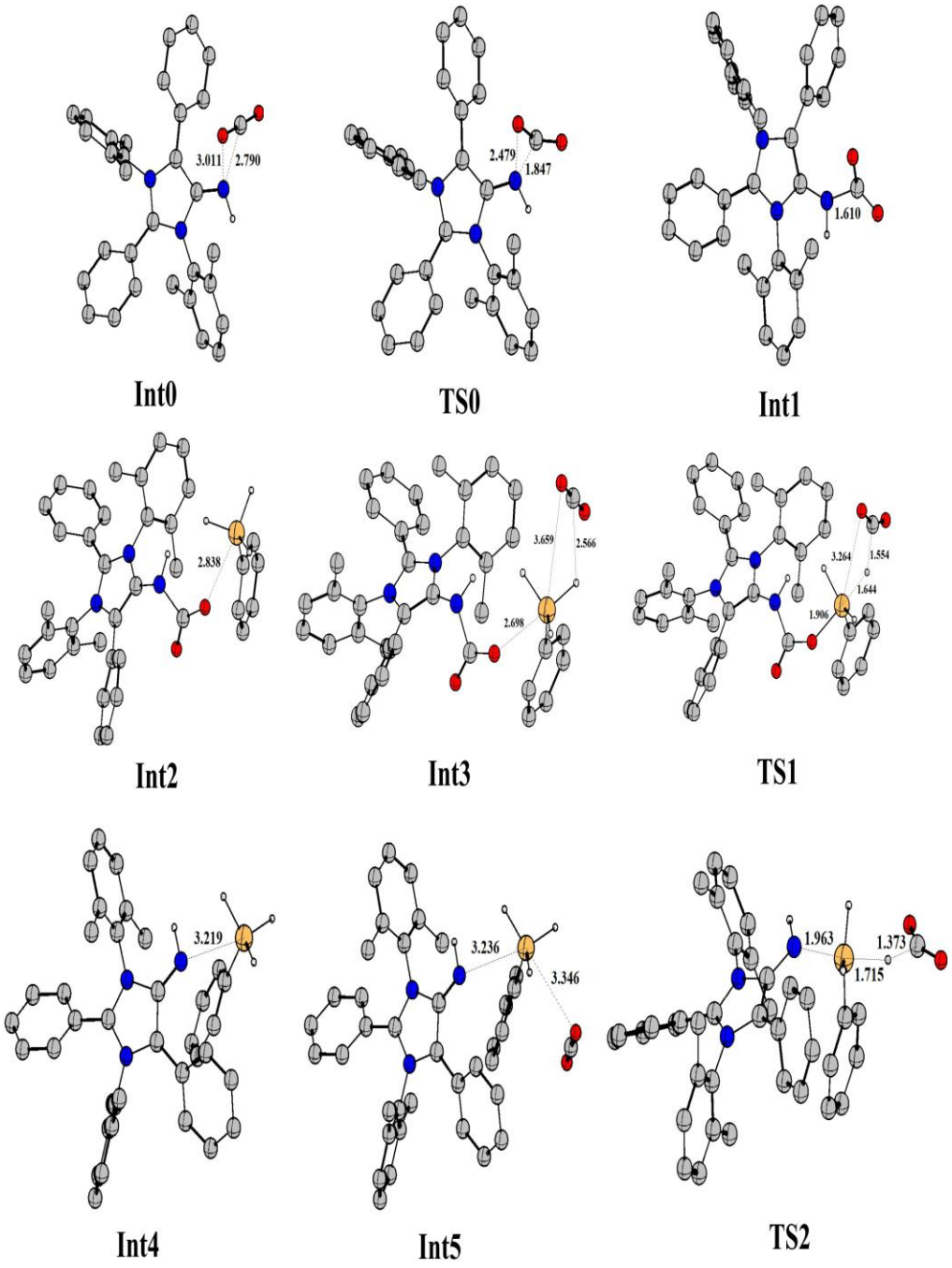

Figure 6.7: Geometry-optimized structures of the intermediate(s)/TS involved in the conversion of CO_2 to silylformate.

where CO_2 inserts into the Si-H bond.The corresponding Gibbs free energy profile depicted in Figure 6.6 shows that both the transition states (**TS1** and

TS2) lie close in the energy profile and therefore both the pathways can lead to the formation of silylformte (**3**).

Simultaneously, the reaction of amide, **4** with $PhSiH_3$ generates the N-silylated amide **5** with the liberation of H_2. Our results indicate that the presence of the catalyst **2** lowers the activation barrier significantly (by 19 kcal/mol) compared to the uncatalysed pathway (Figure 6.8). This behaviour is reflected in the optimized geometries of associated transition states, **TS3** features a shorter H–H distance of 0.905 Å, whereas in **TS3^f** (f=catalyst free) a H–H distance is 1.127 Å(Figure 6.9).

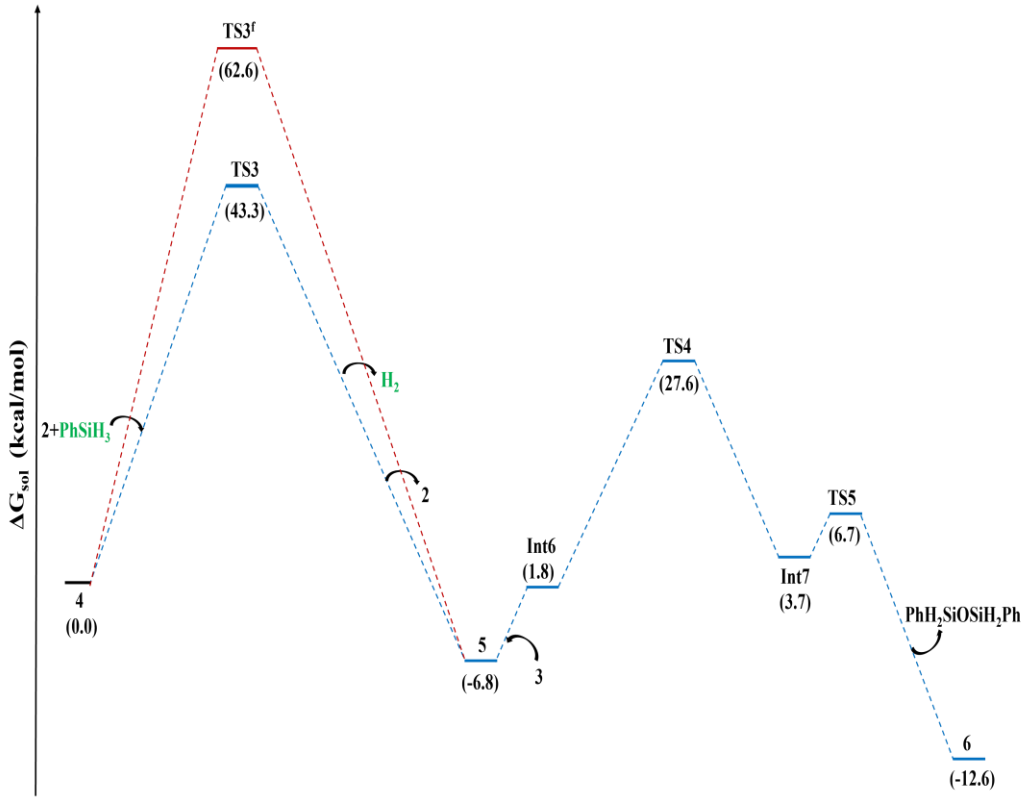

Figure 6.8: The solvent corrected Gibbs free energy profile for the conversion of amide to N-formyl amide.

This N-silylated amide (**5**) can interact with the silylformte (**3**) generated in the previous step, where the NH centre makes a nucleophilic reaction at the carbonyl centre of **3** with a simulateneous interaction of carbonyl oxygen centre and the

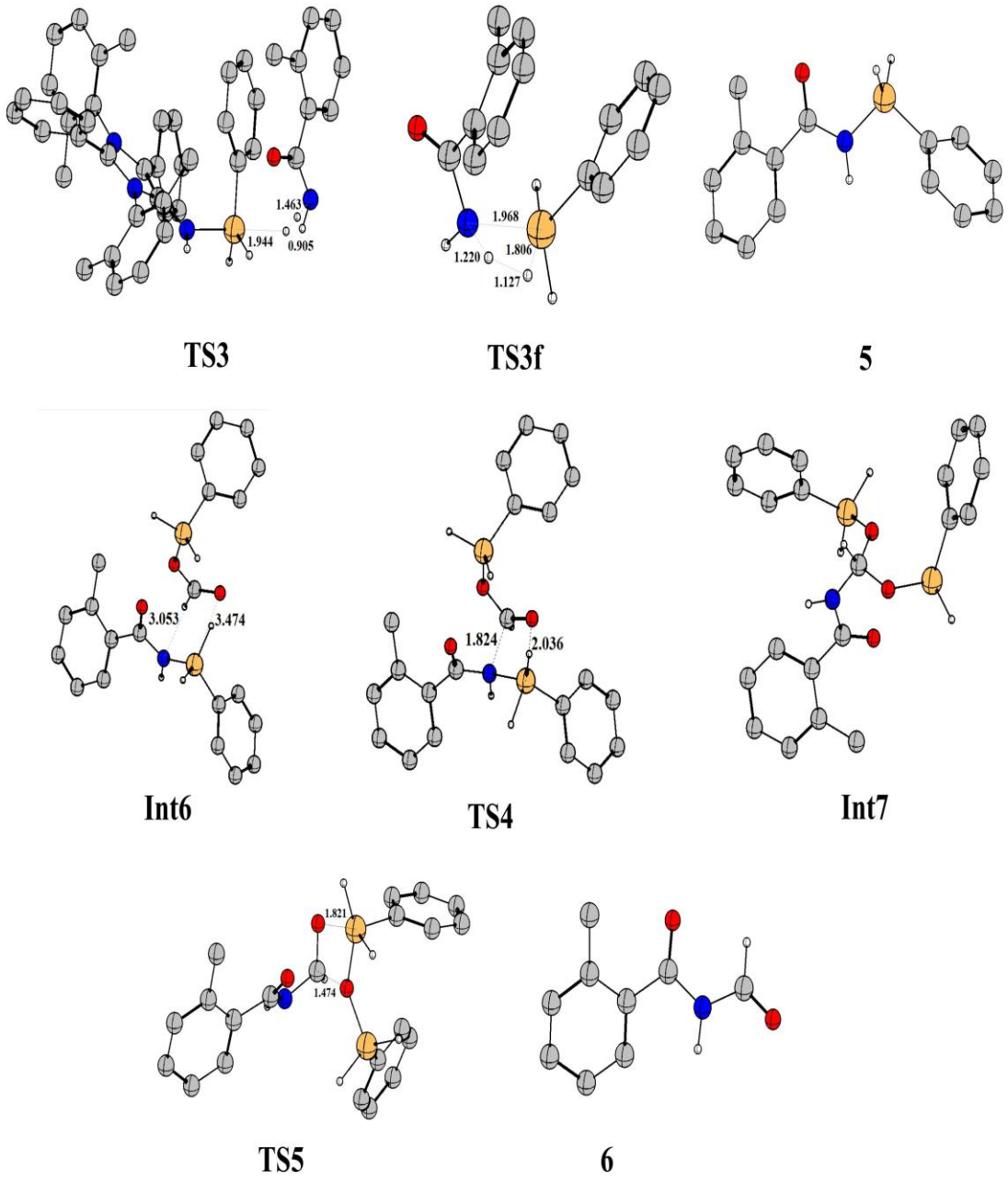

Figure 6.9: Geometry-optimized structures of the intermediate(s)/TS involved in the conversion of amide to N-formyl amide.

silicon centre (Figure 6.8). The transition state associated with this interaction is **TS4** which lies at energy barrier of 27.6 kcal/mol. As a result, the intermediate **int8** is produced which eventually release $PhH_2SiOSiH_2Ph$ via **TS5** and generates

the N-formyl amide (**6**). Note that formation of **6** is also established using a series of control experiments also. Now for the transformation of **6** to the final product two pathways are possible. Either at first the hydride donor $PhSiH_3$ can reduce the formyl group of **6** or **6** can undergoes a nucleophilic attack with a second

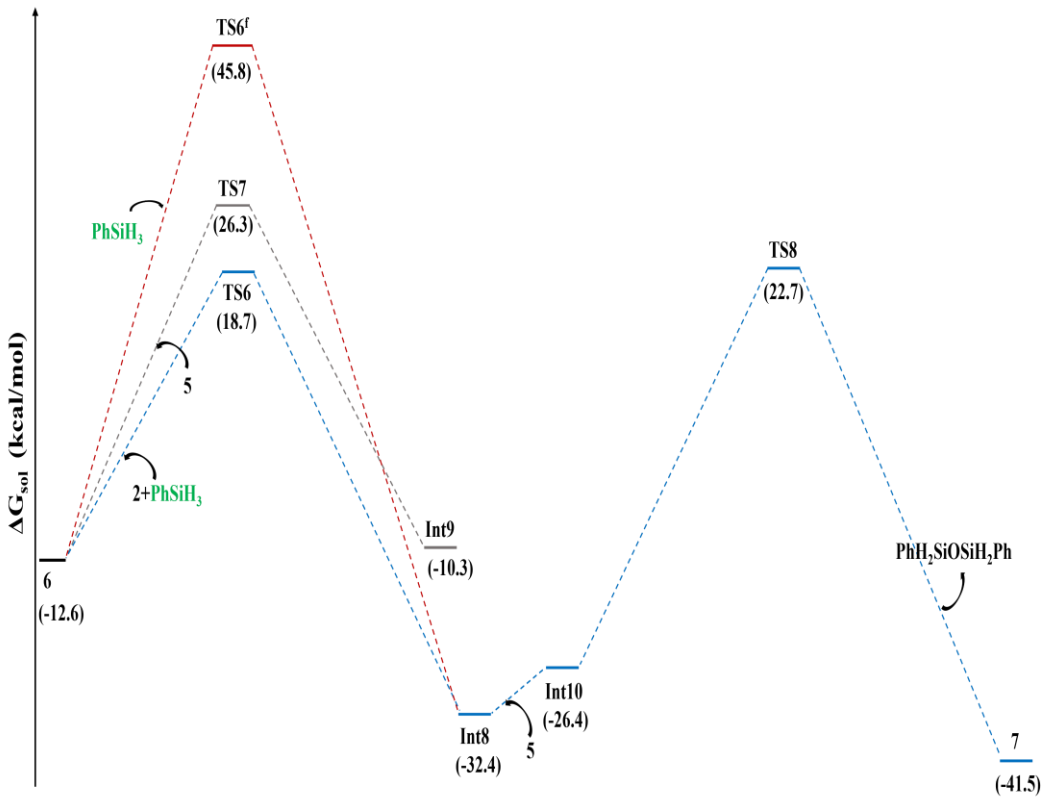

Figure 6.10: The solvent corrected Gibbs free energy profile for the conversion of N-formyl amide to final product.

molecule of **5**. The calculated results show that between the hydride transfer and the nucleophilic attack, the former reaction takes place with a lower barrier with the formation of a very stable intermediate **Int8**. Moreover, it is interesting to observe that the catalyst molecule **2** plays a crucial role in this hydride transfer step. The activation barrier (**TS6**) for this hydride transfer reaction is in the presence of the catalyst is 18.7 kcal/mol. Whereas the barrier associated with the uncatalyzed pathway (**TS6f**) is 45.8 kcal/mol. This suggests active involvement

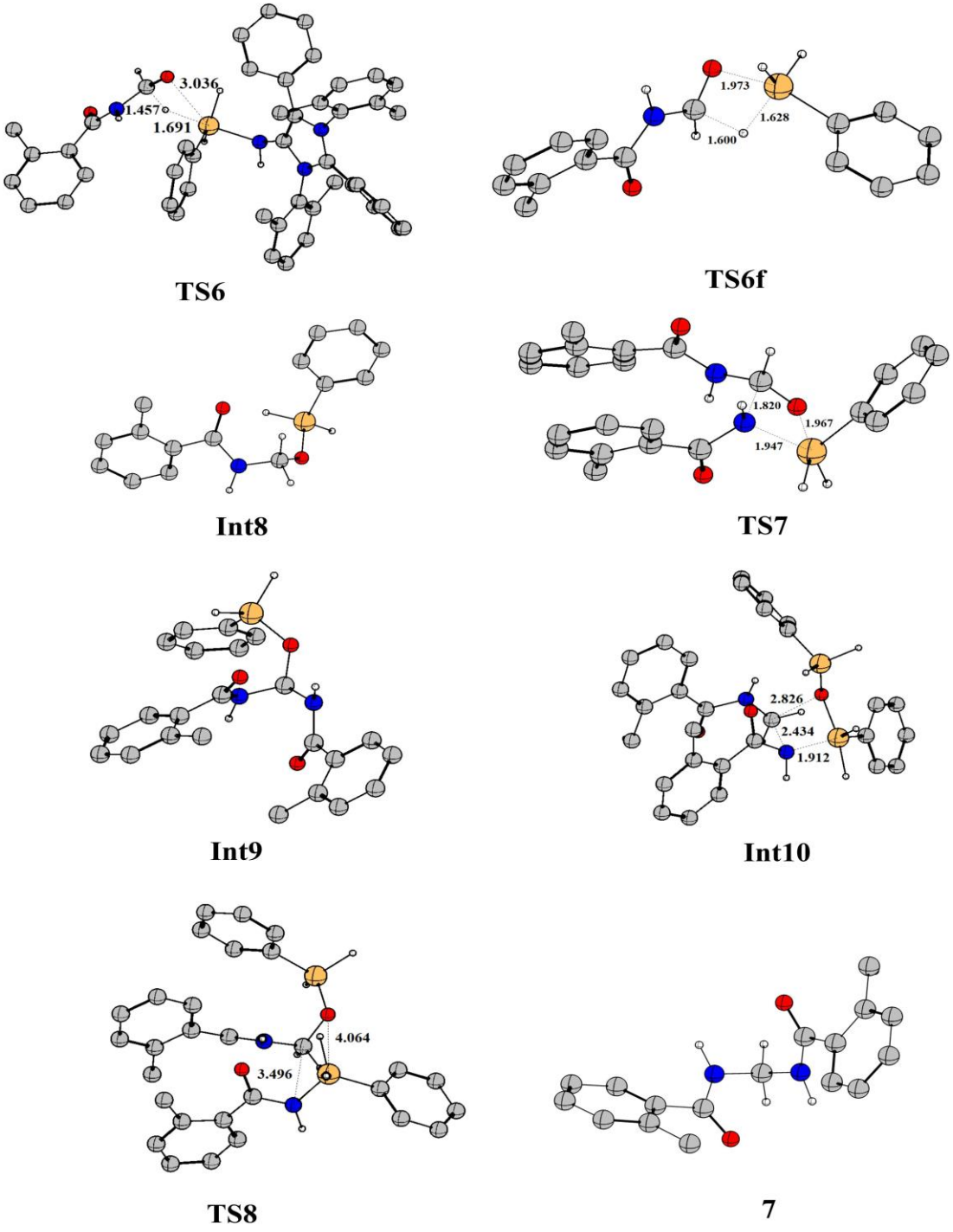

Figure 6.11: Geometry-optimized structures of the intermediate(s)/TS involved in the conversion of N-formyl amide to final product.

of the **mNHI** catalyst to reduce the formyl group of **6** in the presence of silane. Finally, compound **Int8** undergoes a nucleophilic attack by the second molecule of N-silylated amide, **5** resulting in the final product **7** with the liberation of $PhH_2SiOSiH_2Ph$. The transition state for this reaction (**TS8**) lies at 22.7 kcal/mol in the energy profile.

6.4 Conclusions

In summary, we can say we have studied a new class of mesoionic N-heterocyclic imines **mNHIs** which can act as strong nucleophile and can performs reductive functionalization using CO_2 as the methylene source while coupling inert amide molecules. Proton affinity calculations and NRT analysis confirms that this high nucleophilicity is associated with the polarized ylide structure. Moreover these **mNHIs** display an unique colour due to a charge transfer transition from its highest occupied molecular orbital to lowest unoccupied molecular orbital. The mechanistic study suggests that the **mNHIs** can easily react with CO_2 as well as $PhSiH_3$ and both the pathways can generate the silyl formate species. The catalyst plays a crucial role in the formation of N-silylated amide and in the reduction of formyl group of N-formyl amide. We also observed that formation of C-N bond which is last step of this reaction, takes place by an initial hydride transfer followed by a nucleophilic reaction.

6.5 References

[1] Arduengo, A., J., Harlow, R. L., Kline, M. A Stable Crystalline Carbene. J. Am. Chem. Soc. 1991, 113, 361–363.

[2] Hopkinson, M., Richter, C., Schedler, M.Nature 2014, 510, 485–496.

[3] Nesterov, V., Reiter, D., Bag, P., Frisch, P., Holzner, R., Porzelt, A., Inoue,

S. Chem. Rev. 2018, 118, 96789842.

[4] Zhao, Q., Meng, G., Nolan, S. P., Szostak, M. Chem. Rev. 2020, 120, 19812048.

[5] Kuhn, N. Al-Sheikh, A. 2,3-Dihydroimidazol-2-ylidenes and their main group element chemistry. Coord. Chem. Rev. 2005, 249, 829-857.

[6] Cicač-Hudi, M., Schlindwein, S. H., Feil, C. M., Nieger, M. Gudat, D. Chem. Commun. 54, 7645-7648 .

[7] Kuhn, N., Fawzi, R., Steimann, M., Wiethoff, J., Blaser, D. Boese, R. Z. Naturforsch. 1995, 50b, 1779.

[8] Loh, Y. K. Angeles Fuentes, M., Vasko, P. Aldridge, S. Angew. Chem. Int. Ed. 2018, 57, 16559 –16563.

[9] Wilm, L. F. B., Das, M., Janssen-Mgller, D., Mgck-Lichtenfeld, C., Glorius, F. Dielmann, F. Angew. Chem. Int. Ed. 2022, 61, e202112344.

[10] Kuhn, N., Gohner, M., Grathwohl, M., Wiethoff, J., Frenking, G. Chen, Y. Z. Anorg. Allg. Chem. 2003, 629, 793-802.

[11] Kuhn, N. Al-Sheikh, A. Coord. Chem. Rev. 2005, 249, 829–857.

[12] Panda, T. K., Trambitas, A. G., Bannenberg, T., Hrib, C. G., Randoll, S., Jones, P. G. Tamm, M. Inorg. Chem. 2009, 48, 5462.

[13] Trambitas, A. G., Panda, T. K., Jenter, J., Roesky, P. W., Daniliuc, C., Hrib, C. G., Jones, P. G. Tamm, M. Inorg. Chem. 2010, 49, 24352446.

[14] Trambitas, A. G., Panda, T. K. Tamm, M. Chem. 2010, 636, 2156 – 2171.

[15] Revathi, S., Raja, P., Saha, S., Eisen, M. S. Tapas Ghatak Chem. Commun. 2021, 57, 5483–5502.

[16] Tamm, M., Petrovic, D., Randoll, S., Beer, S., Bannenberg, T., Jones, P. G. Grunenberg, J. Org. Biomol. Chem. 2007, 5, 523.

[17] Wu, X. Tamm, M. Coord. Chem. Rev. 2014, 260, 116–138.

[18] Doddi, A., Peters, M. Tamm, M. Chem. Rev. 2019, 119, 6994-7112.

[19] Beer, S., Hrib, C. G., Jones, P. G., Brandhorst, K., Grunenberg, J. Tamm,

M. Angew. Chem. Int. Ed. 2007, 46, 8890.

[20] Rudolf, R., Neuman, N. I., Walter, R. R. M., Ringenberg, M. R. Sarkar, Angew. Chem.Int. Ed. 2022, 61, e2022006.

[21] Saha S. Eisen M. S. ACS Catal. 2019, 9, 5947-5956.

[22] Wilm, L. F. B., Eder, T., Mgck-Lichtenfeld, C., Mehlmann, P., Wgnsche, M., Buß, F. Dielmann, F. Green Chem. 2019, 21, 640 – 648.

[23] Sau, S. C., Hota, P. K., Mandal, S. K., Soleilhavoup, M. Bertrand, G. Chem. Soc. Rev. 2020, 49, 12331252.

[24] Zhao, Y.; Truhlar, G. D. Theor. Chem. Account. 2008, 120, 215241.

[25] Zhao, Y.; Truhlar, G. D. Acc. Chem. Res. 2008, 41, 157167.

[26]. Lee, C.; Yang, W.; Parr, R. G., Phys. Rev. B 1988, 37, 785-789

[27] Miehlich, B.; Savin, A.; Stoll, H.; Preuss, H. Chem. Phys. Lett. 1989, 157, 200-206.

[28] Grimme, S.; Ehrlich, S.; Goerigk, L.J. Comput. Chem. 2011, 32, 1456-1465.

[29] Grimme, S.; Antony, J.; Ehrlich, S.; Krieg, H. J. Chem. Phys. 2010, 132, 154104-154119 .

[30] Grimme, S. J. Comput. Chem., 2004, 25, 1463-1473.

[31] Grimme, S. J. Comput. Chem. 2006, 27, 1787-1799.

[32] Marenich, A. V.; Cramer, C. J.; Truhlar, D. G. J. Phys. Chem. B. 2009, 113, 6378639.

[33] Luchini, G.; Alegre-Requena, J. V.; Funes-Ardoiz, I.; Paton, R. S. F1000Research 2020, 9, 291.

[34] NBO 6.0. E. D. Glendening, J. K. Badenhoop, A. E. Reed, J. E. Carpenter, J. A. Bohmann, C. M. Morales, C. R. Landis, F. Weinhold (Theoretical Chemistry Institute, University of Wisconsin, Madison, WI, 2013); http://nbo6.chem.wisc.edu/.

[35] Frisch, M. J. et al., Gaussian 16 Revision A.03. 2016; Gaussian Inc. Wallingford CT.

7

Exploring Dicordinate Stibenium Cations as Efficient Hydroboration and Cyanosilylation Catalysts

Work reported in this chapter is based on: Nilanjan Sen, Prachi Gothe, Pallavi Sarkar, Shubhajit Das, Swapan K Pati, Shabana Khan, Chem. Comm. (under revision)

7.1 Introduction

There is no doubt that during the last few years p-block elements have gained special attention due to their cost-effectiveness and environmentally benign nature [1-4]. Among them particularly p-block cations are most promising Lewis acid catalysts due to their inherent electrophilicity [5-8]. The research carried out through the 20th century establishes the fact that the group 13 and 14 cations can act as efficient catalysts in several organic transformations [5-13]. Exploration of unique reactivity of cationic compounds is now not only limited to group 13 and 14 elements but has also witnessed an extraordinary development in the chemistry of group 15 elements. Recently, the phosphenium cations were shown to perform asymmetric organocatalysis as well as regio- and chemo-selective hydroboration [14-16]. Recently Melen *et al.* has introduces N-heterocyclic arsenium cations and as catalysts for the hydroboration of aldehydes. However, the antimony analogue of phosphenium cation, namely stibenium (Sb(III)) cations have not been utilized for such reaction. Due to the presence of a lone pair of electrons and a vacant p-orbital, stibenium cations are ambiphilic in nature and appears as a unique low valent species [17-30]. But at the same time group 15 cationic species are weak σ-donor and better π-acceptor [31]. Thus stibenium cations are expected to be strong electrophilic nature and this vehaviour is accountable for the less occurrence of the donor free stibenium cations [21,30]. Recently khan and coworkers have successfully synthesized a series of novel donor free cyclic and acyclic stibenium cations (Figure 7.1) via dehalogenation pathway using respective silver salts, $AgSbF_6$ (for compound A) and AgOTf (for compound B and C). Therefore, it is quite interesting to explore the potential catalytic application of these stibenium cations, which is the focus of the current chapter.

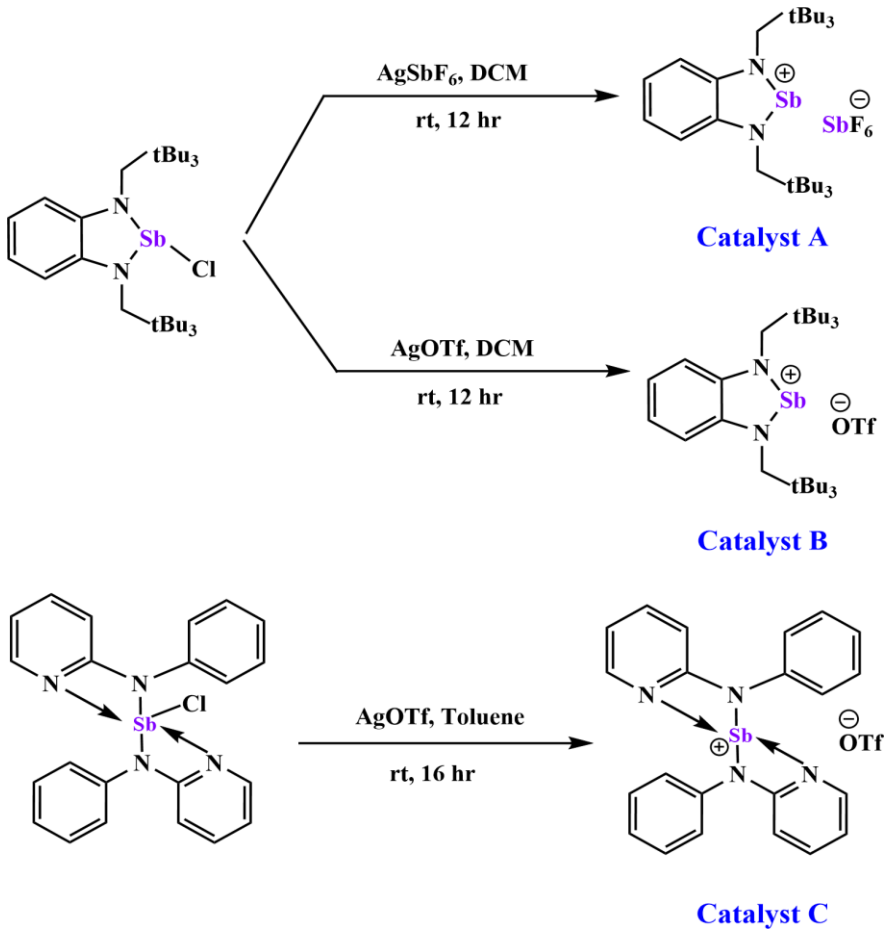

Figure 7.1: Different stibenium cations studied in this work.

7.2 Computational details

Calculations of electronic structure of all the systems are carried out under the framework of density functional theory. For geometry optimization, M062X exchange-correlation functionals along with 6-311G(d,p) basis set is used for lighter atoms (C, H, B, N, O, F) [31,32]. For Sb, we have used def2TZVP basis set in combination with Stuttgart-Dresden pseudopotential [33]. All optimized geometries are characterized by harmonic vibrational analysis to recognize the structures as minima (all positive frequencies) or transition state (one negative frequency). Transition states are (TS) are verified through intrinsic reaction coordinate (IRC) calculations. All

thermochemical data are estimated within the ideal gas-rigid rotor-harmonic oscillator approximation at 298.15 K and 1 atm pressure. SMD model is used to consider solvent effects as proposed by Truhlar and Cramer. The computed entropic corrections are further scaled to 75% in order to take into account the quenching of translational and rotational degrees of freedom in the solution phase [34-37].

7.3 Results and Discussion

7.3.1 Structural features

The computational study commences with the geometry optimizations of the three catalyst's structures. When we looked at closely the optimized geometries, we observed that the counter anions are loosely bound with the cationic core for these catalysts (Figure 7.2). Particularly, catalyst **A** features a discrete cationic structure with hexafluoroantimonate $[SbF_6]^-$ as the counter anion displaying long contacts with the fluorine atoms of $[SbF_6]^-$ anions with Sb-F bond distances of 2.524 Å. On the contrary, for catalyst **B**, the molecular structure displays a close contact of triflate $[OTf]^-$ anion with the antimony centre resulting in the Sb-O

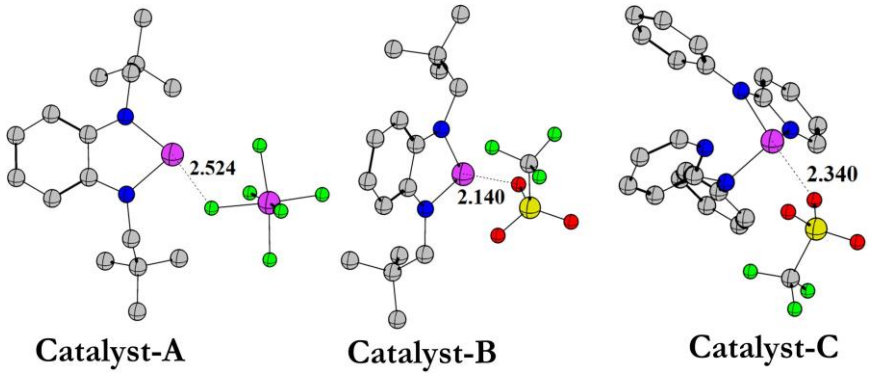

Figure 7.2: Geometry optimized structures of Catalyst **A**, **B** and **C**. Atom colour code: C (grey), N (blue), O (oxygen), F (green), S (yellow), Sb (purple). Hydrogen atoms are omitted for clarity.

bond distance of 2.140 Å. For acyclic catalyst **C** which is based upon the amino pyridyl framework, the molecular structure has a tetra-coordinated pyramidal geometry with a distance of 2.340 Å from the counter anion. Natural bonding analysis of these optimized structures unveils the presence of an electron-donating interaction from the oxygen centre of the $[OTf]^-$ anion to the vacant p orbital of the Sb centre of catalyst **B** ($\Delta E^{(2)}$= 86.3 kcal/mol) and catalyst **C** ($\Delta E^{(2)}$= 63.2 kcal/mol), which is mainly predominant for catalyst **B** (Figure 7.4). However no such interaction is observed in case of catalyst **A**.

Catalyst-A = Cationic part + $[SbF_6]^-$ $\triangle G$ = 27.8 kcal/mol

Catalyst-B = Cationic part + OTf^- $\triangle G$ = 42 kcal/mol

Catalyst-C = Cationic part + OTf^- $\triangle G$ = 36.1 kcal/mol

Figure 7.3: Computed free energies of anion dissociation values for Catalyst **A**, **B** and **C**

These results are further supported by the computed dissociation energies (Figure 7.3) for these systems which indicate weaker coordination with the counter anion, $[SbF_6]^-$ and therefore higher Lewis acidity at the stibenium ion centre for catalyst **A** compared to the catalyst **B** and **C**, respectively.

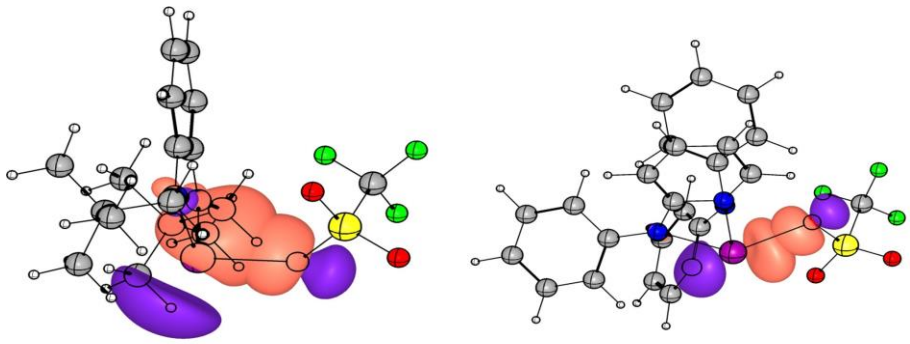

Catalyst-B Catalyst-C

Figure 7.4: Presence of electron-donating interaction for Catalyst **B** and **C**. Atom colour code: C (grey), N (blue), O (oxygen), F (green), S (yellow), Sb (purple).

7.3.2 Catalytic hydroboration reaction

Owing to the Lewis acidic character of these pnictenium cations, next we examined the catalytic behaviour of **A**, **B** and **C** for hydroboration of aromatic carbonyl compounds. It is needless to say hydroboration reaction, which is the addition of a hydrogen-boron bond to unsaturated C-C, C-N or C-O bonds, is receiving quite an attention in modern chemistry both industrially and academically, owing to its wide application in the synthesis of various important synthons. At the same time, aldehydes and ketones are the most common substrate scope for organo-catalytic hydroboration reactions.

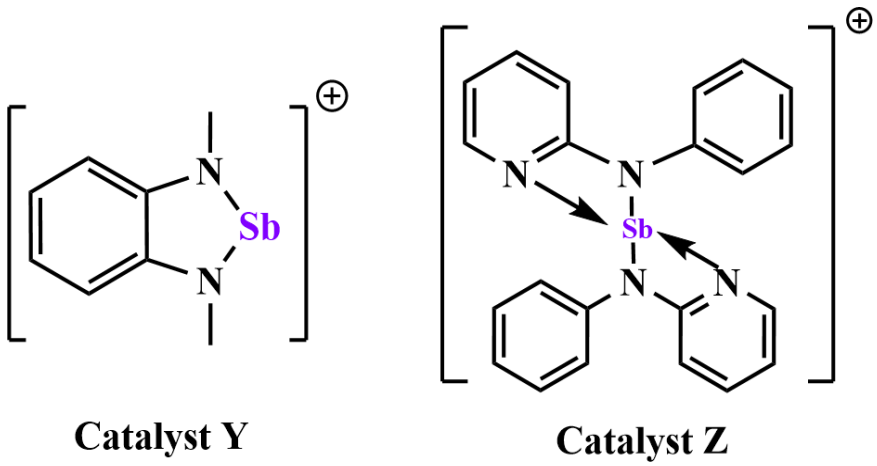

Catalyst Y **Catalyst Z**

Figure 7.5: The model catalysts used for the initial investigation of reaction mechanism.

As discussed before, for these catalysts, the counter anions are weakly coordinated to the cationic centre. Therefore, at first, we explored the reaction mechanisms considering only the cationic part of the catalyst molecule, which eventually is the active site of the catalyst. Catalyst **A** and **B** have a common cationic structure which is designated here as catalyst **Y** and the cationic part of **C** is designated as **Z** (see Figure 7.5). For simplicity, the neopentyl group of N centre in **A** and **B** are replaced by the methyl group, where the structure for catalyst **C** is kept unchanged. Our previous studies have already shown that such minor

changes in the electronic and structural properties do not affect the reactivity of the catalyst systems [38] .

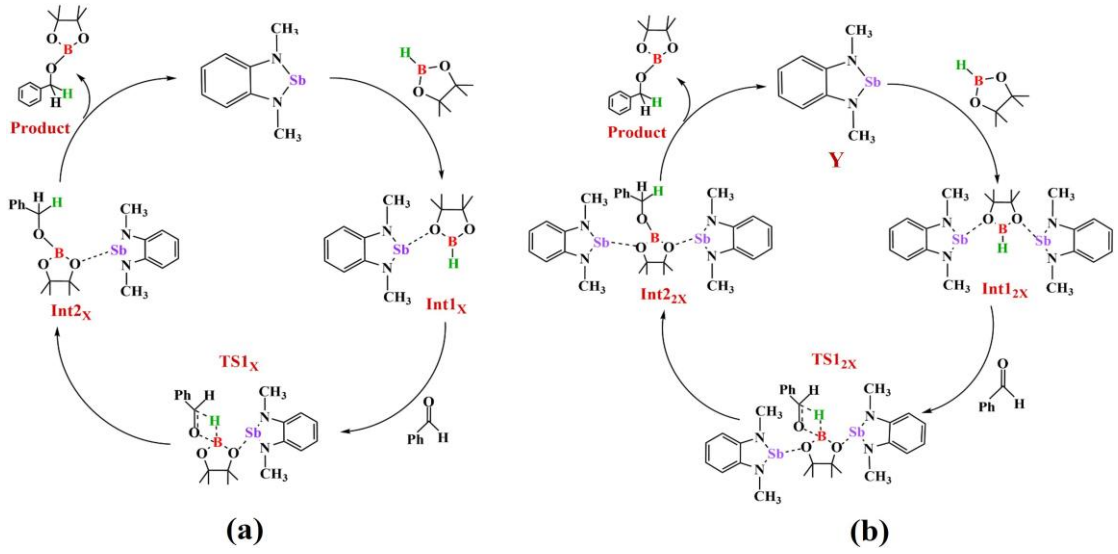

Figure 7.6: Catalytic cycle for hydroboration of benzaldehyde using the model catalyst **Y** (a) single-anchoring pathway (b) double-anchoring pathway.

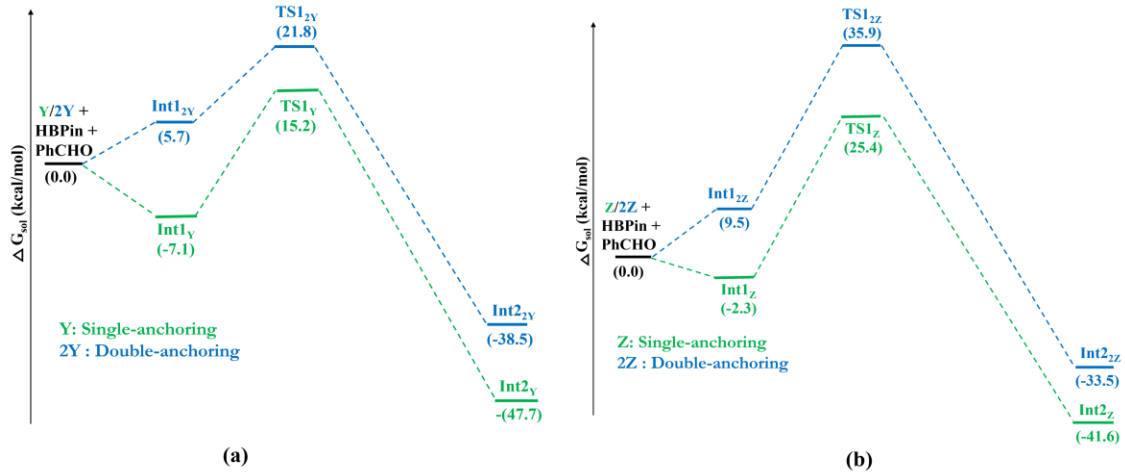

Figure 7.7: The solvent corrected Gibbs free energy profiles for the hydroboration of PhCHO catalysed by (a) **Y** and (b) **Z**. The green profile corresponds to the single-anchoring mechanism whereas the blue profile corresponds to the double-anchoring mechanism.

The hydroboration reaction proceeds via an anchoring mechanism, where the catalyst molecule is anchored with the electronegative oxygen atom of pinacol

borane. This eventually opens up two possibilities, that is the single-anchoring mechanism, where a single catalyst molecule is anchored with borane (Figure 7.6) as well as the double-anchoring mechanism, where two catalyst molecules are anchored with the HBPin molecule (Figure 7.6). We have studied both the possibilities using benzaldehyde as a model aromatic aldehyde substrate. In their recent work khan *et al.* have shown that the hydroboration reaction by germylene and stannylene catalysts with a very similar structural framework proceeds by a double-anchoring mechanism [38]. However, our computed results indicate for both the systems, **Y** and **Z**, the single-anchoring mechanism has a lower activation energy barrier compared to the double-anchoring mechanism (Figure 7.7). This observation is further confirmed with the ketone substrate ($PhCOCH_3$) also (Figure 7.8). Hence it can be concluded that hydroboration reactions of aldehyde and ketone by these class of stibenium cations favour the single-anchoring pathway over the double-anchoring pathway.

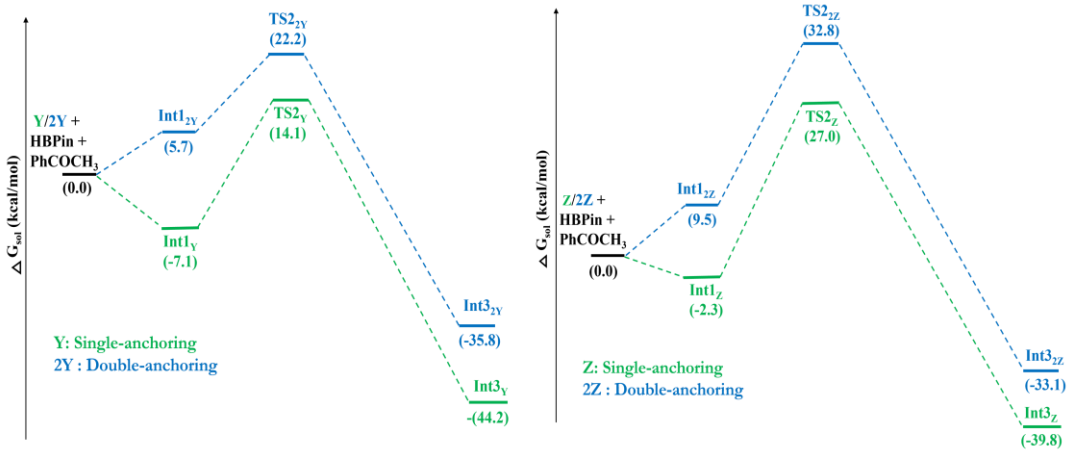

Figure 7.8: The solvent corrected Gibbs free energy profiles for the hydroboration of $PhCOCH_3$ catalysed by (a) **Y** and (b) **Z**. The green profile corresponds to the single-anchoring mechanism whereas the blue profile corresponds to the double-anchoring mechanism.

After deciding on the mechanism, we have studied the catalytic pathway with the catalysts **A**, **B** and **C**, where the counter anions are present (Figure 7.9).

Hydroboration reaction begins with the coordination of HBPin with the catalyst molecule leading to the formation of the **Int1**. The donor-acceptor interaction between the oxygen lone pair of HBPin and the vacant p orbital of the Sb atom of the catalyst molecule lowers the energy of the **Int1** complex. NBO analysis of **Int1**s reveals that this interaction is stronger in **A** ($\Delta E^{(2)}$=18.8 kcal/mol) compared to **B** ($\Delta E^{(2)}$=10.9 kcal/mol) and **C** ($\Delta E^{(2)}$=3.0 kcal/mol), which is a

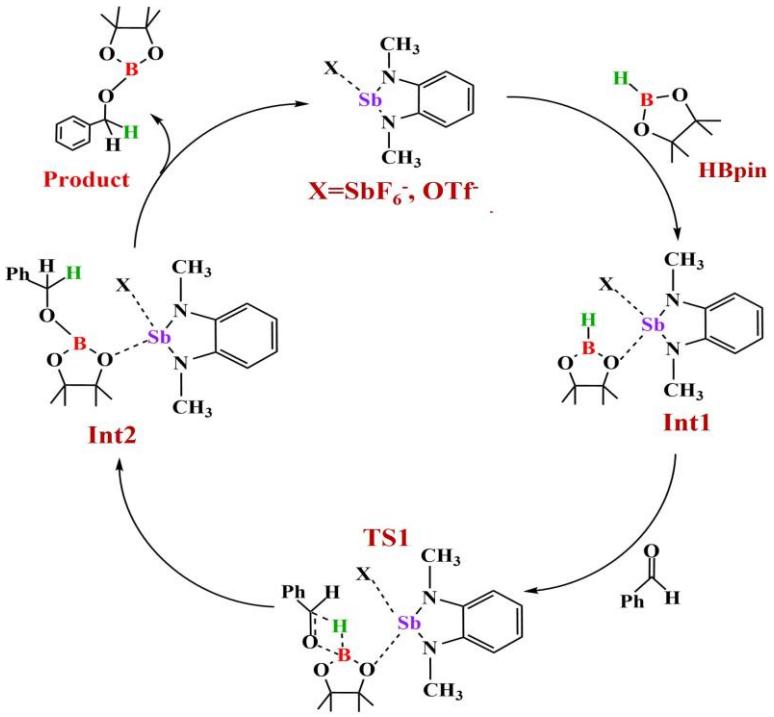

Figure 7.9: Proposed catalytic cycle for hydroboration of benzaldehyde using the catalysts **A**, **B** and **C**.

manifestation of the unquenched Lewis acidity of the Sb centre in **A**. This behaviour is also reflected in the shorter Sb-O distance of 2.611 Å in **Int1A** compared to the Sb-O distance of 2.779 Å in **Int1B** and Sb-O distance of 3.359 Å in **Int1C**. Now the addition of benzaldehyde in **Int1** results in a nucleophilic attack of the carbonyl oxygen centre to the boron centre of HBPin and a hydride transfer to the carbonyl carbon occurs via a four-membered TS, **TS1**. At **TS1**, the catalysts unit anchor to HBPin more strongly which is indicated by the lowering of the respective

Sb-O distance (Figure 7.11). This anchoring is most effective for **A** (Sb-O distance of 2.374 Å) resulting in the lowest free energy activation barrier of 16.3 kcal/mol. On the other side, because of the steric crowding at the Sb centre of catalyst **C**, this anchoring is very weak (Sb-O distance of 3.141 Å). As a result, **TS1C** lies at 27.7 kcal/mol in the gibbs free energy profile (Figure 7.10). However, for **B** this anchoring strength is in between (Sb-O distance 2.503 Å), which gives rise to a moderate value of **TS1B** , 21.7 kcal/mol. **TS1** then relaxes to **Int2** in

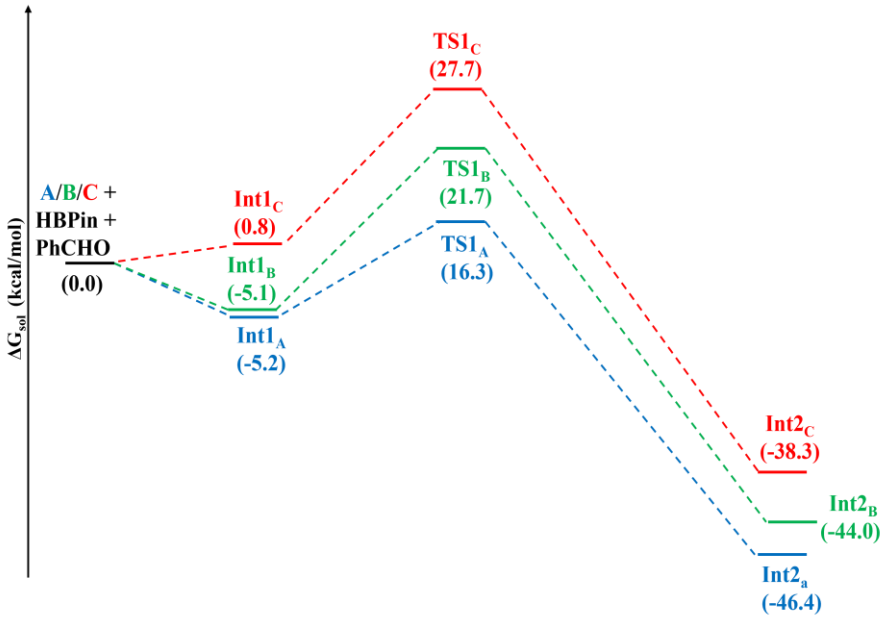

Figure 7.10: The solvent corrected Gibbs free energy profiles for the hydroboration of PhCHO catalysed by **A**, **B** and **C**.

which anchoring becomes much weaker (Sb-O distances are 2.451 Å, 2.781 Å and 3.452 Å for **A**, **B** and **C** respectively). Finally, **Int2** dissociates to release the catalyst molecules and yields the desired alkoxy pinacol boronate ester ($PhCH_2OBPin$). Now the ketone hydroboration also follows a similar mechanism, which is studied using acetophenone ($PhCOCH_3$) as model substrates. For the hydroboration between $PhCOCH_3$ and HBPin catalysed by a the **TS2A** lies at 16.1 kcal/mol whereas **TS2B** and **TS2C** lie at 21.6 kcal/mol and 29.7 kcal/mol in

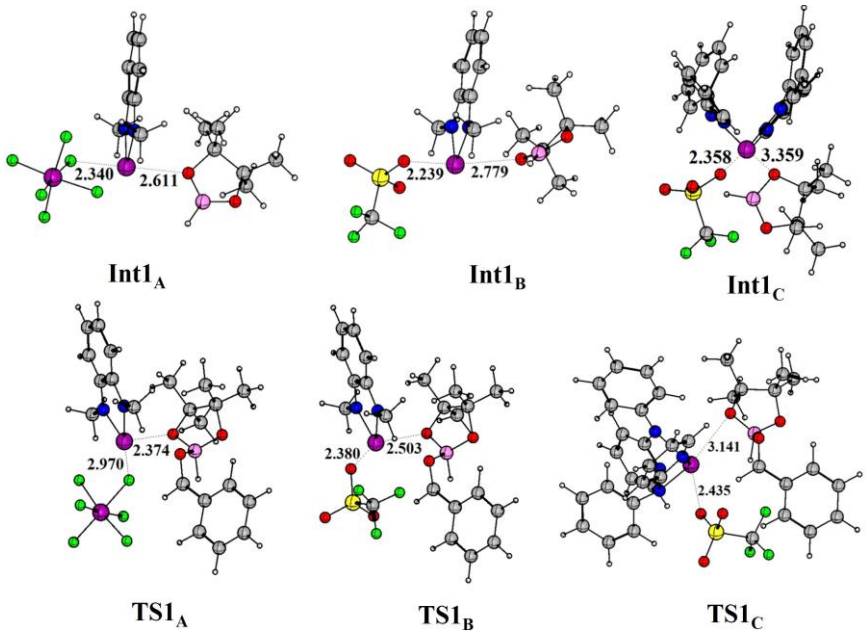

Figure 7.11: The geometry optimized structures of the intermediates/TSs involved in the hydroboration of PhCHO. Atom colour code: C (grey), N (blue), O (oxygen), F (green), S (yellow), Sb (purple).

the free energy profile (Figure 7.12), which actually follows the trend just before discussed for benzaldehyde hydroboration. This result indicates that catalyst **A** can perform hydroboration reactions for aromatic aldehyde and ketone under mild conditions whereas due to the rigid steric crowding around the active centre for catalyst **C**, the reaction scope is limited. Although catalyst **B** does not suffer from such steric hindrance during the reaction, it experiences a reduced of Lewis acidity quenched by the counter anion. As a result, it is difficult for catalyst **B** to perform hydroboration of carbonyl compounds.

7.3.3 Catalytic cyanosilylation reaction

The promising catalytic behaviour of this stibenium ions encourage us to explore their potential for cyanosilylation reaction of aromatic aldehyde. A plausible mechanism for the cyanosilylation of benzaldehyde using catalyst **A** and **B** are depicted

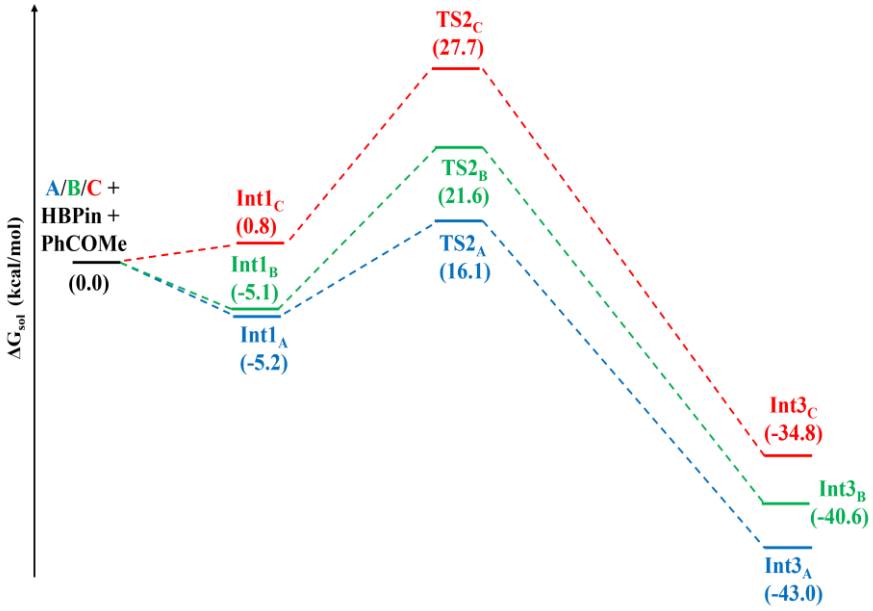

Figure 7.12: The solvent corrected Gibbs free energy profiles for the hydroboration of PhCOMe catalysed by **A**, **B** and **C**.

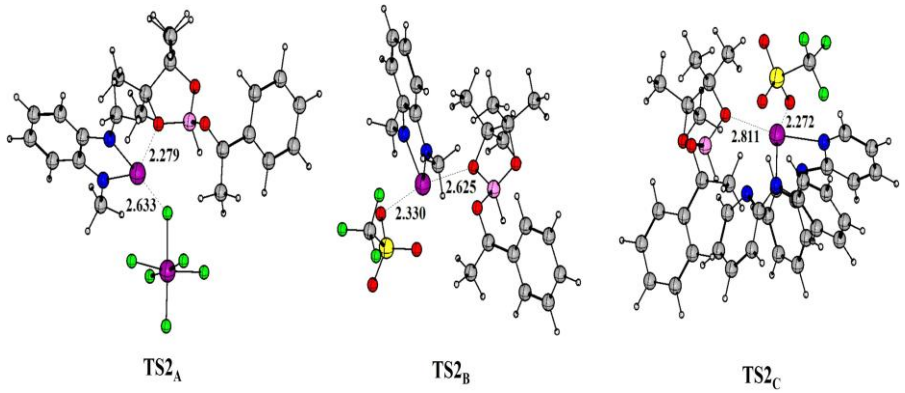

Figure 7.13: The geometry optimized structures of the TSs involved in the hydroboration of PhCOMe by catalysts **A**, **B** and **C** respectively. Atom colour code: C (grey), N (blue), O (oxygen), F (green), S (yellow), Sb (purple), B (pink).

in Figure 7.14. Similar to hydroboration mechanism, here trimethylsilyl cyanide (TMSCN) coordinates with **A**/**B**, leading to the formation of **Int4** complex. NBO analysis of **Int4** features a donor-acceptor interaction between the N lone pair and the empty p orbital of the Sb atom. This electron-donating interaction is stronger in case of **A** ($\Delta E^{(2)}$) = 21.4 kcal/mol) compared to **B** ($\Delta E^{(2)}$) = 14.9 kcal/mol).

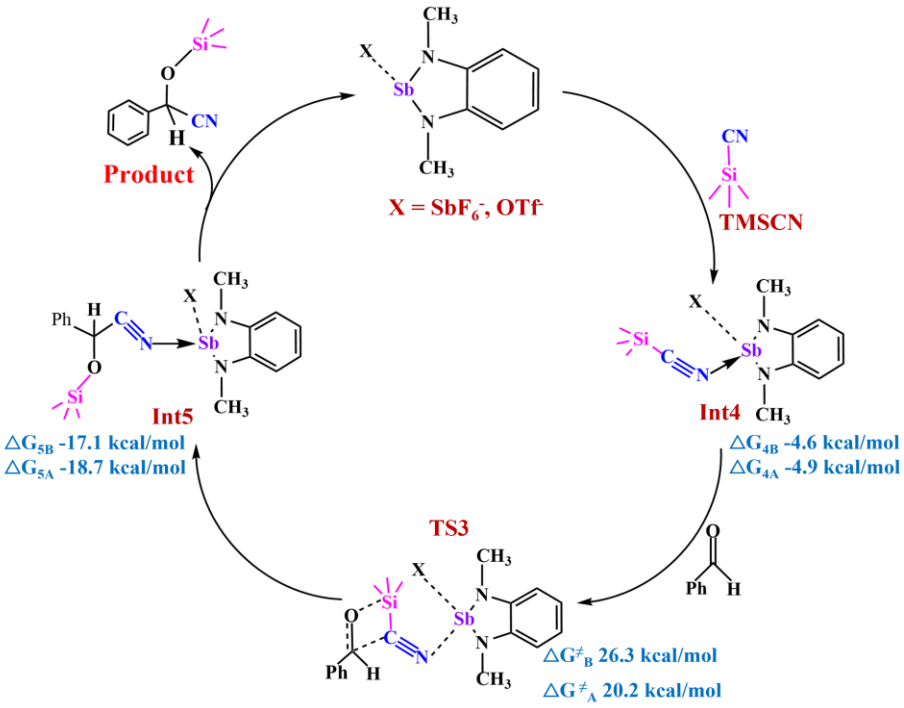

Figure 7.14: Proposed catalytic cycle for cyanosilylation of benzaldehyde using the catalysts **A** and **B**.

This is reflected in the shorter Sb-N distance of 2.689 Å in **Int4A** whereas for **Int4B**, the Sb-N distance is 2.807 Å. Addition of benzaldehyde in **Int4** results in a four-membered transition state, **TS3** where the CN group is transferred to the carbonyl carbon of benzaldehyde. At **TS3A**, which lies at 20.2 kcal/mol (Figure 7.14), catalyst **A** anchors more strongly to TMSCN, as is apparent from the shorter SbN distance (2.420 Å Figure 7.15) and greater extent of Sn-N donor-acceptor interactions ($\Delta E^{(2)}$) = 54.7 kcal/mol) value. For catalyst **B**, **TS3B** lies at 26.3 kcal/mol in the free energy profile where the Sb-N distance reaches to 2.516 Å. At the end the product cyanohydrin is released from **Int5** and the catalyst is regenerated.

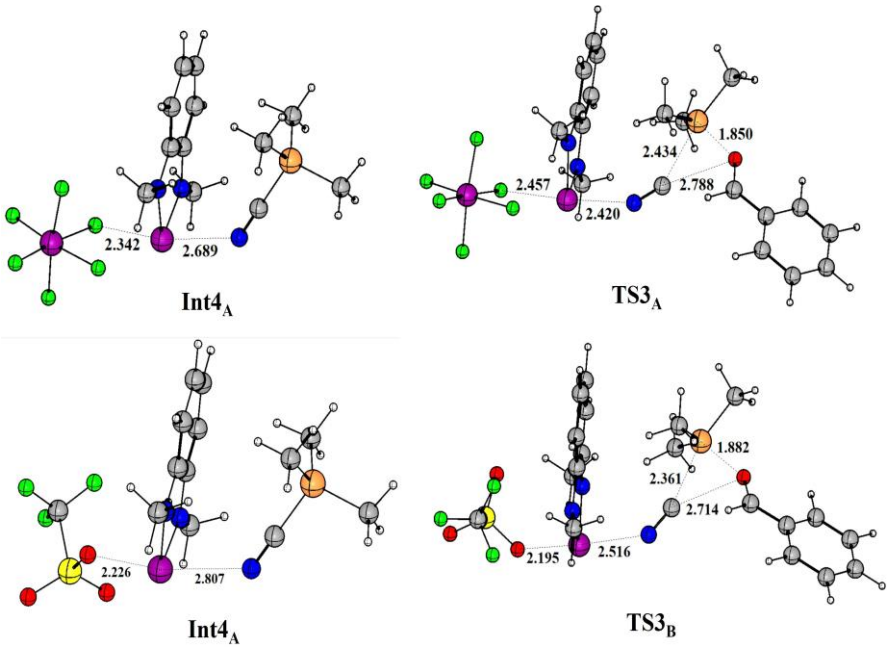

Figure 7.15: The geometry optimized structures of the intermediates/TSs involved in the cyanosilylation of PhCHO, by catalyst **A** (up) and **B** (down).Atom colour code: C (grey), N (blue), O (oxygen), F (green), S (yellow), Sb (purple), Si (golden yellow).

7.4 Conclusions

In summary, we have investigated a new series of cyclic and acyclic Stibenium cations. We observed that in case of these catalysts, the counter anions are loosely bound with cationic core of the system. Paticularly catalyst **A** has a discrete cationic nature and therefore has a high Lewis acidity. Therefore it can act as a efficient catalyst. We have also explored these stibenium cations for hydroboration and cyanosilylation reaction. Our results show that hydroboration reaction by these catalysts proceed via single-anchoring pathway rather than a double-anchoring pathway. Computational results also reveal that due to the high inherent Lewis acidity, catalyst **A** can perform the hydroboration and cyanosilylation reaction of aromatic carbonyl compound under mild condition. However, in case of catalyst **B**, the electron donating interaction from the triflet anion, signifi-

cantly quenches the Lewis acidity of the Sb centre. On the other hand, for acyclic cation **C**, the presence of rigid framework makes it difficult for substrate to come close to active centre. As a result reaction scope is limited for catalyst **B** and **C**.

7.5 References

[1] Huang,E.; Roisnel,T.; Dorcet,V.;Orione, C.; Kirillov,E. Organometallics 2020, 39, 698-710.

[2] Sen.N.; Khan,S. Chem. Asian J., 2021, 16, 705-719.

[3] Shegavi,M. L.; Bose,S. K.; Catalysis Science and Technology 2019, 9, 3307-3336.

[4] Pahar,S.; Kundu G.; Sen, S. S. ACS omega 2020, 5, 25477-25484.

[5] Hsu,C.-P.; Liu, Y.-H.; Boobalan, R.; Lin,Y.-F.; Chein, R.-J.; Chiu,C.-W. Organometallics 2021, 40, 1244-1251.

[6] Franz, D.; Inoue,S. Chemistry Europian. Journal 2019, 25, 2898-2926.

[7] Friedrich,A.; Eyselein,J.; Elsen,H.; Langer,J. ; Pahl,J. ; Wiesinger, M.; Harder, S. Chemistry Europian Journal 2021, 27, 7756-7763.

[8] Sarkar,D.; Dutta, S.; Weetman,C.; Schubert,E. ; Koley,D.; Inoue, S. Chemistry Europian Journal 2021, 27, 13072-13078..

[9] Dagorne,S.; Atwood,D. A. Chemical Review 2008, 108, 4037-4071.

[10] Engesser,T. A.; Lichtenthaler,M. R.; Schleep, M.; Krossing, I. Chemical Society Review, 2016, 45, 789-899.

[11] Koelle,P.; Noeth,H. ; Chemical Review, 1985, 85, 399-418.

[12] Swamy,V. ; Pal,S. ; Khan, S., Sen, S. S. Daltonton Transaction., 2015, 44, 12903-12923.

[13] Fang,H. ; Wang, Z., Fu, X. Coordination Chemisty Review 2017, 344, 214-237.

[14] Miaskiewicz, S. ;Reed,J. H. ; Donets,P. A. ; Oliveira, C. C.; Cramer,N. Angewante Chemie, 2018, 130, 4103-4106.

[15] Rao, B. ; Chong, C. C.; Kinjo, R. Journal of American Chemical Society 2018, 140, 652-656.

[16] Lundrigan,T. ; Welsh, E. N. ; Hynes,T. ; Tien, C.-H. ; Adams,M. R. ; Roy, K. R. ;Robertson, K. N.; Speed, A. W. H. Journal of American Chemical Society 2019, 141, 14083-14088.

[17] Veith M. ; Bertsch, B.; Anorg, Z., Chem. 1988, 557, 7-22.

[18] Veith, M. ; Bertsch, B.; Huch, V.; Anorg. Z. Chem., 1988, 559, 73-88

[19] Carmalt,C. J. ; Walsh,D. ; Cowley, A. H.; Norman,N. C. Organometallics 1997, 16, 3597-3600..

[20] Burford,N. ; Macdonald, C. L. B.; LeBlanc, D. J.; Cameron, T. S. Organometallics 2000, 19, 152-155.

[21] Gudat, D., Gans-Eichler, Nieger, M. Chem Communication 2004, 2434-2435.

[22] Gans-Eichler,T. ; Gudat, D. ; Nieger, M.; Heteroatomic. Chemistry, 2005, 16, 327-338.

[23] Spinney,H. A.; Korobkov, I. ; DiLabio, G. A. ; Yap, G. P. A.; Richeson, D. S. Organometallics 2007, 26, 4972-4982.

[24] Spinney, H. A. ; Korobkov, I. ; Richeson,D. S. Chem. Communication, 2007, 1647-1649.

[25] Kilah, N. L. ; Petrie,S. ; Stranger,R. ; Wielandt,J. W. ; Willis, A. C.; Wild,S. B. Organometallics 2007, 26, 6106-6113.

[26] Lehmann,M. ; Schulz, A. ; Villinger, A. Europian Journal of Inorganic Chemistry, 2010, 5501-5508.

[27] Price,J. T. ; Lui, M. ; Jones, N. D. ; Ragogna, P. J. Inorganic Chemistry 2011, 50, 12810-12817.

[28] Hering,C. ; Lehmann, M. ; Schulz, A. ; Villinger, A. Inorganic Chemistry, 2012, 51, 8212-8224.

[29] Srungavruksham, N. K. ; Liu, Y.-H. ; Tsai, M.-K.; Chiu, C.-W. Inorganic Chemistry, 2020, 59, 4468-4474.

[30] Lehmann,M. ; Schulz, A.; Villinger, A. Angewante Chemie Int. Ed., 2012, 51, 8087-8091.

[31] Zhao, Y.; Truhlar, D. G. Theoretical Chemistry Accounts: Theory, Computation, and Modeling (Theoretica. Chimica. Acta) 2008, 120, 215–241.

[32] Zhao, Y.; Truhlar, D. G. Density functionals with broad applicability in chemistry. Acc. Chem. Res. 2008, 41, 157–167.

[33] Andrae, D.; Haeussermann, U.; Dolg, M.; Stoll, H.; Preuss, H Theoretical Chemistry Accounts: Theory, Computation, and Modeling (Theoretica. Chimica. Acta.) 1990, 77, 123–141

[34] Marenich, A. V.; Cramer, C. J.; Truhlar, D. G. Journal of Physical Chemistry B 2009, 113, 6378–6396

[35] Wertz, D. H. Journal of American Chemical Society 1980, 102, 5316-5322.

[36] Dirk V. Journal of American Chemical Society 2008, 130, 665-675.

[37] Rios, P.; Rodriguez, A.; Lopez-Serrano, J. ACS Catalysis 2016, 6, 5715–5723.

[38] Dasgupta, R. ; Das, S. ; Hiwase, S. ; Pati, S. K. ; Khan, S. Organometallics 2019, 38, 1429-1435.

8

Summary & Outlook

The filed of main-group catalysis has witnessed a rapid development particularly during the last decade. Several outstanding research has been reported which convinced the scientific community that light main-group elements, specifically Group 13, 14 and 15 can acts as efficient catalyst for many important organic transformations which are once considered stronghold of heavy transition metals. A renaissance of main-group chemistry has been accelerated partly by the discovery of FLPs in 2006. The early years of FLP chemistry are devoted to understanding the fundamental concepts underlying FLP reactivity. Moving on, attention has been given to broaden the reach across the substrate scope, new FLP systems as well as to develop new efficient catalytic protocol by combining the existing FLPs with some 3d-transition metals. Apart from this, N-Heterocyclic Carbene based complexes as well as p-block Lewis acids has demonstrates their potential in this field. Our contribution in this area, which we have reported in the previous six work chapters, was to provide a conceptual understanding of the fundamental mechanism in these recently developed systems. In the concluding chapter of this thesis, we recollect and summarize the key findings of our computational studies. Also here we wish to mention a few aspects, we might be useful for future aspects.

In our study of quinoline reduction we proposed that hydrogenation reaction

by the borenium cations proceeds in a stepwise manner. The substrate quinoline acts as Lewis base during the dihydrogen activation along with the borenium ion Lewis acid, In addition we have also observed that the steric hindrance at the active centre of the aNHC stabelized borenium ion makes it inefficient towards the hydrogenation reaction.

Subsequently we have examined a new family intramolecular FLPs, $(C_2F_5)_3E$-$CH_2P(tBu)_2$ (E = Si, Ge, Sn). We proposed that during the dihydrogen activation these neutral Tetrel atoms, in absence of a vacant p orbital, borrow the required Lewis acidity from its adjacent anti-bonding orbital. We have extended this idea and explored their potentials as hydrogenation catalysts towards carbon dioxide, carbonyl and imine substrates. Our computed results reveal that significant improvement in the reactivity can be achieved by changing the donor centre from phosphorous to nitrogen. The synchronous reaction profiles of N-containing FLPs make them better catalysts for H_2 activation as well as for hydrogenation. Our results also suggests that while dimer formation is not a inhibiting side reaction for these geminal FLPs, reductive elimination reaction can be a possible side reaction for some of the FLPs.

Then we investigate the cooperative catalysis between copper hydride and Lewis pair during CO_2 hydrogenation reaction. Our results delinates the crucial role of the THF solvent as an active participant during activation of H_2 as well as transferring the proton ion generates from it. The role of the base DBU is also elucidated which show that DBU play a crucial role by releasing the formate group from the copper formate complex which is starting point of the next catalytic cycle. Moreover the inefficiency of PMP-BCF FLP towards this reaction is also investigated.

Next we explored the mechanism of reductive functionalization of amide using CO_2 as the methylene source catalysed by a mesoionic N-heterocyclic imine. Our results rationalize the high nucleophilicity and high proton affinity of these class

of N-heterocyclic imines arrising from their associated with the polarized ylide structure. Our results also show that several reaction steps like formation of N-silylated amide and in the reduction of formyl group of N-formyl amide, enjoyed a kinetic advantage due to strong donating ability of the mesoionic N-heterocyclic imine catalyst.

Finally we investigate a new series of cyclic and acyclic stibenium cations for hydroboration and cyanosilylation reaction. Our results show that steric enviroment around the active antimony site of the catalyst as well as the coordination strength of the counter anions significantly influence the reactivity of these stibenium ions.

Thus in this thesis we have tried to provide mechanistic understanding of some reduction reaction catalysed by various main-group species whose reactivity are relatively new. We are hopeful that the results presented here will help the scientific community for rational designing of main-group catalyst in near future. From here, the future research could propagated to many possible direction. One possible route is to explore new candidates based on environmentally benign species. But at the same time it is equally important to modify and optimize the existing catalyst for improved reactivity and selectivity. In this regard, systematic computational studies along with use of machine learning algorithms could play a crucial role to identify the influencing parameters and therefore to design prospective catalysts more rapidly instead of a trial and error approach. It is important to mention here that although the idea of metal-free hydrogenation protocol is truly appealing, till now main-group catalysts are often inferior than the existing transition metal catalysts. One possible solution could be designing a combined protocol which can be benefited from both main-group as well as 3d transition metal elements. The another alternative which gained lot of attraction recently is the utilization of heterogenized molecular catalyst where either the main-group elements are linked to a surface or they are incorporated into a porous material

like metal organic framework or zeolite and it can be expected that these new approaches might eventually carry main-group catalysis from laboratory research to the domain of industrial applications.